Titre: Title:	Early Detection of Doxorubicin-Induced Cardiotoxicity Using Combined Biomechanical Modeling and Multi-Parametric Cardiovascular MRI
Auteur: Author:	Mohamed Aissiou
Date:	2016
Type:	Mémoire ou thèse / Dissertation or Thesis
Référence: Citation:	Aissiou, M. (2016). Early Detection of Doxorubicin-Induced Cardiotoxicity Using Combined Biomechanical Modeling and Multi-Parametric Cardiovascular MRI [Ph.D. thesis, École Polytechnique de Montréal]. PolyPublie. https://publications.polymtl.ca/2212/

UNIVERSITÉ DE MONTRÉAL

EARLY DETECTION OF DOXORUBICIN-INDUCED CARDIOTOXICITY USING COMBINED BIOMECHANICAL MODELING AND MULTI-PARAMETRIC CARDIOVASCULAR MRI

MOHAMED AISSIOU

INSTITUT DE GÉNIE BIOMÉDICAL

ÉCOLE POLYTECHNIQUE DE MONTRÉAL

THÈSE PRÉSENTÉE EN VUE DE L'OBTENTION

DU DIPLÔME DE PHILOSOPHIAE DOCTOR

(GÉNIE BIOMÉDICAL)

AOÛT 2016

UNIVERSITÉ DE MONTRÉAL

ÉCOLE POLYTECHNIQUE DE MONTRÉAL

Cette thèse intitulée:

EARLY DETECTION OF DOXORUBICIN-INDUCED CARDIOTOXICITY USING COMBINED BIOMECHANICAL MODELING AND MULTI-PARAMETRIC CARDIOVASCULAR MRI

présentée par : AISSIOU Mohamed

en vue de l'obtention du diplôme de : Philosophiae Doctor

a été dûment acceptée par le jury d'examen constitué de :

M. VINET Alain, Ph. D., président

Mme PÉRIÉ-CURNIER Delphine, Doctorat, membre et directrice de recherche

Mme CHERIET Farida, Ph. D., membre et codirectrice de recherche

M. TOURNOUX François, M.D., Ph. D., membre

M. YOUNG Alistair Andrew, Ph. D., membre externe

DEDICATION

This work is dedicated to my parents, for their love.

ACKNOWLEDGEMENTS

I would like to thank Professor Delphine Périé-Curnier, my research director for leadership, the continuous support during these many years and for having accepted to supervise me. I would also like to thank Professor Farida Cheriet for her time and the enormous support provided for this work.

I would also like to express gratitude to the following organizations for their financial support: The MÉDITIS training program, the Cole Foundation, École Polytechniqus de Montréal and the CHU Sainte-Justine Research Center.

I would like to thank Guillaume Gilbert and Tarik Hafyane for their technical support during MRI acquisitions and data analysis. I would also like to thank my colleagues at the mécano-imagerie tissulaire laboratory, for their friendly presence and their help during algorithms testing. They were: Clémence Balosetti, Marc-Olivier Lapointe, Maxime Huber, Simon-Pierre Côté and Pierre-François Beauchemin.

I would like to thank my parents for everything they provided me and for their enormous love, support and their continuous presence.

RÉSUMÉ

La chimiothérapie à la doxorubicine est efficace et est largement utilisée pour traiter la leucémie lymphoblastique aiguë. Toutefois, son efficacité est entravée par un large spectre de cardiotoxicités incluant des changements affectant à la fois la morphologie et la fonction du myocarde. Ces changements dépendent principalement de la dose cumulée administrée au patient. Actuellement, très peu de techniques sont disponibles pour détecter de telles cardiotoxicités. L'utilisation d'images de fibres musculaires (par exemple, à l'aide de l'imagerie des tenseurs de diffusion par IRM) ou des techniques d'imagerie 3D (par exemple, ciné DENSE IRM) sont des alternatives prometteuses, cependant, leur application en clinique est limitée en raison du temps d'acquisition d'images et les erreurs d'estimation qui en résultent.

En revanche, l'utilisation de l'IRM multi-paramétrique ainsi que le ciné IRM sont des alternatives prometteuses, puisque ces techniques sont déjà disponibles au niveau clinique. L'IRM multiparamétrique incluant l'imagerie des temps de relaxation T1 et T2 peut être utile dans la détection des lésions dans le tissu du myocarde alors que l'imagerie ciné IRM peut être plus appropriée pour détecter les changements fonctionnels au sein du myocarde. La combinaison de ces deux techniques peut également permettre une caractérisation complète de la fonction du tissu myocardique.

Dans ce projet, l'utilisation des temps de relaxation T1 pré- et post-gadolinium et T2 est d'abord évaluée et proposée pour détecter les dommages myocardiques induits par la chimiothérapie à la doxorubicine. En second lieu, l'utilisation de patrons 2D de déplacements myocardiques est évaluée dans le cadre de la détection des dommages myocardiques et altération fonctionnelle due au traitement à la doxorubicine. Enfin, l'utilisation de la modélisation par éléments finis, incluant les contraintes et déformations mécaniques est proposée pour évaluer les changements dans les propriétés mécaniques au niveau du myocarde, avec l'hypothèse que le traitement à base de doxorubicine induit des changements importants à la fois dans le tissu et au niveau de la fonction myocardique.

Dans notre cohorte de survivants de cancer, des changements myocardiques locaux ont été trouvés entre le groupe à risque standard et le groupe à risque élevé lorsque le T1 pré-gadolinium fut utilisé. Ces changements ont été amplifiés avec l'utilisation d'agent de contraste tel que confirmé par le coefficient de partition, ce qui suggère que l'utilisation du T1 post-gadolonium et le coefficient de

partition peuvent être des biomarqueurs d'imagerie utiles dans la détection des cardiomyopathies induites par la doxorubicine. D'autre part, l'utilisation de T2 a montré que le groupe à risque élevé avait un T2 plus élevé comparé au groupe à risque standard et similaire aux valeurs rapportées dans la littérature. Toutefois, une plus grande cohorte de survivants de cancer peut être nécessaire pour évaluer l'utilisation des temps de relaxation T1 et T2 comme étant des indices éventuels de détection des dommages myocardiques dans le contexte de la cardiotoxicité induite par la doxorubicine.

Dans la même cohorte de volontaires qui ont été évalués dans cette étude, les patrons de déplacement myocardiques étaient significativement plus faibles chez les survivants du cancer comparativement aux volontaires sains, bien que la signature des courbes de déplacement soit resté similaire. L'utilisation du suivi myocardique basé sur la technique d'extraction du squelette myocardique devrait être examiné et pourrait ouvrir de nouvelles avenues pour une meilleur estimation des déplacements myocardiques, puisque la technique réduit considérablement le phénomène de glissement et est basée sur les caractéristiques géométriques du myocarde. Cependant, plusieurs limites doivent être traitées comme par exemple le fait que le mouvement à travers le plan ne soit pas considéré. Le fait d'inclure ce mouvement dans notre modèle pourrait permettre une évaluation quantitative des déplacements du myocarde.

Notre nouvelle technique pour estimer les contraintes et déformations myocardiques donne des résultats robustes et un suivi précis du tissu myocardique. Les contraintes et déformation étaient évaluées en utilisant soit la technique linéaire soit la technique cumulative. Les deux techniques donnent une estimation indépendante des contraintes et déformations qui peut être utilisée pour détecter tout changement dans la fonction mécanique du myocarde. Encore une fois, dans la même cohorte de survivants de cancer, les contraintes et déformations myocardiques étaient significativement plus faibles par rapport aux volontaires sains, ce qui pourrait indiquer une réduction de la fonction contractile du myocarde. L'utilisation des contraintes et déformations apparentes devrait apporter de nouveaux renseignements en termes de la fonction mécanique du myocarde qui doivent être explorés.

Pour conclure, pour le moyen et long terme, ce projet contribue à l'avancement des connaissances dans le domaine des cardiomyopathies induites par la doxorubicine, le suivi du myocarde et l'analyse multiparamétrique du myocarde. En outre, les techniques présentées dans cette étude pour

la détection précoce des cardiotoxicités induite par la doxorubicine sont toutes prometteuses. Nous croyons que tous les indices présentés ont leur mot à dire dans la détection des cardiotoxicités induite par la doxorubicine. Toutefois, la technique des patrons de déplacement est considérée comme étant la plus susceptible de détecter précocement les cardiotoxicités induite par la doxorubicine.

ABSTRACT

Doxorubicin chemotherapy is effective and widely used to treat acute lymphoblastic leukemia. However, its effectiveness is hampered by a wide spectrum of dose-dependent cardiotoxicity including both morphological and functional changes affecting the myocardium. Currently, very few techniques are available for detecting such cardiotoxic effect. The use of muscle fibers orientation (e.g., diffusion tensor imaging DT-MRI) or 3D imaging techniques (e.g., cine DENSE MRI) are possible alternatives, however, their clinical application is limited due to the acquisition time and their estimation errors.

In contrast, the use of multi-parametric MRI along with cine MRI is a promising alternative, since theses techniques are already available at a clinical level. Multiparametric MRI including T1 and T2 imaging may be helpful in detecting myocardial tissue damage, while cine MRI may be more appropriate to detect functional changes within the myocardium. The combination of these two techniques may further allow an extensive characterization of myocardial tissue function.

In this doctoral project, the use of pre- and post-gadolinium T1 and T2 relaxation times is firstly assessed and proposed to detect myocardial damage induced by doxorubicin chemotherapy. Secondly, the use of 2D myocardial displacement patterns is assessed in detecting myocardial damage and functional alteration due to doxorubicin-based treatment. Finally, the use of finite element modeling including mechanical strains and stresses to evaluate mechanical properties changes within the myocardium is alternatively proposed, assuming that doxorubicin-based treatment induces significant changes to both myocardial tissue morphology and function.

In our cohort of cancer survivors, local myocardial changes were found between standard risk and high risks group using pre-gadolinium T1 relaxation times. These changes were further amplified with gadolinium enhancement, as confirmed by the use of partition coefficient, suggesting this MRI parameter along with partition coefficient as candidates imaging markers of doxorubicin induced cardiomyopathy. The use of T2 on the other hand showed that the high risk group of cancer survivors had higher T2 relaxation times compared to the standard risk group and similar to reported values. Though, a larger cohort of cancer survivors may be required to assess the use of T1 and T2 relaxation time as possible indices for myocardial tissue damage in the onset of doxorubicin-induced cardiotoxicity.

Within the same cohort of volunteers that were assessed in this study, displacement patterns were significantly lower in cancer survivors compared to healthy volunteers, although the signature of displacement curves remained similar. The use of skeleton-based myocardial tracking should further be considered and may open doors to a better estimation of myocardial displacements since it significantly reduces the sliding phenomenon and relies on myocardial geometry characteristics. However, several limitations need to be addressed such as the through-plane motion in order to allow quantitative assessment of myocardial displacements.

Our new technique for estimating myocardial strains and stresses provided robust results and accurate tracking of myocardial tissue. Myocardial strains were assessed using either a linear-based or cumulative-based estimation of strains and stresses. Both techniques provided independent estimation that can be used to detect any alteration within the myocardial contractile function. Again, within the same cohort of volunteers, the apparent strains and stresses were significantly lower compared to healthy volunteers, which may indicate a reduction in myocardial contractile function. The use of apparent strains and stresses should further bring new insights in terms of myocardial mechanical function which needs to be explored.

To conclude, for the medium and long term, this project contributes to the advancement of knowledge in the field of doxorubicin-induced cardiomyopathies, myocardial tracking and multiparametric analysis of the myocardium. Furthermore, the presented techniques for detecting doxorubicin-induced cardiotoxicity are all promising. We believe that all of the presented indices may have a say in detecting doxorubicin-induced cardiotoxicity with displacement patters analysis being the most susceptible to early detect doxorubicin-induced cardiotoxicity.

TABLE OF CONTENTS

LIST OF TABLES

LIST OF FIGURES

LIST OF SYMBOLS AND ABBREVIATIONS

2CH	2-chamber view
4CH	4-chamber view
2D	2-dimensional
3D	3-dimensional
DF	Diastolic fraction
ED	Early diastole
EF	Ejection fraction
ε/σ	Mechanical strain/stress
HR	High risk cancer survivors
HV	Healthy volunteers
LD	Late diastole
LV	Left ventricle
MRI	Magnetic resonance imaging
RV	Right ventricle
SA	Short-axis view
SD	Standard deviation
SE	Septum
SR	Standard risk cancer survivors
TD	Telediastole
TF	Thickening fraction
TS	Telesystole
vM	von Mises index

XY	XY index or XY resultant

LIST OF APPENDICES

CHAPTER 1 INTRODUCTION

Doxorubicin, belonging to the anthracycline family is a chemotherapeutic agent used for the treatment of many types and forms of cancer including leukemia, lymphomas, osteosarcomas, soft tissue sarcomas and breast, lung, bladder, endometrium, uterus, stomach and thyroid cancers [1]. It is normally administered by rapid intravenous doses [2, 3], and is believed to reside between the DNA strands of cancerous cells to further inhibit macromolecules synthesis and topoisomerase II progression [4].

In the case of acute leukemias, the major problem related to doxorubicin chemotherapy lies in its cardiotoxic effects that depends mainly on the administered cumulative dose [5-7, 2, 8-10]. This cardiotoxicity affects not only molecular mechanisms, but also regional and global cardiac function. With current treatments, very few of these cardiotoxic effects appear reversible while the majority of them are not.

1.1 Cardiotoxicity of doxorubicin

In terms of molecular mechanisms, the main cardiotoxic effects at short-term, induced by moderate to high cumulative doses of doxorubicin, include: reactive oxygen species (ROS) generation [11-13], lipid peroxydation of mitochondrial and sarcoplasmic membrane [14-18], calcium homeostasis alterations [19-21], iron (Fe3) homeostasis alteration [22-24], induced cellular apoptosis through signaling and ROS generation [25-27]. In terms of histologic changes, the cardiotoxic effects include: extracellular matrix disorganisation [28, 4], induced diffuse fibrosis [21, 4], muscle fibers and cardiomyocytes number decrease [5, 29, 30], mitochondrial swelling and myofibrillar Z-lines irregularity [5]. On the other hand, the cardiotoxic effects in terms of electrophysiological changes include: sinus tachycardia [31, 2], QRS-T signal amplitude drop [5, 28] and premature ventricular contraction [31, 32, 4]. Finally, the cardiotoxic effects in terms of morphological and functional alterations include: ventricular systolic function decrease [33, 34, 8, 4], ventricular dilatation and myocardial wall thinning [7, 4] and ventricular contractile function along with radial deformation decrease [7] [35, 4].

Several histological changes (Figure 1.1) in the myocardium are related to doxorubicin-based therapy. Druck et al. (1984) reported the presence of 68% of patients with histological grade of 1.0 or more following administered doxorubicin doses above 200 mg/m^2 [32]. In addition, several other

histological observations are described including: loss of muscle fibers and increased interstitial tissue along with altered syncytial arrangement of muscle fibers [5, 35], presence of diffuse fibrosis and myofibrilar loss [28, 4, 30], myocyte vacuolization [29] and mitochondrial loss with myofibrilar structure disorganization [21]. Most cardiomyopathies are reported in the left ventricle as it is the most studied cardiac chamber. However, there are currently no proposed models in the literature to assess doxorubicin-induced cardiotoxicity to our knowledge.

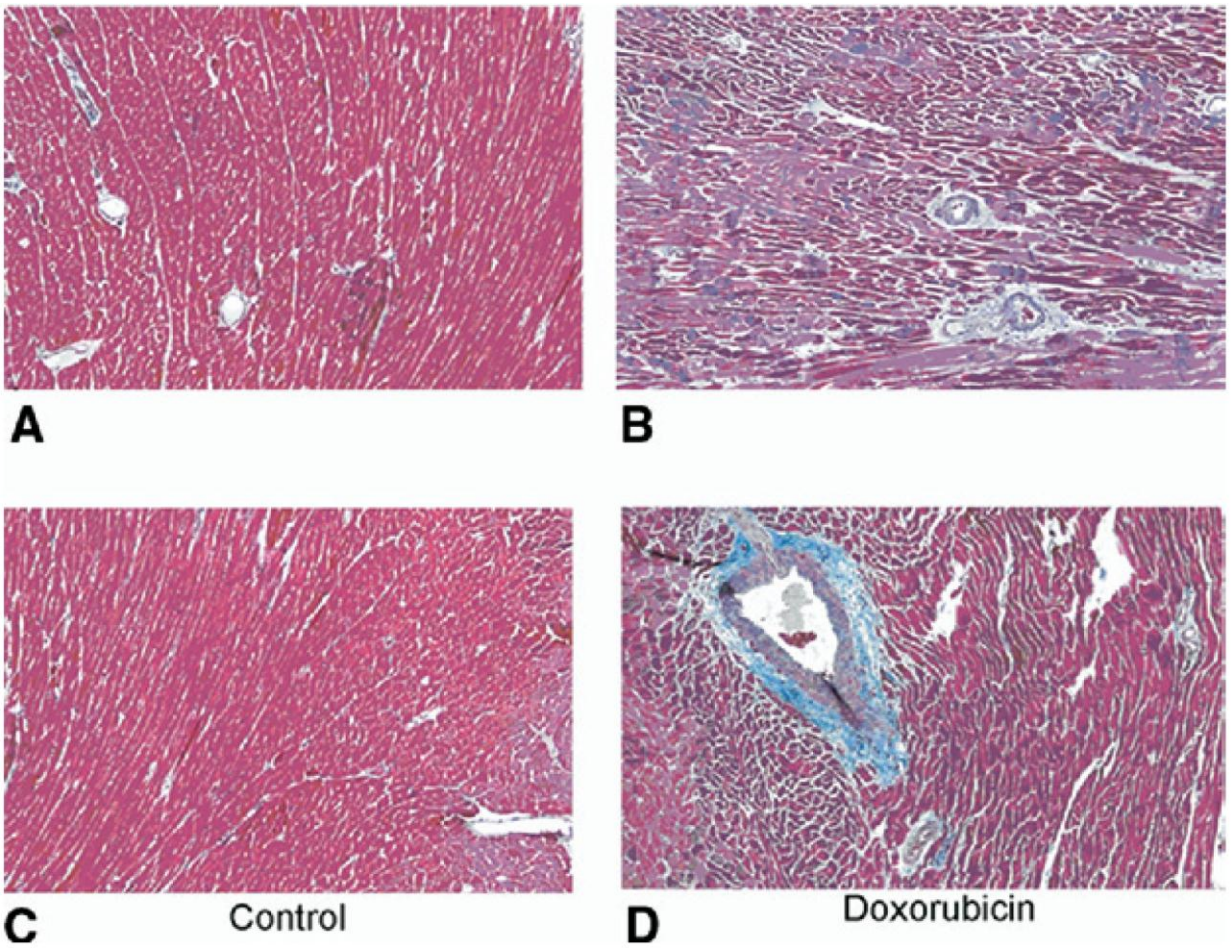

Figure 1.1: Myocardium histologic slice from a rat treated with doxorubicin. Masson's trichrome stain at the mid-ventricular level in control rats (A et C) compared with rats pre-treated with doxorubicin (B et D). Note the presence of interstitial and perivascular fibrosis (blue stain) in pre-treated rats (adapted from Migrino et al., (2008) [35]).

Furthermore, most of doxorubicin-induced cardiotoxic effects are progressive and occur during the first 6 months after the last treatment [34]. Their amplitude depends mostly on the cumulative dose of doxorubicin, usually measured in milligrams per square meter of body surface area. Some changes occur early while other take several weeks or even months to manifest, and at this stage become irreversible by current treatments [36]. In addition, the contribution of these cardiotoxicities to cardiac dysfunction and myocardial tissue damage in children is not well understood, considering that current clinical indices can only detect important tissue damages [35, 37, 38].

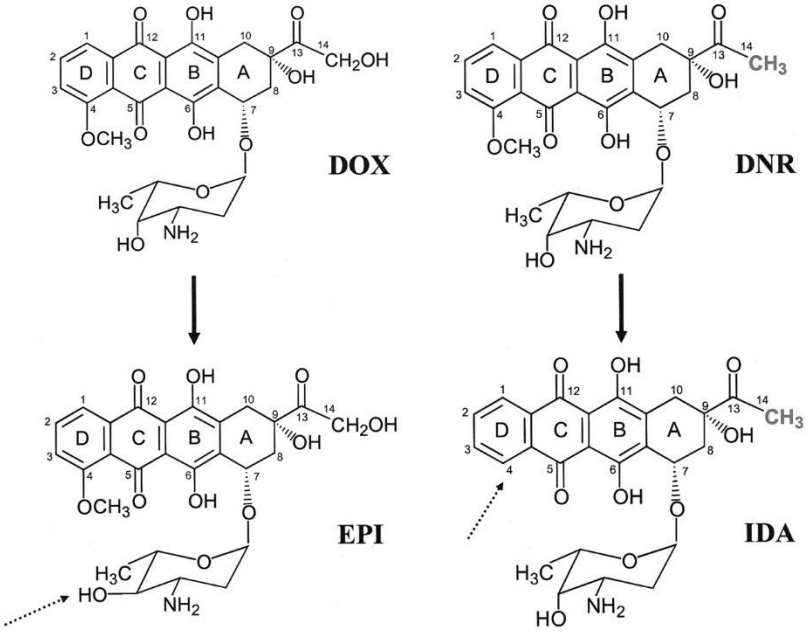

Figure 1.2: Molecular structure of doxorubicin and its analogues (DOX: doxorubicine, DNR: daunaurubicine, EPI: epirubicine, IDA: idarubicine) of the anthracycline family (adapted from Minotti et al. (2004) [39]).

On the cardiac function part, chemotherapeutic treatment with doxorubicin (molecule displayed in Figure 1.2) induces several changes in cardiac function. According to the cumulative dose administered, these changes include: increased heart rate [40], diastolic pressure and heart mass [28], dilatation of the ventricular myocardium [28, 4], increased myocardial wall stress, ventricular diastolic dysfunction [7, 4], reduced ejection and shortening fractions [33, 34, 8, 4], decreased radial contractility [35, 41] and sometimes induced heart failure [5, 9].

1.2 Cardiomyopathies diagnosis

Doxorubicin seems to alter both functional and biochemical parts of the heart. Although mechanisms behind their action remain uncertain, diagnosing them early is crucial to prevent future progressive degeneration of the heart tissue and its function. Current gold standard for the diagnosis of doxorubicin-induced cardiomyopathie remain endomyocardial biopsy of both the left and right ventricle [42, 43]. However, the main drawback of myocardial biopsy is that it is invasive. Non-invasive techniques include 12-lead electrocardiogram, echocardiography and MRI [44, 45]. While MRI is often the gold standard within non-invasive techniques, echocardiography remains the most used tool to diagnose doxorubicin-induced cardiotoxicity. Exercise-spirogometry and stress-echocardiography [45] have also been proposed as possible biomarkers to detect late cardiotoxicity. On the other hand, the use of contrast enhancement agents in MRI is also a promising alternative [46].

Furthermore, most of the reported studies use echocardiography to estimate myocardial displacements and characteristics in the context of doxorubicin-induced cardiomyopathies. However, the geometric assumptions behind echocardiography, which affect both the M mode and two dimensional echocardiography, may lead to inaccurate measurement of myocardial characteristics [47]. MRI on the other hand is considered as the gold standard within non-invasive techniques. It is not only non-invasive but also provides high-quality cardiovascular images which can be used to diagnose cardiomyopathies. MRI provides not only conventional cine MRI images which are used to extract myocardial displacement and other characteristic and functional parameters with high precision, but also other more specialized imaging sequences such as T1 and T2 relaxation times that can be used to detect alterations in terms of the biochemical contents of the myocardium.

1.3 Thesis plan

This thesis is presented by scientific articles. The rest is organized into seven chapters. First, Chapter 2 presents a review of literature of reported doxorubicin-induced cardiotoxicity. Chapter 3 discusses the context, objectives and the main hypotheses of the thesis as well as the overall approach of the research work. The next four chapters are devoted to the original contributions of this thesis and correspond to the four articles published or in the process of submission. Chapter 4

includes the first article that reviews doxorubicin-induced cardiotoxicity, published in The international journal of cardiovascular imaging. Chapter 5 includes the second article, submitted to the Journal of Magnetic Resonance Imaging, which investigate the use of myocardial T1 and T2 relaxation times as biomarkers for doxorubicin-induced cardiotoxicity. Chapter 5 includes the third article that investigates the use of myocardial displacements patterns using clinical cine MRI in doxorubicin-treated cancer survivors, submitted to the Journal of Cardiovascular Magnetic Resonance. Chapter 6 includes the fourth article that investigates the use of myocardial 2D strains and stresses in the detection of doxorubicin-induced cardiomyopathies, submitted to Medical Image Analysis. Chapter 7 proposes a general discussion of the overall work done during this project and finally the conclusion which discusses the contributions of this thesis, the new avenues of research to be explored and perspectives for future work.

CHAPTER 2 LITERATURE REVIEW

In this chapter, a brief review of the literature on the heart and on the different methods we used to investigate doxorubicin-induced cardiotoxicity is presented. It is organized into four main sections. Section 2.1 covers some key aspects about the anatomy and physiology of the human heart that are relevant to understand how the heart is affected by doxorubicin-based chemotherapy. Section 2.2 presents the pertinence of the use of MR parameters such as T1 and T2 relaxation times in the early detection of doxorubicin-induced cardiotoxicity. Section 2.3 presents the use of myocardial displacement patterns and their application in the context of early detection of myocardial damage induced by doxorubicin-based chemotherapy. Finally, section 2.4 covers the use of biomechanical indices such as mechanical strains and stresses and explains how they may be relevant when investigating the structural part of the cardiac function in the onset of doxorubicin-induced cardiotoxicity.

2.1 Anatomy and physiology of the human heart

The anatomy and physiology of the human heart play a key role in understanding the mechanisms related to the cardiotoxicity induced by doxorubicin-based chemotherapy. The main function of the heart, being to supply the human body in blood fluid, is mainly accomplished by the heart muscle, known as the "myocardium". Taking the left ventricle as a point of origin (see Figure 2.1), the oxygenated blood is propelled with a LV pressure of 140 mmHg (see Table 2.1), which allows the opening of the aortic valve and blood distribution to the human body. Once the blood runs through the body to perform its function, it returns through the inferior and superior vena cava where it passes through the right atrium before being propelled to the right ventricle through the tricuspid valve with a pressure approximately of 5 mmHg. When the right ventricle is filled (end of atrial systole / end of ventricular diastole), the ventricular myocardium contracts and pumps the blood to the lungs through the pulmonary valve with a pressure of approximately 15-30 mmHg. Once the blood passes through the pulmonary circuit to be oxygenated, it returns through the pulmonary veins, where it passes through the left atrium before being propelled, following the atrial contraction, to the left ventricle through the mitral valve with a pressure of about 12 mmHg. Afterwards, the same loop is completed for each cardiac cycle. Ventricular pressure and volume curves followed during a specific cardiac cycle are shown in Figure 2.2.

Table 2.1: Cardiac chambers and arteries systolic and diastolic pressure (adapted from Klingensmith, 2008 [48]).

Compartment	Pressure (mmHg) S/D
superior/inferior vena cava.	3-5
Right atrium	2-5
Right ventricle	15-30/3-8
Pulmonary artery	15-30/4-12
Pulmonary vein	2-15
Left atrium	6-12
Left ventricle	100-140/3-12
Aorta	120/80

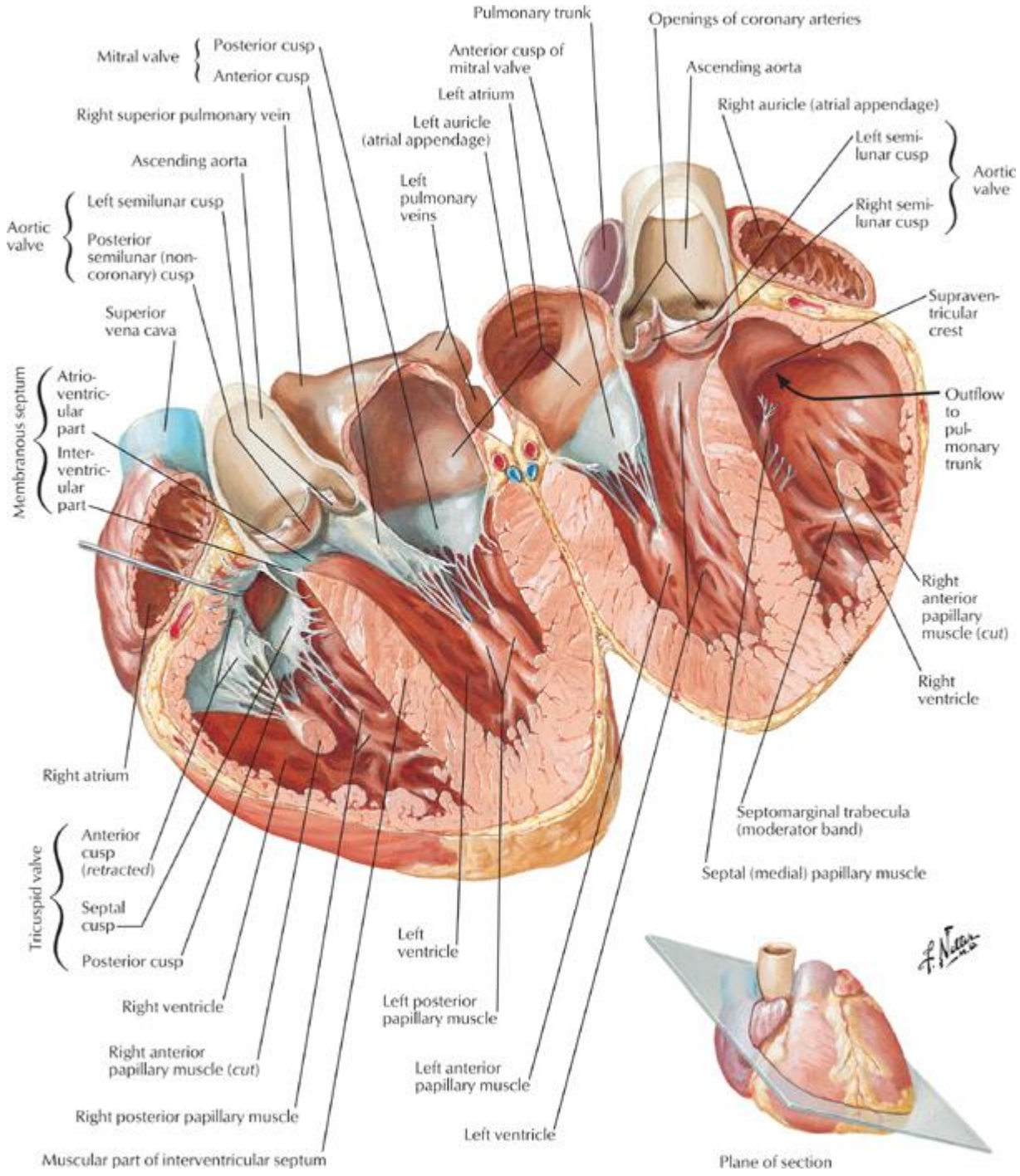

Figure 2.1: Human heart anatomy in 4-chamber view (Adapted from Netter, 2010 [49]).

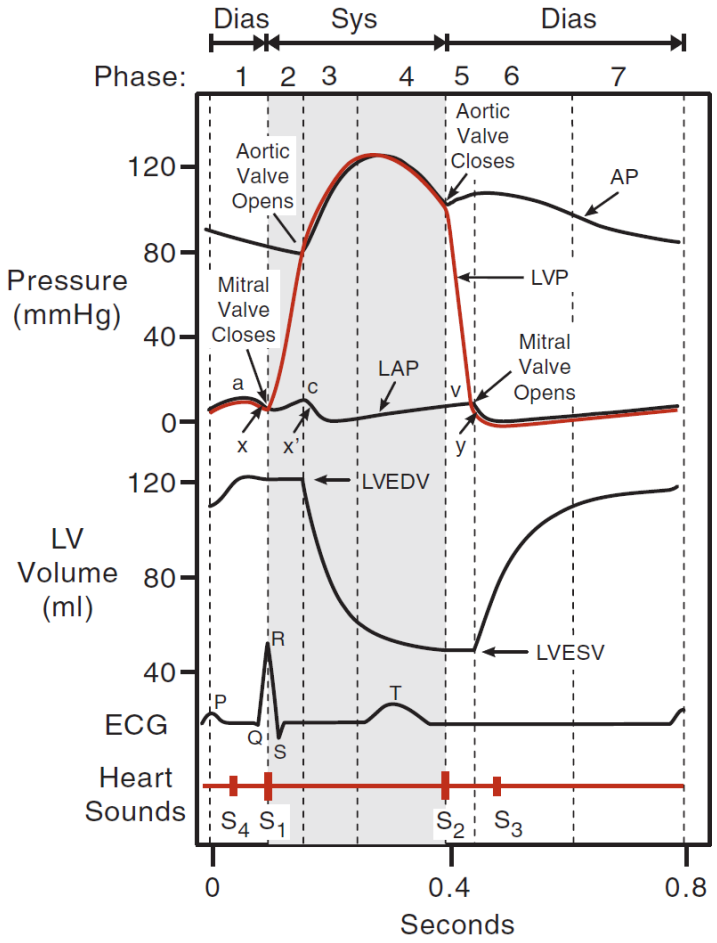

Figure 2.2: The cardiac cycle and pressure/volume curves. (1) atrial systole, (2) isovolumic contraction, (3) fast ejection, (4) reduced ejection, (5) isovolumic relaxation, (6) rapidly filling period and (7) reduced filling. (Adapted from Klabunde, 2011 [50]).

In general, for each cardiac chamber, pressure and volumes curves (Figure 2.2) depend mainly on the input / output in terms of blood fluid, the geometry in which the fluid is confined along with the loading conditions which are represented mainly by myocardial contraction. The functional layers of cardiac tissue are the epicardium, myocardium and endocardium. The epicardium is comprised of connective tissue surrounded by epithelium which helps to limit the volumic expansion of the heart. The myocardium is composed of muscle fibers present in circular, oblique and helical forms and maintained by the fibrous skeleton. The arrangement of the cardiac muscle fibers is represented by two electrically isolated syncytia that are maintained by the skeleton: atrial syncytium and ventricular syncytium. The anchors and insertion point of the fibers is mainly

located in the cardiac fibrous skeleton which surround fibrous rings in peripheries of the valves except the tendinous cords, mainly found in the left and right ventricles.

In parallel, the heart contracts due to an electrical impulse that propagates through atrial myocardium first (Figure 2.3), then through ventricular myocardium to initiate myocardial contraction. During each cardiac cycle, an electrical impulse is generated at the sinoatrial node, i.e., SA node, where it propagates through the atrial myocardium and stimulates it to trigger atrial systole. Once the impulse reaches the atrioventricular node, i.e., AV node, it is delayed by approximately 100ms (Figure 2.4), before being propagated to ventricular myocardium through the His bundle and until it reaches the Purkinje fibers. Afterward, ions would run freely between cardiomyocyte through gap junctions where they trigger cardiomyocyte contraction, i.e., ventricular systole. The time for electrical impulses to reach different myocardial regions is shown in Figure 2.4.

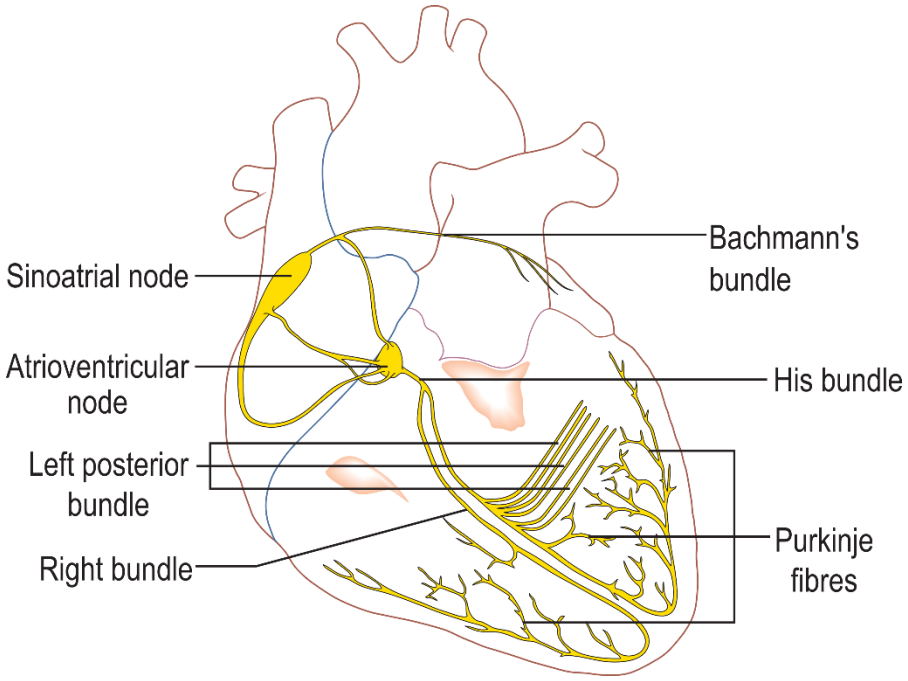

Figure 2.3: Conduction system of the heart. Adapted from the Wikimedia Commons file.

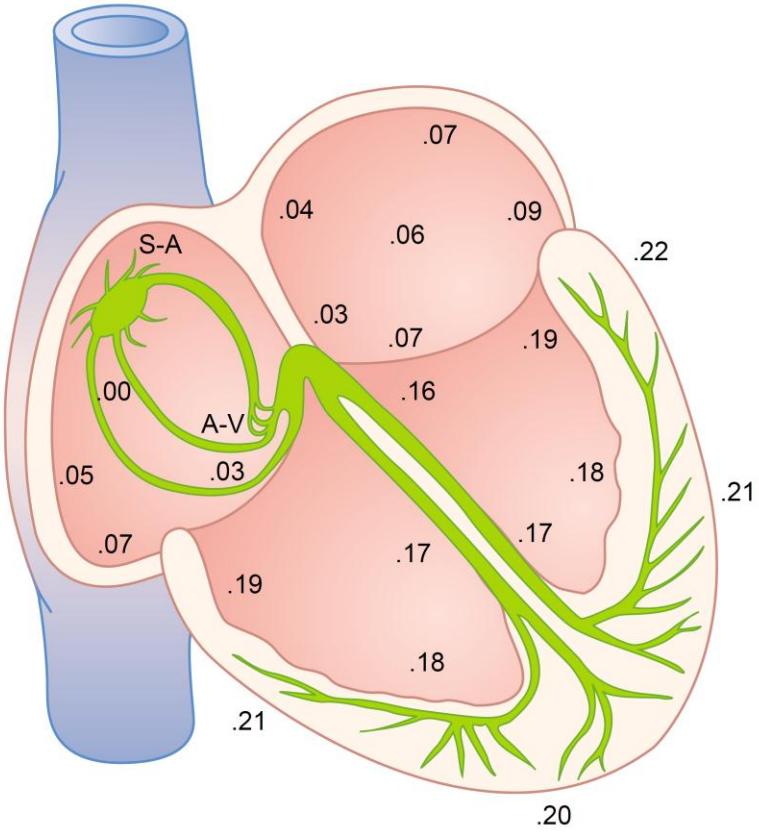

Figure 2.4: Transmission of the electrical impulse through the heart (Adapted from Guyton and Hall, 2006 [51]).

2.2 MR parameters: T1 and T2 relaxation times

The use of T1, T2 and T2*relaxation times, also known as longitudinal and transversal spin-lattice relaxation times respectively, allows the detection of multiple tissue changes [52, 53], based on hydrogen proton spin relaxation in different tissues. Clinical T1 is used to detect the presence of diffuse fibrosis while T2 is used to detect the presence of cardiac ischemia [54] and T2* to detect myocardial iron overload [55]. The use of T1 and T2 can also be combined to give an indication in terms of water and fat contents in the imaged tissue. Recently, regarding the clinical use of MTR, Weber et al. showed that the presence of myocardial infarction was associated with the decrease of magnetization transfer ratio [56]. However, although combining these parameters seems to have a great potential in detecting early doxorubicin myocardial damage, clinical studies are still lacking in the literature.

2.3 Myocardial displacement patterns analysis

Pattern analysis of myocardial deformation allows direct quantification of the cardiac function. The trajectory followed by the myocardium, from one phase to another during the cardiac cycle at each point can be quantified by a 2D or 3D vector. When the 2D or 3D myocardial wall deformation is followed during a cardiac cycle, a pattern with a specific signature is generated. However, in a pathological case where the architecture of cardiomyocyte fibers may be affected, these deformation patterns become altered and the damaged regions can be both localized geometrically and quantified in terms of 2D or 3D displacement amplitudes [35]. The advantage related to the use of myocardial displacement patterns obtained from cine MRI images is that we use the actual results in terms of myocardial deformation. Moreover, the distribution of displacements within the myocardium is directly mapped to myocardial geometry. Currently, very few tools are available for the analysis of 2D and 3D myocardial displacement patterns. Their use in the characterization and monitoring of cardiomyopathies has a great potential in understanding the pathological response of the myocardium during anthracycline-based chemotherapy but also in the development of cardio-protective treatments.

The three main techniques used to track myocardial displacements of the human heart during a cardiac cycle can be summarized as: the use of dedicated imaging sequences such as 3D cine DENSE which encode the 3D tissue displacement directly into the phase of the MR image (Hess, 2009, Zhong 2010), the use of simulated fibers directions [57, 58] (see Figure 2.5 and 2.6) or obtained by specialized sequences such as ex vivo diffusion tensor magnetic resonance imaging DT-MRI [59, 60], and the use of reconstruction techniques based on 2D imaging combined with 3D reconstruction [61-65] (see Figure 2.5 and 2.6). A concise review of several myocardial deformation tracking techniques including tagged, cine, phase contrast, DENSE and SENC MRI based technique was reported by Wang et al. (2012a) [66]. Although the mutual objectives are to allow the simulation of the cardiac cycle and to quantify myocardial tissue damage, currently, only the reconstruction-based technique allows clinical application, small reconstruction errors and guarantees realism in terms of simulations.

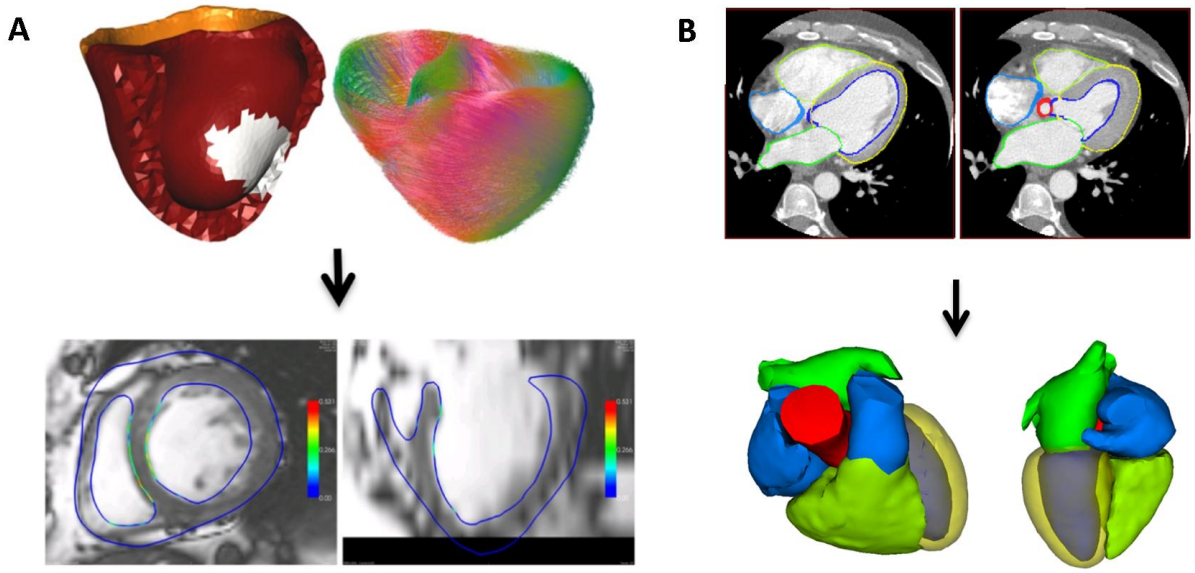

Figure 2.5: A: finite-element ventricular myocardium model obtained from cine- and DT-MRI (adapted from Sermesant et al. 2012 [61]). B: complete volumetric model of the human heart obtained from cardiovascular computed tomography data (adapted from Peters et al. 2009 [62]).

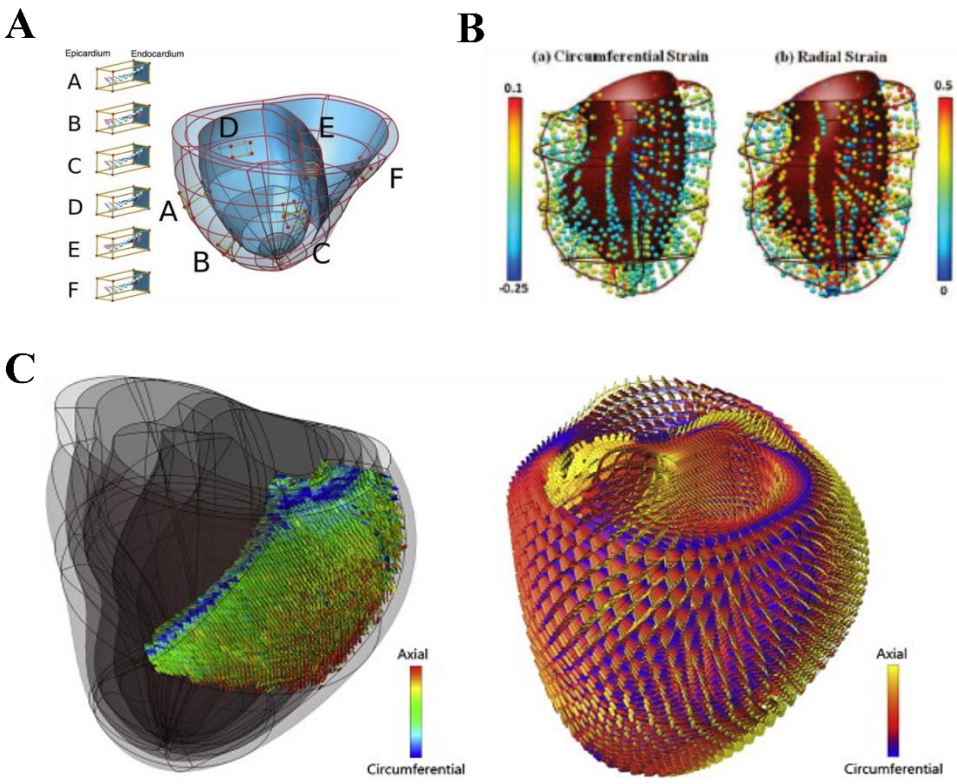

Figure 2.6: A: parametric ventricular myocardium model including simulated fibers direction (adapted from Niederer et al. 2011 [57]). B: parametric left ventricular model obtained using 2D

control curves with computed tomography data (adapted from Wang et al. 2012 [63]). C: parametric ventricular myocardium model adjusted to echocardiographic data that allow independent loading conditions simulation (adapted from Aguado-Sierra et al. 2011 [67]).

2.4 Biomechanical indices: strains and stresses

Myocardium contraction is done through coupled electromechanical excitation [68], which with the contribution of anatomical architecture of cardiac muscle fibers, generates specific patterns of ventricular volumes and pressure curves. During a normal heartbeat, the cardiomyocyte changes about 20% of its length [69]. Moreover, the organization of muscle fibers bundles that are mainly found in circular, oblique and spiral disposition gives a unique geometrical deformation of the human heart. Among reported cardiotoxic effects induced by doxorubicin, many are suspected to induce changes in terms of muscle fibers structure, function and density. However, consequences on the myocardial mechanics' part (structure and function) remain poorly understood and need to be addressed.

Myocardial muscle fibers are 1.5-3 times stiffer in the fiber direction [70, 71]. However, it is important to recall that during experimental testing, where equibiaxial loading conditions are applied in a physiological range of strains, the difference between fiber and cross-fiber directions in terms of tensile strength is significantly smaller [72, 73]. Cross-fiber loading condition is applied naturally by intra-chamber resulting pressure or by loading in the fiber direction itself which result in interaction between the different fiber bundles, i.e., directions. Moreover, there are different types of fiber directions and their exact presence, depending on the myocardial segment, are currently unclear. In terms of stress-strain relation, another factor would be the extracellular matrix. Tensile failure of the porcine extracellular matrix is relatively the same in both fiber and cross-fiber direction, whereas the tensile modulus is estimated 3 times stiffer in the fiber direction [74]. Consequently, modelling biomechanical (active and passive) myocardial parameters is a challenging task. Considering the whole myocardial structure with only myocardial fibers orientation and mechanical properties and omitting extracellular matrix properties may significantly impact the accuracy of the model.

CHAPTER 3 OBJECTIVES AND MAIN HYPOTHESES

3.1 Context of doxorubicin-induced cardiotoxicity

In the context of doxorubicin-induced cardiotoxicity, it is important to evoke the need to early detect myocardial damage induced by doxorubicin-based chemotherapy, especially in children where delayed cardiotoxicity may manifest years or decades after treatment. A major difficulty associated with the development of cardioprotective agents is related to the timing of the various cardiotoxic effects and the triggering mechanisms which currently remain unclear. Two questions related to this issue will be studied during this doctoral project: *What cardiomyopathies are induced by doxorubicin-based chemotherapy that can be detected by MRI?* and *Do these doxorubicin-induced cardiomyopathies alter the myocardial function?*

To answer these two questions, we will need to acquire cardiovascular images from cancer survivors and investigate them to explore the whole spectrum of anthracyclines-related cardiotoxicities on the myocardial tissue. Currently the cardiotoxicities that arise with anthracyclines-based treatment are not clear enough and the literature is lacking studies that investigate anthracyclines cardiotoxicity using cardiovascular magnetic resonance imaging (MRI). Our choice of using MRI instead of echocardiography or other imaging techniques relies on the fact that MRI remains the gold standard when it comes to investigating cardiomyopathies in general. On the other hand, MRI provides the most advanced imaging sequences such as cine MRI and T1 and T2 imaging susceptible to detect any alteration in the myocardium. For this reason, MRI was selected as the main imaging modality.

3.2 Objectives and hypotheses

In this context, the proposed objectives and hypotheses underlying this doctoral project are:

1) Review doxorubicin-induced cardiotoxicity
2) Evaluate MR parameters, including pre- and post-gadolinium T1 and T2 relaxation times, sensitivity to detect myocardial damage induced by doxorubicin chemotherapy. The assumption underlying this part of the project is that MR parameters (T1 and T2) are sensitive in the detection of doxorubicin-induced cardiotoxicity

3) I) Propose a quantitative method to estimate the effect of doxorubicin-based treatment in cancer survivors on myocardial displacement patterns using cine cardiovascular MR (cine-CMR). The hypothesis underlying this part of the project is that doxorubicin chemotherapy induces direct damage to myocardial fibers architecture which can be detected through myocardial displacement patterns analysis.

   II) Evaluate clinical indices' sensitivity to detect changes in the myocardial function (both systolic and diastolic) following doxorubicin chemotherapy. Thus, the assumption underlying this project is that clinical indices are sensitive in the detection of doxorubicin-induced cardiotoxicity.
4) Develop a method based on cine MRI associated to a finite element model of the myocardium to evaluate mechanical properties changes within the myocardium in children receiving doxorubicin therapy for leukemia. The main hypothesis underlying this part of the project is that doxorubicin treatment induces significant changes to myocardial mechanical properties, i.e., contractile function.

An article is proposed for each objective (see Figure 3.1) and the long-term objective of this project is to develop new diagnostic tools to characterize early myocardial degeneration using the most sensitive imaging-based biomarker and the underlying hypothesis is that doxorubicin-based treatment induces important changes to myocardial function in children receiving doxorubicin-based chemotherapy.

The overall approach of this research work is based on acquiring cardiovascular images from acute lymphoblastic leukemia survivors, including cine MRI and T1 and T2 images and analyse them to extract myocardial characteristics. Firstly, cardiovascular T1 and T2 images will be acquired and segmented to extract myocardial T1 and T2 signal. This myocardial signal will further be analysed to determine whether T1 and T2 sequences are sensitive in the detection of doxorubicin-induced cardiotoxicity. Secondly, using cine MRI images, the myocardial area will be segmented to extract myocardial displacement patterns during the cardiac cycle. These patterns of displacement will further be analysed and compared between the different groups, i.e., cancer survivors at high risk, cancer survivors at low risk and healthy volunteers. Likewise, the effect of doxorubicin-based treatment on myocardial displacement patterns will also be investigated. Finally, using myocardial displacements obtained from cine MRI images, myocardial strains and stresses will be estimated using a hyperelastic finite-element model and compared between the different groups to determine

whether doxorubicin-based therapy induces mechanical properties changes in the same cohort of acute lymphoblastic leukemia survivors.

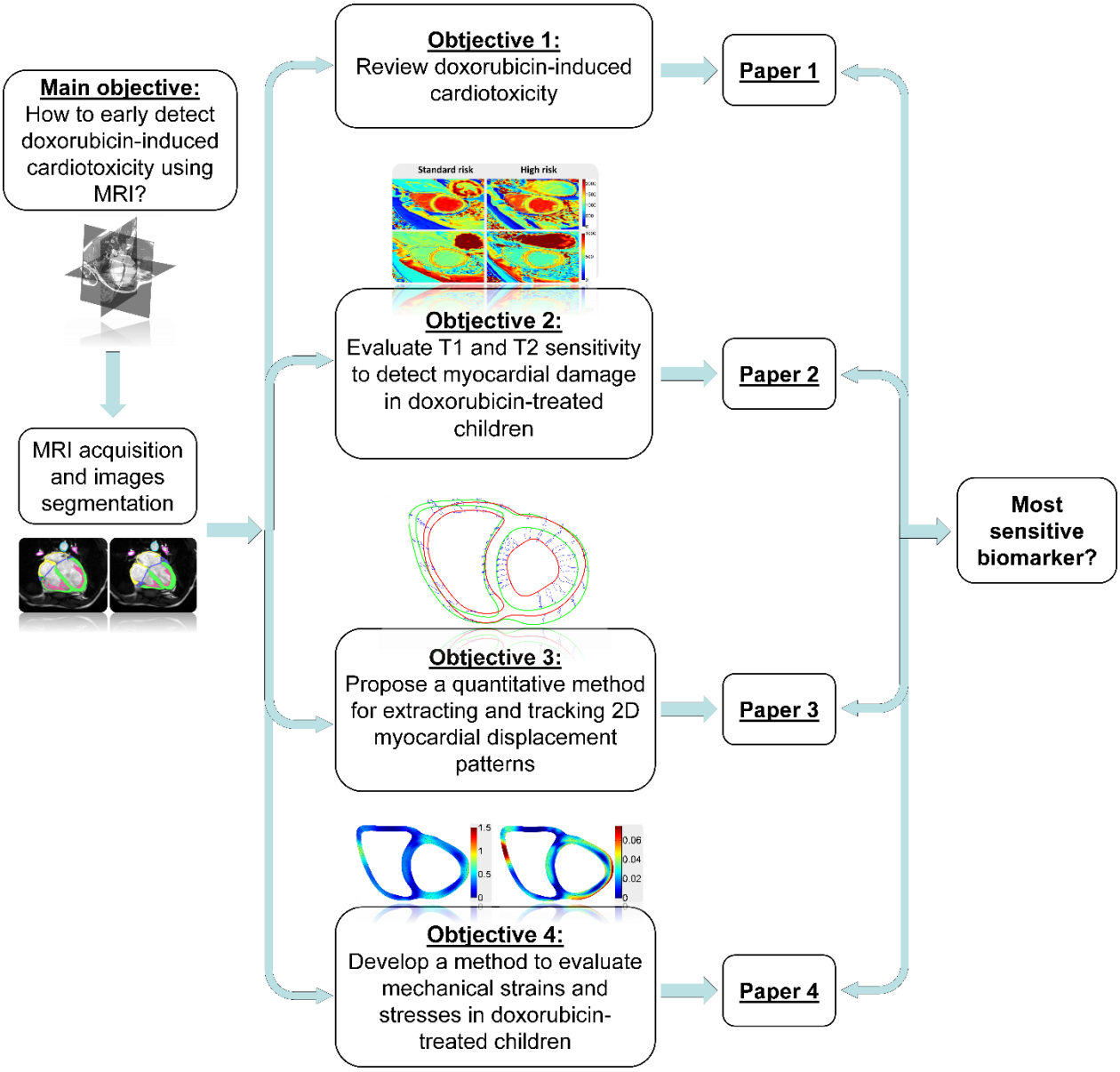

Figure 3.1: Study diagram.

CHAPTER 4 ARTICLE 1: IMAGING OF EARLY MODIFICATION IN CARDIOMYOPATHY: THE DOXORUBICIN-INDUCED MODEL

Mohamed Aissiou[1,2], Delphine Périé[1,2], Farida Cheriet[2,3], Nagib S. Dahdah[2], Caroline Laverdière[2], Daniel Curnier[4].

[1] Mechanical Engineering Department, École Polytechnique de Montréal, Montreal, Canada

[2] Research Center Sainte-Justine University Hospital, Montreal, Canada

[3] Computer Engineering Department, École Polytechnique de Montréal, Montreal, Canada

[4] Kinesiology Department, University of Montreal, Montreal, Canada

4.1 Abstract

Doxorubicin chemotherapy is effective and widely used to treat acute lymphoblastic leukemia. However, its effectiveness is hampered by a wide spectrum of dose-dependent cardiotoxicity including both morphological and functional changes, affecting primarily the myocardium. Non-invasive imaging techniques are used for the diagnosis and monitoring of these cardiotoxic effects. The purpose of this review is to summarize and compare the most common imaging techniques used in early detection and therapeutic monitoring of doxorubicin-induced cardiotoxicity and the suggested mechanisms of such side effects. Imaging techniques using echocardiography including conventional 2D and 3D echocardiography along with MRI sequences including Tagging, Cine, and quantitative MRI in detecting early myocardial damage are also reviewed. As there is a multitude of reported indices and imaging methods to assess particular functional alterations, we limit this review to the most relevant techniques based on their clinical application and their potential to early detection of doxorubicin-induced cardiotoxic effects.

4.1.1 Keywords

Anthracycline, Doxorubicin, Cardiotoxicity, Acute lymphoblastic leukemia, Childhood cancer.

4.2 Introduction

Doxorubicin chemotherapy is part of the standard treatment regimens for children with acute lymphoblastic leukemia [2]. However, its effectiveness is hampered by a wide spectrum of dose-

dependent cardiotoxicity including morphological changes such as myofibril loss and diffuse fibrosis and several resulting functional changes such as progressive ventricular dysfunction and late congestive heart failure [4]. While mechanisms underlying doxorubicin cardiotoxicity remain uncertain [39], characterizing their effect on the myocardium would help not only diagnosing myocardial damages and monitoring future cardioprotective treatments, but would also bring insights as to which metabolic and regulatory pathways are involved. In this review, we will attempt to explore whether the current cardiovascular imaging techniques are sensitive enough for early detection and monitoring of doxorubicin-induced cardiotoxicity. We will also attempt to explore if the recent exploratory techniques are clinically relevant and feasible.

The first section will describe the doxorubicin-induced dose-dependent cardiotoxicity including: histological findings, functional and morphological damage and incidence of late cardiotoxicity. The second section will review the proposed mechanisms underlying anthracycline-induced cardiotoxicity. The third section will review current imaging techniques, their potentials and their limitations to detect early changes preceding low cardiac output in doxorubicin-induced cardiomyopathy including 2D and 3D echocardiography as well as cardiovascular MRI. The last section will conclude on the relevance of cardiovascular imaging to detect doxorubicin-induced cardiotoxicity and its progression.

4.3 Doxorubicin-induced dose-dependent cardiotoxicity

The probability of a doxorubicin-induced congestive heart failure is related to the total dose of administered doxorubicin. The linear correlation between the probability of secondary cardiomyopathy and the cumulative dose starts at around 4% when the cumulative dose is 500–550 mg/m^2, and increases to 18% at 551–600 mg/m^2, to 36% when it exceeds 600 mg/m^2 [5], and up to 50% at a dose of 1000 mg/m^2 [75, 76]. The difference between the lower and the upper therapeutic range is rather small, but the consequence of either side of this therapeutic range could be life-threatening [77], on one side by insufficient dose to complete remission and on the other side by excessive dose inducing potentially irreversible cardiotoxic effects. In a retrospective study of 4018 patients, early results yielded an overall incidence of drug-induced congestive heart failure of 2.2% [31]. Moreover, a weekly dose schedule of doxorubicin administration is associated with a significantly lower incidence of congestive heart failure than the 3-week schedule. Several clinical factors known to predispose for cardiomyopathy include age (>65 years), simultaneous

administration of other antineoplastic agents that are damaging to the myocardium, method of doxorubicin administration, previous cardiac disease and combination of multiple therapies [2, 28, 78]. Nevertheless, characteristics such as patient's ability to carry on normal activities, sex, race, and tumor type were not risk factors [31]. Moreover, some patients may tolerate higher doses than the acceptable threshold [76], while others may experience late cardiotoxic effect at even low doses [79], suggesting other factors, such as genetic predisposition, may play in individual response to the therapy. The pharmacokinetics of doxorubicin remain variable between patients. In children, body surface area is preferred to body weight or lean body mass for dose normalization. Notwithstanding, inter-patient dose variation results in up to 5-fold of the maximum doxorubicin plasma level in children [77].

The genetic factor may also explain the inter-individual variations in the cardiac response to doxorubicin treatment. Although the topic has not been extensively studied [80, 81], there is an advocated need to assess genetic predispositions to doxorubicin cardiotoxicity [82, 80, 81]. Carbonyl reductase (CBR) mediated reduction of anthracycline to cardiotoxic alcohol metabolite is believed to be a major metabolic route implicated in the pathogenesis of cardiotoxicity [83, 84]. Patients with CBR3 V244M homozygous G genotype are at an increased risk of cardiotoxicity at doses as low as 101-150 mg/m^2 [84]. Other genes polymorphisms such as in GATA-4 [85] or histamine N-ethyl transferase [86] may also be important in the assessment of individuals predisposition to doxorubicin cardiotoxicity. However, as reactive oxygen species generation and subsequent lipid peroxidation could be responsible for most if not all subsequent events including alterations in gene expression [87], knowing the relative timeline of the genetic factor relative to reactive oxygen species generation is crucial.

4.3.1 Histological findings

Chemotherapy induced cardiomyopathy has been studied invasively with endomyocardial biopsy. Accordingly, at cumulative doses exceeding 200 mg/m^2, 68% of patients had Billingham (modified scale) biopsy grades of 1.0 or higher with no correlation between the cumulative dose and the biopsy grade [32]. The presence of areas with patchy myocardial interstitial fibrosis and scattered vacuolated myofibrillar loss [28, 4], a loss of muscle fibers and an increase in the amount of interstitial tissue as well as the disruption of the syncytial pattern seen in normal myocardium were noted [5]. The presence of vacuolization of cardiomyocytes and edema (Figure 4.1) as early as 24

h after a single injection of 2.5 mg/kg in rats along with condensation of the nucleus, shrunken appearance of the cardiac myocyte, gradual dose-dependent decrease in the staining intensity and disorganization of cross-striated staining patterns were also observed [29]. Enlarged T-tubules and distension of the sarcoplasmic reticulum with disarray and mitochondrial loss were demonstrated in rats previously treated with doxorubicine, while higher cumulative doses were associated with mitochondrial degeneration, myofibrillar disarray and edematous cardiomyocyte with even the absence of subsarcolemmal mitochondria [21]. Interestingly, interstitial and perivascular fibrosis [35] at midventricular level in rats myocardium were reported, suggesting the presence of both extra- and intracellular mechanisms. Early changes may also include signs of dose-dependent inflammatory cells infiltration and myocardial fibrosis [30]. However, most of these histologic findings are associated with relative high cumulative doses, although, they may appear at much smaller doses in the absence of measurable cardiac dysfunction [88].

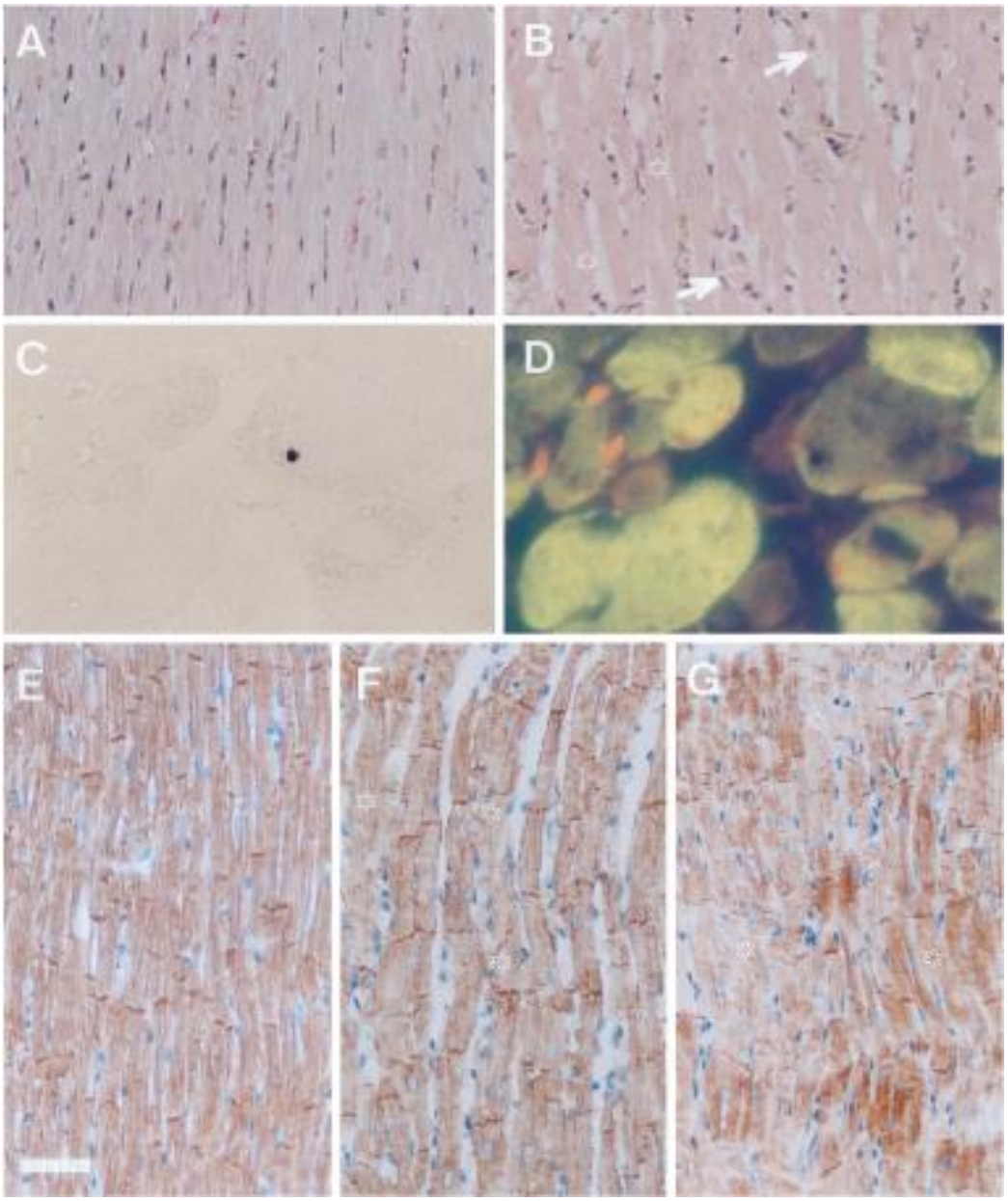

Figure 4.1: Histologic section of rat myocardium. a) Control. b) 24 h after a single injection of 2.5 mg/kg. c) TUNEL-positive nucleus at 24 h post injection of 2.5 mg/kg. d) Double staining with antimyosin. e) Control rat myocardium. f) Myocardium after a single injection of 2.5 mg/kg. g) Myocardium after a cumulative dose of 15 mg/kg.[Adapted from Arola et al. (2000)].

4.3.2 Functional and morphological changes: effects on the cardiac pump

Most patients experiencing anthracycline-associated cardiotoxicity show evidence of cardiac dysfunction within the first 6 months after therapy [34]. Early dose-dependent functional changes of the cardiac pump are witnessed clinically and at necropsy including: increased heart rate [40], increased diastolic blood pressure and heart weight, abnormal systolic time intervals [28] and ventricular dilatation [28, 4]. The electrocardiogram may reveal initial arrhythmia, most commonly sinus tachycardia [31, 2], nonspecific ST-T changes [31, 32, 4], left axis deviation and non-sustained supraventricular tachycardia with premature atrial and ventricular beats [4], decreased amplitude of QRS complexes [5, 28], premature ventricular contraction, as well as features suggestive of myocardial infarction [31]. Cardiac ventricular function changes in both animal and human studies include diastolic dysfunction with wall stress increase and wall thickness dysfunction [7, 4], fractional shortening and ejection fraction decrease [33, 34, 8, 4], reduction in radial strain (transmural profiles amplitude of myocardial strain in the radial direction of the left ventricle) associated with histologic indices of myocardial injury [35], progressive effect in reduced contractility and increased afterload [89] and congestive heart failure [5, 9].

4.3.3 Late toxicity incidence

When myocardial damage involves a critical mass of cardiomyocytes, the heart expands in size and the chamber walls become thinner which lead to a dilated cardiomyopathy with reduced contractile function [90]. The acute form of doxorubicin cardiotoxicity may manifest itself within 24 h of infusion, while chronic cardiotoxicity may take as long as 4 to 20 years at post-treatment [91]. While most doxorubicin cardiotoxicity occur within the first 6 months after therapy, patients developing late doxorubicin-induced cardiomyopathy seem to have milder cardiac decompensation and better chances for functional improvement [34]. In a long term echocardiography follow-up of acute lymphoblastic leukemia survivors treated with either 180 or 240 mg/m^2 of anthracycline, no clinically relevant cardiac damage was tangible. In contrast, subclinical abnormalities were described mostly by a decrease in the isovolumetric relaxation time and Tei-index of the left ventricle 13.3 years following treatment [92]. With cumulative doses under 450 mg/m^2, the diagnosis and monitoring of late cardiotoxicity remains important even beyond the first year after of follow-up [35], especially in the pediatric and young adult population [93, 94, 79, 33]. Overall, it is agreed that the cumulative loss of mature cardiomyocytes leads to heart failure because of a

very limited proliferative potential during a life time [95]. Hence, early detection of cardiac toxicity may be essential for establishing early intervention for better outcome.

4.4 Mechanisms underlying anthracycline-induced cardiotoxicity

Mechanisms (Table 4.1) behind doxorubicin-induced cardiotoxicity are still uncertain. Numerous evidence suggest a signaling pathway involving reactive oxygen species generation and lipid peroxidation, perturbation of calcium handling, inhibition of gene expression [95] and induced cell death through both apoptosis and necrosis [96].

Table 4.1: Mechanisms underlying Anthracyline-induced cardiotoxicity.

Proposed mechanism	Induced cadiotoxicity	Reported changes	Description
ROS generation and lipid peroxidation [11-13, 97]	Membrane lipid perooxidation	↑ NADPH oxidation level ↑ TBARS concentration	Detected as early as 1 h
Mitochondrial damage [14-18]	Cardiomyocyte dysfunction	Mitochondrial membrane potential reduction	Early effect ROS generation dependant Detected as early as 5 min post-treatment
Inhibition of DNA and protein synthesis [98]	-	Early and late DNA damage patterns	Dose-dependent DNA damage
Apoptosis and Necrosis [25, 26, 97, 27]	Acute cardiomyopathy Myocardial damage	Caspase-3 activation Inhibited by antioxidants ↓ membrane integrity	P53 independent Detected at few hours post-treatment
Perturbation of Ca2+ handling [19-21]	Reduced contractility	SR Ca^{2+} release channels alteration ↓ [3H]Ryanodine binding ↑ SR Ca^{2+} release rate ↓ mitochondrial calcium loading	Results from ROS generation

4.4.1 Reactive oxygen species generation

Reactive oxygen species are generated in a redox cycle, in addition to metabolic pathways for elimination, by a univalent reduction of doxorubicin to a semiquinone radical which can rapidly auto-oxidize in the presence of oxygen to generate superoxide anions [14]. Reactive oxygen species generation may alter many components of the cardiomyocyte near their site of generation, including membrane lipids, mitochondria and nucleic acids. The presence of anthracycline-induced lipid peroxidation was demonstrated [11, 12]. Adryamicin induced 30%-50% concentration increase of lipid peroxidation byproduct assessed using thiobarbituric acid reactive substances level in rats during 1 to 24 h post-treatment with a cumulative dose of 15 mg/kg [13] while more than 2-fold increase in mice treated with a higher cumulative dose of 25 mg/kg [99]. A long-term oral administration of nitrate, between 7 days pre-treatment and 5 days post-treatment with doxorubicin) decreased significantly the malondialdehy and 4-hydroxyalkenals concentration levels in mice [100, 101, 18]. Moreover, the resulting changes were reversed by the use of antioxidants such as FP15 [99] and Probucol [13] which interestingly does not seem to interfere with antitumor activity of anthracycline. However, a common limiting factor in these studies resides in the limit of the assay sensitivity and specificity to quantify lipid peroxidation that remains hitherto controversial [102].

Mitochondria, representing 25% to 35% of the cardiomyocyte volume, are believed to be the primary targets in Adriamycin cardiotoxicity [14]. Several mitochondrial enzymes such as NADH dehydrogenase, cytochrome P-450 reductase and xanthine oxidase are involved in generating oxygen free radicals [103-106]. Mitochondrial damage, based mainly on reactive oxygen species generation, is demonstrated by numerous studies [15-18]. Very low concentration of doxorubicin induced mitochondrial membrane potential reduction which was followed by apoptosis within approximately 6 h [15]. Interestingly, superoxide production in mitochondria was seen as early as 5 min within doxorubicin treatment followed by a release of the pro-apoptotic protein cytochrome c [15]. In the neonatal rat ventricular cardiomyocyte, reactive oxygen species generation was localized in the mitochondria associated to a decrease in mitochondrial and MnSOD activity with increased cardiomyocyte death and mitochondrial membrane depolarization, changes that were reversed by the antioxidant and stilbenoid Rasveratrol [16]. Moreover, mitochondrial damage was seen in tumor cell line MTLn3 but not in H9c2 cells [17], which raise great concern about the different signaling mechanisms and development of further cardioprotective agents. Doxorubicin

strongly downregulated the stable expression of the cytochrome c oxidase subunits II and Va, while Mito-Q, a mitochondria-targeted antioxidant, restored them [107]. Long-term oral administration of nitrate in mice significantly reduced mitochondrial complex I and hydrogen peroxide H_2O_2 generation and partially restored the cardiac function [18]. Conversely, the study did not investigate the interference of the agent in tumor cells.

Inhibition of nucleic acid and protein synthesis is also a potential consequence of anthracycline-induced reactive oxygen species generation [39]. At clinically relevant concentration of doxorubicin, two different DNA damage patterns were present in rats cardiomyocyte cell line H9c2 [98]. The first one occurs early and may be completely repaired within two hours, while the second is seen within several hours and may be responsible for p53 activation. Interestingly, chemical inhibition of p53 prevented cell death but not DNA damage, which is in concordance with the p53 being activated only when DNA damage exceed repair capacity.

4.4.2 Apoptosis

Apoptosis is the second main mechanism and is believed to be responsible for myocardial damage [108, 109, 25]. The mechanism is not involved in chronic cardiomyopathy [96] and is believed to induce acute rather than progressive chronic cardiomyopathy [29]. Furthermore, different regulatory mechanisms may be activated depending on the cumulative dose of doxorubicin [26]. Caspase-3 activity increases significantly in rats cardiomyocyte incubated with Doxorubicin [25]. On the other hand, Caspase-3 activation was significantly reduced when the cardiomyocyte was pre-treated with the metalloporphyrin antioxidant FeTBAP. The study suggested that apoptosis was induced by a H_2O_2-mediated mechanism that is independent of p53 activation [25] which is in agreement with previous studies asserting that the downstream effectors in apoptosis can also be activated independent of p53 [110]. Caspase-3 activity increase in H9c2 cardiomyocyte cell line was maximally detected 8 h after doxorubicin addition and preceded significant sub-G1 cells increase detected at 72 h, whereas elevation in reactive oxygen species generation was detected as early as 1 h post-treatment [97]. Fortunately, differences in terms of kinetics and order of mechanisms triggeing events between toxicity in tumor cells and cardiomyocyte are suggested, especially in the mitochondrial transmembrane potential and mass changes during treatment [17]. Doxorubicin induced different apoptosis mechanisms in normal (H_2O_2-dependant) and tumor (P53-dependant) cells [25] while doxorubicin along with daunorubicin led to immediate loss of

membrane integrity and resulted in cell death via necrosis, but not through apoptosis as assessed by caspase activity [27]. However, apoptosis happened only at high doxorubicin doses while lower doses are more likely to induce cell death through mitotic catastrophe [26]. The process order was reactive oxygen species formation, mitochondrial membrane depolarization, cytochrome c release, caspases-3 activation, followed by DNA fragmentation [110], which is in concordance with cardiomyocytic apoptotic mechanisms. However, at this point, no study confirmed the time course of doxorubicin-induced apoptosis in the cardiomyocyte.

4.4.3 Anthracycline-induced alteration of calcium handling

The last but not least mechanism is related to anthracycline-induced alteration of calcium handling [39, 111]. Early results in rabbits pre-treated with doxorubicin demonstrated a dose-dependent increase in the probability of open-state of the SR Ca^{2+} release channels [112], a decrease in the amount of SR Ca^{2+} release channels and [3H] Ryanodine binding [113], or an increased SR Ca^{2+} release rate and decreased in *vitro* contractility of the cardiomyocyte, particularly after resting intervals [20]. The mRNA expression levels decreased for proteins responsible for Ca^{2+} uptake (SERCA2) and release (ryanodine receptor) [19]. Proteins that regulate the influx and efflux of Ca^{2+} across the plasma membrane remained stable however, and no extensive damage was seen at histology with the corresponding dose. Alterations in Ca^{2+} are suggested by these studies to result commonly from anthracycline-induced reactive oxygen species generation, mainly at the mitochondrial level [114]. Such alterations are important to the cardiac function since Ca^{2+} homeostasis is closely related to the cardiomyocyte contraction [115]. The most common site resulting in perturbation of calcium handling is the sarcoplasmic reticulum [19, 20], which includes one of the main calcium channels, the SR Ca^{2+}-ATPase. Calcium dysregulation may be both a result and a cause of reactive oxygen species generation [116]. On the other hand, doxorubicin-induced cardiac dysfunction can occur in the presence of impairment of RYR2 mRNA expression level but also in the absence of significant dysfunction to SR Ca^{2+} loading ATPase [117]. RYR2 expression, thought mRNA levels, protein concentrations and Bmax, was also correlated to the decrease in left ventricular fractional shortening at echocardiography [117]. Correlations were further found between decreased mitochondrial calcium loading capacity and cumulative doxorubicin dose in rats [21]. Nevertheless, the triggering event in the suggested doxorubicin-induced Ca^{2+} homeostasis perturbation and implication of other potential channels such as

mitochondrial Ca^{2+} uniporter and the plasma membrane Ca^{2+} ATPase is unclear. Whether these mechanisms are precursors or directly resulting from doxorubicin treatment is a question that remains open.

4.5 Imaging techniques

The "gold standard" for the detection of acute doxorubicin myocardial damage remains endomyocardial biopsy of the right ventricle as it provides the greatest reliability and sensitivity [118, 2, 43]. Endomyocardial biopsy is also used to grade the severity of doxorubicin-induced cardiotoxicity [103, 119, 120]. However, the disadvantage of this technique is that it is invasive, with inherent risks requiring experience and appropriate training [4]. On the other hand, the standard non-invasive screening includes 12-lead electrocardiogram at baseline and at the end of therapy despite its limited capacity to detect early toxicity with certainty [44]. These two methods represent the two edges of the "screening" spectrum and are limited by the invasiveness of the first and the lack of diagnostic power of the second. Hence, other screening means have been used in an effort to validate potential cardioprotective agents [121] but are known to lack sufficient predictive power of patients at higher risk [122, 123].

4.5.1 Echocardiography

Recent developments provided significant improvement to echocardiography image quality and recommendations for its use [124]. Echocardiographic measurements of left ventricular fractional shortening and ejection fraction have always represented the basic measurements in assessing anthracycline cardiotoxicity [45, 44], particularly in children [125, 4]. However, in the setting of anthraycline-induced cardiotoxicity, these indices may not provide the same sensitivity. In an echocardiographic study including 108 survivors of childhood cancer, measurement of ejection fraction had a sensitivity of 25% to detect fractions less than 50%, and a false negative rate of 75%, while 3D echocardiography had 53% and 47% respectively using MRI as a reference [126]. Despite the reported high prevalence of reduced ejection fraction and cardiac mass among the patients, even in low-dose anthracycline, a larger cohort is required due to the absolute number of patients with reduced ejection fraction and cardiac mass. Although, both 2D and 3D echocardiography may accurately estimate the ejection fraction and provide similar results to cardiovascular MRI, area

and volume measurement are known to be underestimated, particularly in the presence of dilated cardiomyopathy [127].

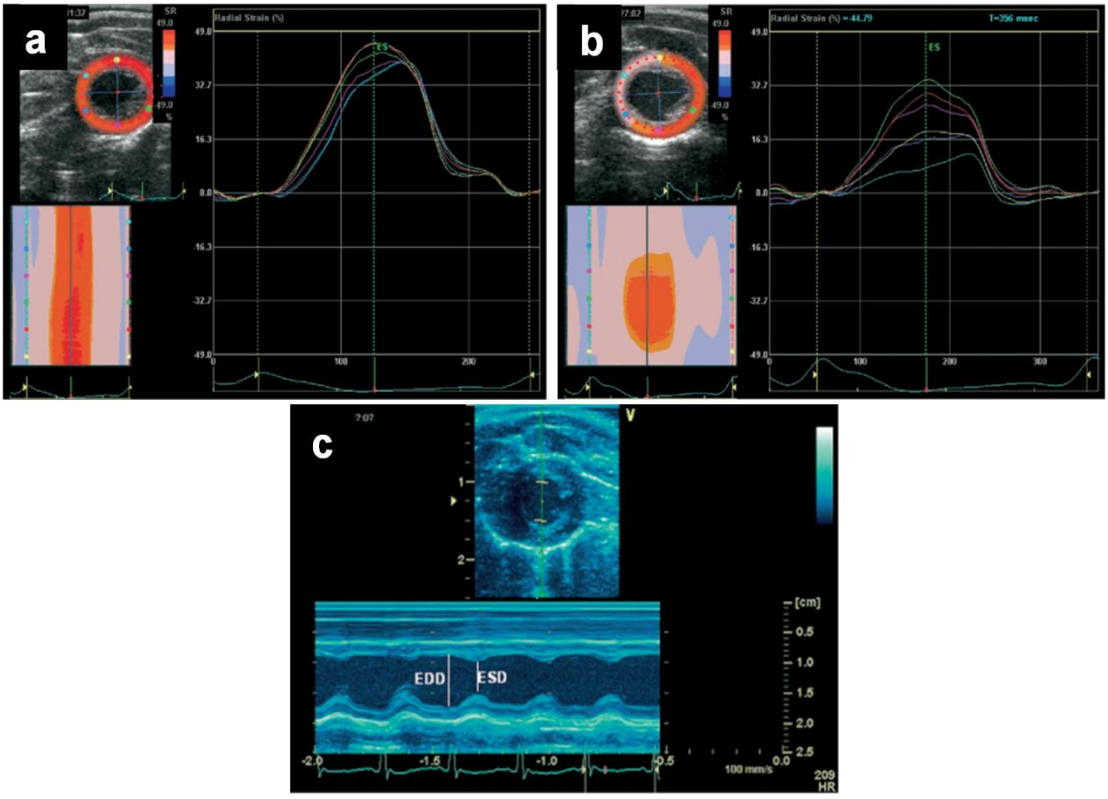

Figure 4.2: 2D radial strain analysis in a doxorubicin treated rat using echocardiography. a) At Baseline. b) At 12 weeks. c) Fractional shortening using anatomical M-mode.[Adapted from Migrino et al. (2008)].

Using high cumulative doses in rats resulted in a significant 2D Doppler radial strain reduction (Figure 4.2) at 8 weeks which was further associated with histologic indices of myocardial damage and directly related to cardiac mass while inversely related to caspase-3 activity [35]. Doppler derived strain and strain rate measurement provide higher sensitivity and specificity than the measurement of ejection fraction in detecting early myocardial abnormalities during doxorubicin treatment [128]. At two weeks, myocardial damage was induced, as confirmed by histologic examination and was only detectable by strain and strain rate measurements, whereas standard echocardiographic parameters (dimensional and ejection fraction measurements) and myocardial

velocities were able to detect only delayed changes [128], including fractional shortening detection at 12 weeks [129]. Interestingly, even if the inter- and intraobserver scores in 2D strain echocardiography may be poor to moderate in the two-chamber view, the reliability scores seems to provide high reproduction values in almost all views [130]. Nevertheless, based on left ventricular shortening fraction and ejection fraction measurements, routine echocardiograms do not represent the ideal surveillance as they rarely identify cardiac damage significant enough to impact therapeutic decisions [131] despite baseline echocardiography screening assessment prior to chemotherapy [132].

Beyond the systolic function, studying diastolic function parameters seems to provide an added value to echocardiography. In a preliminary study on adult patients treated with anthracycline cumulative dose of 211 ± 82 mg/m^2, significant changes in the diastolic function were reported within 3 months after treatment, whereas at 3 years, more pronounced changes in both diastolic and systolic function were seen, using both conventional and tissue Doppler echocardiography [129]. Another study including a series of 28 patients treated with anthracycline (212 ± 15 mg/m^2), echo Doppler quantification of the E-wave (mitral valve at early filling), A-wave (mitral valve during atrial contraction) and the ratio E/A demonstrated better detection potential than the common ejection fraction index [133]. Figure 4.3 shows a diastolic dysfunction with preserved normal systolic function in a patient following doxorubicin chemotherapy.

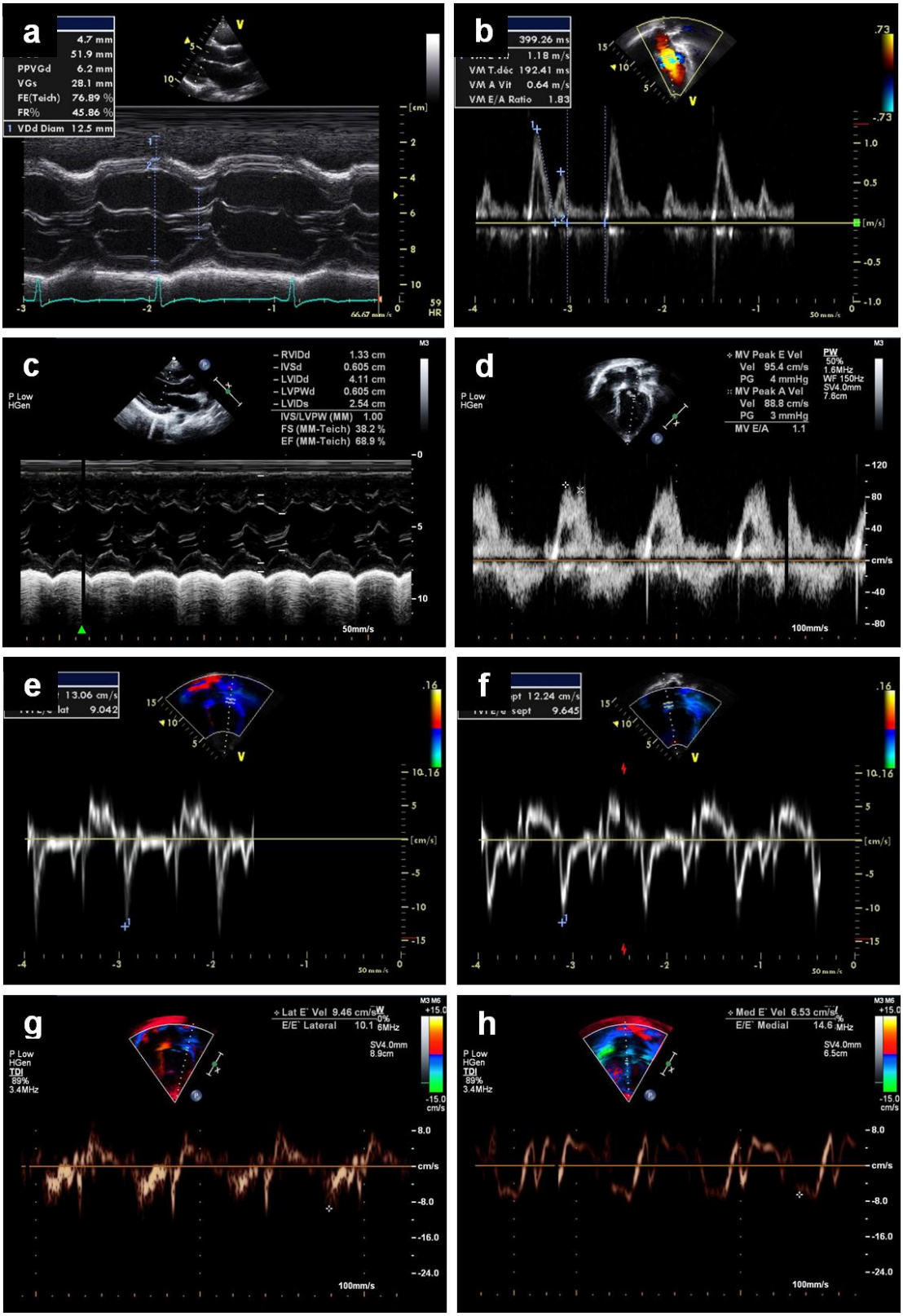
a
4.7 mm
51.9 mm
PPVGd 6.2 mm
VGs 28.1 mm
FE(Teich) 76.89 %
FR% 45.86 %
1 VDd Diam 12.5 mm
b
399.26 ms
1.18 m/s
VM T.déc 192.41 ms
VM A Vit 0.64 m/s
VM E/A Ratio 1.83
c
P Low
HGen
RVIDd 1.33 cm
IVSd 0.605 cm
LVIDd 4.11 cm
LVPWd 0.605 cm
LVIDs 2.54 cm
IVS/LVPW (MM) 1.00
FS (MM-Teich) 38.2 %
EF (MM-Teich) 68.9 %
50mm/s
d
P Low
HGen
MV Peak E Vel
Vel 95.4 cm/s
PG 4 mmHg
MV Peak A Vel
Vel 88.8 cm/s
PG 3 mmHg
MV E/A 1.1
100mm/s
e
13.06 cm/s
f
12.24 cm/s
g
P Low
HGen
TDI
Lat E` Vel 9.46 cm/s
E/E` Lateral 10.1
100mm/s
h
P Low
HGen
TDI
Med E` Vel 6.53 cm/s
E/E` Medial 14.6
100mm/s

Figure 4.3: In this patient with normal myocardial systolic and diastolic function (**a** and **b**), features of diastolic dysfunction following doxorobucin chemotherapy are evidenced by mitral inflow velocity fusion of early and late phase filling (**c** and **d**). Diastolic function was also evaluated by tissue Doppler analysis (E/E' ratios) of the septal and lateral walls of the left ventricle (**e** and **f**), as demonstrated in this patient with reduced left ventricle relaxation leading to increased E/E' ratios (**g** and **h**). **a)** Systolic function (ejection fraction 76.9%). **b)** Mitral inflow (E/A = 1.83). **c)** Preserved normal systolic function (ejection fraction 68.7%). **d)** Compromised mitral inflow (E/A = 1.1) **e)** Normal lateral wall relaxation with E/E'= 9.04. **f)** Normal septal wall relaxation with E/E'= 9.64. **g)** Reduced lateral wall relaxation with borderline E/E'= 10.1. **h)** Reduced septal wall relaxation with increased E/E'= 14.6.

Exercise echocardiography is known to be more sensitive to early subclinical changes [134, 45, 135]. At 6 months post-treatment, exercise echocardiography on doxorubicin treated children is more sensitive to assess cardiotoxicity, while ECG and 24 h Holter monitoring are less sensitive [45]. However, the reported cumulative doxorubicin dose used in that particular study was relatively low. At 12 month post-treatment, exercise echocardiography on doxorubicin treated children is also more sensitive to reflect dose-dependent anthracycline subclinical abnormalities than conventional echocardiography [135]. Above all, ejection fraction and fractional shortening changes do not seem to be associated with cumulative dobutamine dose for anthracycline-induced cardiotoxicity detection, which raise concerns about the predictive power of these commonly used indices both in rest and stress condition [133, 136]. Similarly, and to compensate for the relatively limited utility of resting echocardiographic evaluation, dynamic evaluation has been proposed. In this perspective, a challenge test with dobutamine, a sympathomimetic agent, was demonstrated to enhance the detection of anthracycline-induced cardiotoxicity, especially in children [137, 133, 136]. Systolic and diastolic changes were found in 85% of children over 2 years old previously treated with moderate cumulative doses of anthracycline [137]. Whereas at rest 26% of them showed increased wall stress, the detection rate rose to 52% during dobutamine stimulation. Similarly, exercise detection of anomalies seems to elucidate a degree of predisposition to future cardiac deterioration [137].

Further echocardiographic indexes may also provide sensitivity to early anthracycline-induced cardiotoxicity such as the Tei-index, a Doppler based myocardial performance index, to evaluate the severity of myocardial combined systolic and diastolic dysfunction [138, 139]. Significant difference in the Tei-index between patients groups receiving either >200mg/m^2 or <200mg/m^2, while no significant differences in left ventricular ejection fraction and fractional shortening were observed [140]. The peak oxygen uptake (pVo2) and anaerobic threshold were significantly decreased in patients treated with anthracycline and exercise intolerance was further associated with increased Tei-index [141]. Changes in the Tei-index may also be useful for early cardiotoxicity detection. On 23 patients with hematological malignancies receiving doses below 420 mg/m^2, Tei-index variations significantly correlated with doses variations, but not with left ventricular ejection fraction variations [142].

Other echocardiographic techniques, such as 3D echocardiography may further enhance the performance of conventional 2D echocardiography [143]. For instance, left ventricular function and volume measurements seem to be better estimated in 3D compared to 2 D imaging [144]. Other enhancements could be brought by the use of contrast agents with optimized definition of the endomyocardium [145].

4.5.2 Magnetic Resonance Imaging

Although echocardiography is inexpensive and readily available clinically, MRI remains currently an alternative method used for myocardial function and perfusion evaluation, as well as for tissue characterization [146, 46, 147]. To assess particular myocardial tissue alterations, Table 4.2 summarizes some of the reviewed imaging techniques and their main limitations.

Table 4.2: Use and main limitations of MRI and echocardiography in the characterization of the myocardium.

Modality	Sequence	Description/Usage	Limitations	Ref.
MRI	T1, T2, T2* and MTR	Tissue characterization	Inter-patient analysis requires quantitative mapping.	[148, 149]
	LGE	Short examination times High contrast-to-noise ratio	Requires intravenous contrast agent administration	[148]

	Molecular Imaging	Myocyte apoptosis and necrosis	-	[150, 60]
	Cine	Ventricular function assessment Volume, derived mass and deformation measurements	Segmentation required	[87]
	Tagging	Intramyocardial deformation Ventricular torsion	Limited tag time during cardiac cycle	[151]
	Models and others.	3D structural analysis Biomechanical parameters Post-imaging analysis	Time consuming Requires post-processing calculations	[152, 151, 153, 154]
Echocardiography	Linear M-Mode	Reproducible High frame rates	-	[124]
	Tissue Doppler Imaging	Performed in apical views to acquire mitral velocities Measure both systolic and diastolic function	Not accurate as index of filling pressure in normal subjects	[155]
	3D Echocardiography	Measurement of RV volume parameters	Volume underestimation Lack sensitive analysis tools	[144, 143, 127]
	Contrast Enhanced Echocardiography	Improved visualisation of endocardial border Improved assessment of LV structure and function Clinically recommended	Requires contrast administration	[145, 156]

4.5.2.1 Conventional MRI

Conventional cardiovascular MRI allows the measurement of basic cardiac function parameters, volumes and derived mass calculations in any cardiac axis and with relatively high spatial resolution, although some axis views may be more reproducible and time-efficient measurements [87]. Along with the use of post-processing techniques, conventional MRI may quantitatively measure both global and regional cardiac function (Figure 4.4), however it may not allow measurement of 3D intramyocardial deformation in contrast to Tagging MRI. During the cardiac cycle, the force generated by the myocardium includes two components: passive tension, which resides in the connecting filament protein that tends to restore the sarcomere length when it is

stretched, and active force, the force generated during electromechanical activation-contraction. Active force is generally associated with systolic function while passive force is associated with diastolic function and normally requires prior knowledge of the intra-chamber pressure. The use of basic indices such as the left ventricular ejection fraction, ventricular volumes and mass provides a reasonable indication of the cardiac function and morphological characteristics [148, 87, 46]. But more importantly, there may be a future role for quantitative MRI to document diastolic and interstitial functions of the myocardium [157, 158].

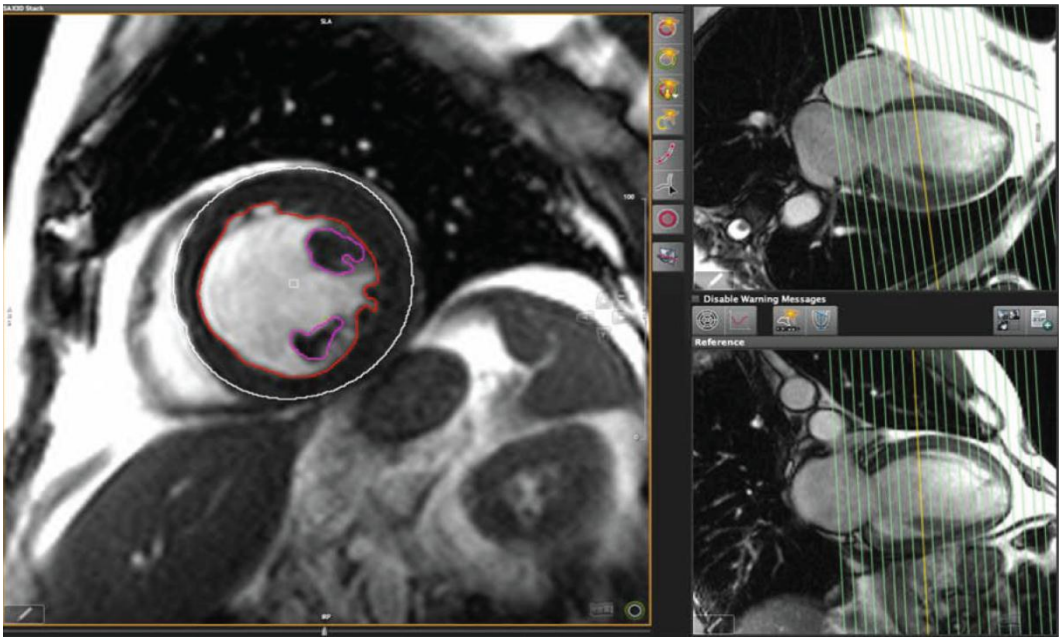

Figure 4.4: Cardiovascular MRI. Short axis analysis (left) using long axis views as a cross-reference (right). [Adapted from Childs et al. (2011)].

4.5.2.2 Tagging, Cine DENSE and Cine MRI

Whereas the heart undergoes complex but predictable motion patterns in the healthy setting, proper characterization of its motion remains an open and challenging research subject. The use of specialized sequences such as Tagging and Cine DENSE imaging will further advance our understanding of the myocardial 3D deformation patterns and facilitate future development of tools and applications that serve that purpose. A tagging-based model was proposed to measure passive diastolic function using a combination of tagging and diffusion tensors MRI with concurrent pressure recordings [151]. Although the model requires considerable acquisition time and a

combination of multiple data acquisition, such models would greatly help quantify myocardial damage severity since the 3D structure of the myofibers is inherently mapped within the myocardium volume. A 3D Cine DENSE sequence with spiral K-space data acquisition was also introduced recently to quantify myocardial strain that encode tissue displacement directly into the image phase [154]. However, the sequence is time consuming and requires previous data segmentation to calculate the Lagrangian displacement field. Recent development in atlas and tools areas provided further the possibility to run statistical analysis using cardiac atlas databases that could play an important role in phenotyping anthracycline-induced myocardial dysfunction [153, 152]. Such models are useful in the presence of cardiomyopathies, especially as it remains unclear how both active and passive myocardial function components are affected by doxorubicin chemotherapy.

Cine MRI may also be used in combination with 2D and 3D models to track myocardial displacements [159-161], which is a starting when evaluating myocardial function and structure. Using the Lagrangian tensor, Bistoquet et al. (2008) proposed an incompressible biventricular model to estimate the 2D Lagrangian strain within the myocardium. A weaker radial and circumferential strain was reported in patient with ventricular dyssynchrony [159]. A 3D model based on short-axis control curves fitted to myocardial walls was proposed [160]. The model seems promising not only in the estimation of myocardial mechanics, but also in providing a personalized reconstruction of diseased hearts with functional alterations. Several other models are proposed with different potentials and limitations, which are discussed in [162, 153, 163, 164]. However, one limit that is common to most Cine-based myocardial models is the inability of the imaging sequence itself to image intramyocardial deformation such as with Tagging MRI. In an ongoing work, the authors used a whole-heart Cine MRI to estimate myocardial 3D deformation using 2D curves tracking and 3D assembly with kriging interpolation (Figure 4.5). Future work will include validation of the resulting deformation data using Tagging MRI as a reference to estimate the model's sensitivity to intramyocardial deformation changes.

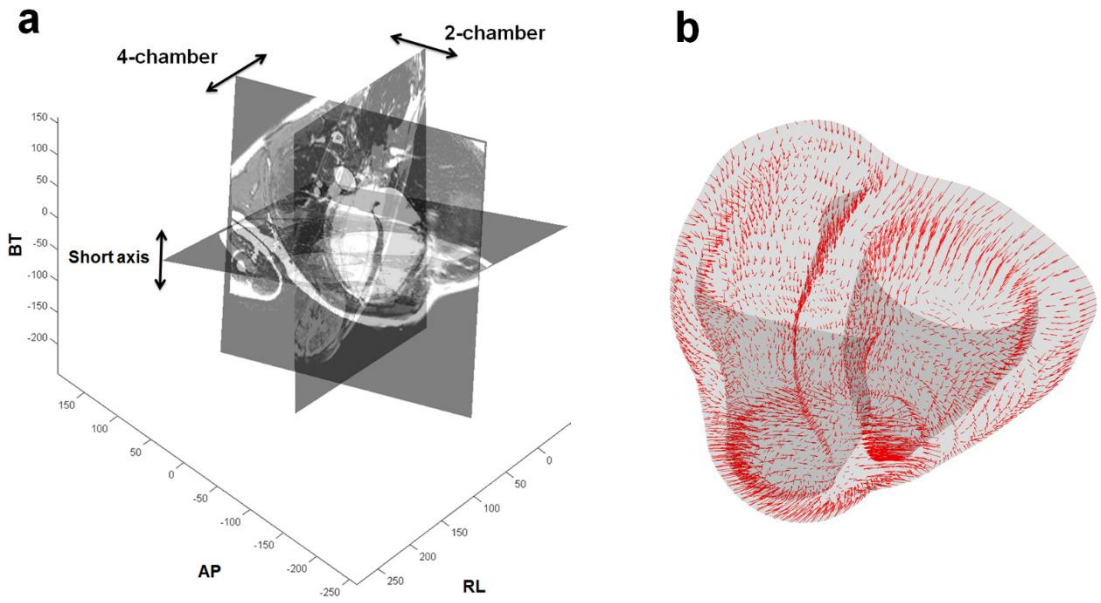

Figure 4.5: Myocardial deformation tracking in a healthy subject. a) MR acquisition configuration. b) Myocardial deformation (interpolated at geometry's nodes) at t = 40ms.

4.5.2.3 Multi-parametric MRI

The use of multiple sequences, each giving a unique contrast for a given tissue, through proton relaxation characteristics, gives MRI the potential to detect a wide-spectrum of abnormalities and pathological tissue changes. Recent development in cardiovascular MRI has made several sequences available clinically. The use of the relaxation times T1, T2, T2* (Figure 4.6) and magnetization transfer ratio (MTR) provide an array of detectable changes capability [52, 148] to characterize myocardial and vascular tissue through characteristics of proton (^{1}H) relaxation and magnetization transfer. T1 mapping with or without late gadolinium enhancement provide a great sensitivity to detect myocardial fibrosis and may be acquired within a single breath hold [165, 166]. In a study including 25 patients with heart failure and 9 transplanted hearts, shorter post-contrast T1 times were reported (383 ± 17 ms in heart failure compared to 543 ± 32 ms in control subjects, $p < 0.0001$) and further correlated with collagen contents at histology ($R = -0.7$). Significant decrease of both pre- and post-contrast T1 times were also reported in both chronic and acute myocardial infarction, with more pronounced changes in acute studies [167, 168]. T2 imaging on the other hand was demonstrated to detect myocardial edema [169], ischemia and other conditions involving changes in the tissue's free water contents [149]. Normal T2 values in the human

myocardium are 52.18 ± 3.4 ms and significant increase in T2 times were reported in patients with myocardial infarction [169]. However, T2 mapping may not be useful to detect cardiac amyloidosis [170]. The use of T2* may also detect early myocardial iron overload [55]. Quantitative T2* imaging was studied in twelve gerbils with iron dextran loading and the results showed a strong linear correlation (R^2 = 0.94) between 1/T2* and cardiac iron [171]. Although, association with anthracycline cardiotoxicity may only be hypothesized at this point, myocardial T2* is a reliable and sensitive sequence for diagnosis and monitoring myocardial iron overload [172]. Magnetization transfer, on the other hand, offers a potential use for tissue characterization and detection of pathologies such as myocardial infarction and inflammation and where myocardial tissue structural integrity is affected. A decrease in MTR was observed in a preliminary study including 7 patients with infarcted myocardium (24.5 ± 9.2% compared to 33.0 ± 3.3%, P = 0.035) [56]. While these sequences may be acquired during a single breath-hold and provide quantitative imaging for inter-patient analysis, their sensitivity in anthracycline cardiomyopathies diagnosis has not been sufficiently investigated. Relationships between the intrinsic passive properties of cardiac [157] and musculoskeletal [158] muscles and MRI parameters were recently reported. It would be interesting to investigate such relations in the setting of anthracycline induced cardiomyopathies.

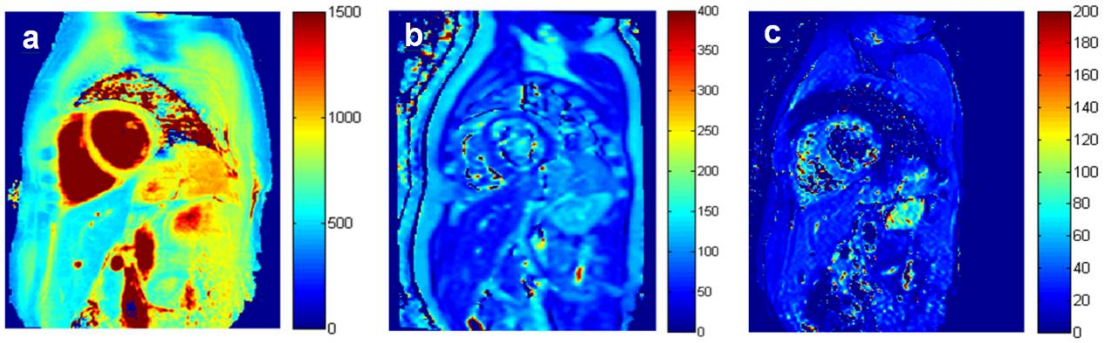

Figure 4.6: Multi-parametric MR mapping in short-axis at the mid-ventricular level in a healthy subject. T1 (a), T2 (b) and T2* (c) relaxation time maps.

Our group has developed a multi-parametric MRI protocol composed of a multiple inversion recovery turbo spin-echo sequence for T1 mapping, a multi-echo turbo spin-echo sequence for T2 mapping, two gradient echo sequences (one with an off-resonance pulse applied at 1100Hz down to the free water proton resonance frequency and the other one without it) for MTR mapping and

a multi-shot spin-echo echo-planar-imaging diffusion-weighted sequence for the apparent diffusion coefficient (ADC) and fractional anisotropy (FA) mapping. Multi-parametric MRI protocol associated to principal component analysis is a promising tool for the indirect evaluation of cardiac muscle mechanical properties and should be useful to find biomarkers and predictive factors of the evolution of the pathologies. Our *in vitro* experiments will now allow us focused *in vivo* testing on healthy and infracted hearts in order to determine useful quantitative MR-based biomarkers. Based on our data it is possible now to perform longitudinal *in vivo* testing on ischemic and revascularized hearts. Future directions of our laboratory aim to better understand and develop novel quantitative MRI parameters as biomarkers of myocardial viability and potential prognostic scoring of myocardial relaxation and contraction.

4.5.2.4 Contrast-enhanced MRI

Molecular imaging of the heart tissue is also feasible by contrast magnetic resonance imaging [173]. It provides great potential for further assessment of other cellular damage induced by necrosis and apoptosis [150, 60]. Contrast enhanced MRI with left ventricular ejection fraction evaluation was used to study 21 patients treated with anthracycline [46]. At day 3 (Figure 4.7) of therapy, delayed contrast enhancement and decreased ejection fraction were detected, where most patients had less than 100 mg/m^2 of anthracycline cumulative dose. Moreover, an increase of >5-fold of contrast enhancement was further associated with a significant loss of ejection fraction of 16% at day 28 of follow-up. The presence of delayed enhancement in 21 of 25 patients with hypertrophic cardiomyopathy was reported [174]. Delayed enhancement was detected in an ill-defined patchy (77.4%) and focal nodular (22.6%) patterns [174]. Delayed enhancement MRI may be particularly useful for assessing myocardial fibrosis [175, 176]. Correlations were found between late gadolinium contrast enhancement MRI and the presence of endocardial fibrosis with mild interstitial myocardial fibrosis seen at histology [177].

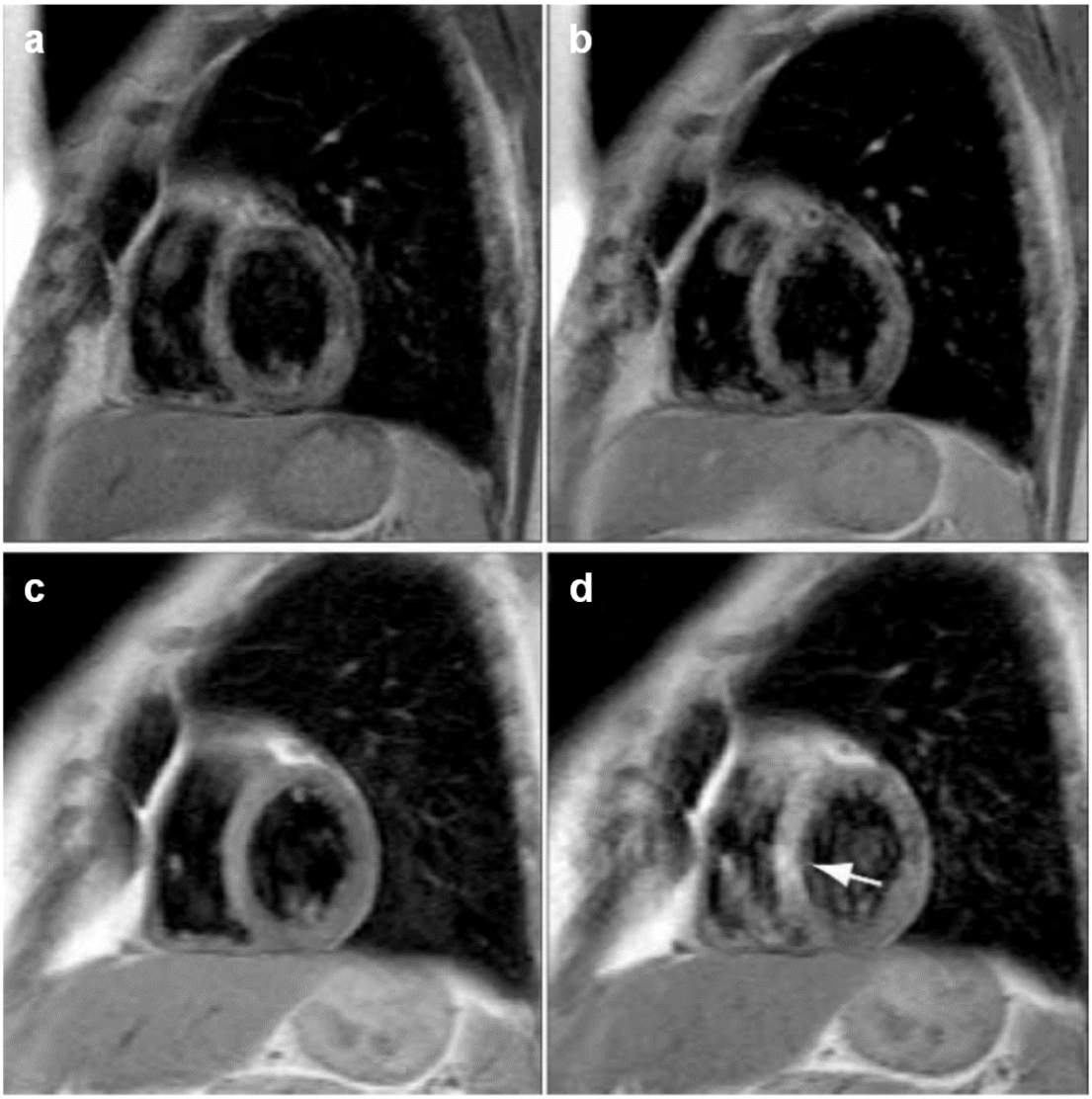

Figure 4.7: T1-weighted before (a and c) and after (b and d) contrast administration. Increased myocardial enhancement at 3 days following anthracycline chemotherapy (c and d) compared to Baseline images (a and b), with a prominent contrast enhancement within the septum (arrow). [Adapted from Wassmuth et al. (2001)].

Manganese-enhanced MRI is also promising in disorders involving calcium homeostasis. Manganese dipyridoxyl-diphosphate (MnDPDP) was recently used in imaging infarcted myocardium [178] and with T1 mapping to quantify Mn^{2+} concentrations and define regions with potentially altered Ca^{2+} homeostasis [179-181]. However, high infused doses may have adverse effects in serial monitoring, although no Mn^{2+} intoxication cases have been reported in patients

with myocardial infarction receiving a single dose of 10 μmol/kg [178]. Assessing the dynamic feature of Mn^{2+} response should provide valuable information related to Ca^{2+} homeostasis in doxorubicin-induced cardiomyopathies. Mn^{2+} follows the same Ca^{2+} influx pathway to reach intracellular space due to its similar chemical properties to Ca^{2+} [181]. Calcium enters the intracellular space via Ca^{2+} voltage-dependant calcium channels and perhaps a much smaller amount via Na^{+}/Ca^{2+} exchanger [182]. Accumulation of the Mn^{2+} in intracellular cell is due to the influx being strong that the efflux which make Mn^{2+} a potential contrast agent in clinical imaging [180].

While many sequences hold an important potential in diagnosing and monitoring cardiomyopathies, some powerful sequences remain however at the research level due to the required long acquisition times, insufficient signal-to-noise or the complex post-processing computations, such as cardiovascular diffusion tensors imaging [59] and MR spectroscopy [183]. The use of MRI may help discriminate the induced pattern of ventricular dysfunction from other pathologies such as stress cardiomyopathy [146].

4.6 Conclusion

A wide-spectrum of functional and morphological anthracycline-induced changes have been described. It is important to recognise the need of imaging tools to identify the etiology of cardiac dysfunction in the setting of chemotherapy treatment. But above all, early detection of myocardial damage and appropriate monitoring of cardiopretective therapeutic strategies need to be enhanced. Although, both MRI and Echocardiography provide several potential ways in assessing anthracycline cardiotoxicity, MRI has the ability to modulate the contrast in response to some specific mechanisms and provide high quality functional information that may target specific cardiotoxic changes. Currently, there are no formal recommendations for the use of cardiovascular magnetic resonance in the setting of dilated cardiomyopathies or other anthracycline-induced cardiotoxicities in clinical practice. Hence, research and development in this direction are necessary.

4.7 Acknowledgments

This work was supported by The Cole Foundation, the Natural Sciences and Engineering Research Council (NSERC) of Canada and the MEDITIS training program (Ecole Polytechnique of Montreal and NSERC).

CHAPTER 5 ARTICLE 2: DETECTION OF DOXORUBICIN-INDUCED CARDIOTOXICITY USING MYOCARDIAL T1 (PRE- AND POST-GADOLINIUM) AND T2 RELAXATION TIMES

Mohamed Aissiou[1,2], Farida Cheriet[2,3], Daniel Curnier[2,4], Tarik Hafyane[5], Maja Krajinovic[2], Caroline Laverdière[2], Daniel Sinnett[2], Gregor Andelfinger[2] and Delphine Périé[1,2]

[1]Mechanical Engineering Department, École Polytechnique de Montréal, Montreal, Canada.

[2]CHU Sainte-Justine Research center, Montreal, Canada.

[3]Computer and Software Engineering Departement, École Polytechnique de Montréal, Montreal, Canada.

[4]Kinesiology Department, University of Montreal, Montreal, Canada.

[5]Montreal Heart Institute, Research center, Montreal, Canada.

5.1 Abstract

Purpose: Doxorubicin-based chemotherapy is effective and widely used to treat leukemia. However, its effectiveness is hampered by a wide spectrum of dose-dependent cardiotoxicity. We aimed to assess the use of T1 and T2 relaxation times as indices of myocardial tissue changes following chemotherapy.

Materials and Methods: We prospectively assessed 26 acute lymphoblastic leukemia (ALL) survivors (25.0 ± 7.7 years old) who previously received doxorubicine-based chemotherapy with MRI acquisitions including pre- and post-gadolinium T1 and T2 sequences. ALL survivors were divided into two groups: high risk (HR, n=18) and standard risk (SR, n=8). Images were acquired at apical, mid-ventricular and basal levels. Partition coefficient, T1 and T2 were compared between ALL survivors and healthy volunteers (HV, n=9).

Results: Partition coefficients were higher in HR or SR group as compared to HV group ($p<0.001$). Pre-gadolinium T1 was higher in HR group compared to SR group ($p<0.01$), higher in SR group compared to HV group ($p<0.005$), and higher in HR group compared to HV group ($p<0.005$). Post-gadolinium T1 was lower in HR group compared to SR group. T2 was significantly higher in HR group compared to SR group ($p<0.001$).

Conclusion: Local myocardial changes were found between high risk and standard risks groups in terms of T1 and T2. The partition coefficient confirmed the presence of an abnormal perfusion function in ALL survivors. The use of T1 and T2 as indices for myocardial tissue damages in the onset of doxorubicin-induced cardiotoxicity should be more investigated.

5.1.1 Keywords

Relaxation times, T1 mapping, T2 mapping, partition coefficient, doxorubicin, cardiotoxicity, chemotherapy.

5.2 Introduction

Several cardiotoxic effects are induced by doxorubicin chemotherapy. Most of them occur during the first 6 months after the last treatment and are progressive [34]. Their amplitude depends mostly on the cumulative dose of doxorubicin, usually measured in milligrams per square meter of body surface area. Some changes occur early while others take several weeks or even months to appear, and may become irreversible despite current treatments [36]. Reported changes include the induction of reactive oxygen species [13], cellular apoptosis [26], diffuse fibrosis [21], premature ventricular contraction [4], extracellular matrix disorganization [103] and other dose-dependent cardiomyopathies that may affect the cardiac function [4]. In adults increased risk of developing late cardiotoxicity is reported and associated with advanced age [8]. Moreover, late cardiac dysfunction may begin with congestive heart failure [8]. However, in children, who could be expected to live many decades after cure of malignancy, impaired myocardial growth, increased left ventricular afterload and possibly a reduction in myocardial contractile function have been reported [41]. Moreover, myocardial abnormalities seem to be highly dependent on the cumulative doxorubicin doses in children [33]. In addition, the contribution of these cardiotoxicities to cardiac dysfunction and myocardial tissue damage in children is not well understood, considering that current clinical indices can only detect late tissue damages [37, 35]. In parallel, the use of cardioprotective agents such as Dexrazoxane is known to reduce the formation of free radicals [184], thus limiting damages to the myocardium.

Current studies on the detection of doxorubicin-induced cardiotoxicity are mainly focussed on MRI and echocardiography, while echocardiography being the most reported as it is inexpensive and the most readily available clinically [185]. Although parameters such as left ventricular ejection

fraction or fractional shortening are conventionally used at a clinical level, these parameters are insensitive biomarkers of early doxorubicin damage [35]. Parameters such as radial and longitudinal strains [35, 186] and MRI-based parameters such as T1 and T2 relaxation times [185] seem to provide a better potential to early detect doxorubicin-induced cardiotoxicity. The use of T1 and T2 relaxation times allows detection of multiple tissue damages [52, 53], based on hydrogen proton spin relaxation in different tissues. Clinical T1 is used to detect the presence of diffuse fibrosis while T2 is used to detect cardiac ischemia [169, 187, 188]. The use of T1 and T2 can also be combined to give insight in terms of water and fat contents in the imaged tissue. The use of T1 and T2 sequences was previously proposed [185, 177, 189-191], with contrast enhanced T1 imaging being one of the most expected to early detect doxorubicin-induced cardiotoxicity [177, 46]. However, one limitation to these studies is that none of them have investigated relaxation time within the whole myocardial area, including the right ventricle.

Contour-based myocardial segmentation, which takes into account the whole myocardial area is more extensive and less prone to segmentation errors. Inclusion of a specific myocardial signal and exclusion of noise is automatically controlled through thresholding rather than manually controlling regions of interest. Manually segmenting regions of interest is prone to segmentation errors and more importantly may not provide full assessment of the signal distribution over of the myocardial tissue. Moreover, using myocardial skeleton curves, standard myocardial segments may also be automatically extracted and analysed. Thus, in this context, the aims of this study were: 1) propose a contour-based estimation of T1 and T2 relaxation times based on the whole myocardial area and 2) evaluate T1 pre- and post-gadolinium enhancement and T2 relaxation times sensitivity to detect myocardial changes induced by doxorubicin-based chemotherapy in childhood ALL survivors.

5.3 Methods

5.3.1 Cohort of survivors

According to the research protocol approved by the institutional Review Board (IRB), we prospectively included 26 ALL survivors from the PETALE study [192] and 9 healthy volunteers (HV) who gave their informed consent. The ALL survivors (mean age: 25.0 ± 7.7 years), 13 males and 13 females, had previously undergone a doxorubicin-based chemotherapy treatment for

childhood leukemia, following the Boston protocol (cumulative doxorubicin doses of 241 ± 97 mg/m^2). These ALL survivors were divided into two groups: high risk (HR, n=18) and standard risk (SR, n=8), based on the cumulative doxorubicin dose received during treatment, age at the beginning of the treatment and other clinical factors. 10 out of 18 HR survivors received dexrazoxane doses of 2749 ± 463 mg/m^2 as a cardioprotective agent. The 9 healthy volunteers (mean age: 48.4 ± 12.4 years), 7 males and 2 females, underwent the same MRI acquisition parameters for pre-gadolinium T1.

5.3.2 MRI acquisition

The MRI acquisitions were performed on a Siemens Skyra 3T MR system using an 18-channel phased array body matrix coil. T1 and T2 images were acquired for each patient during multiple breath-holds and ECG-gated acquisitions. T1 sequence was acquired using a MOLLI sequence for T1 mapping [193] and a T2-prepared TrueFISP sequence for T2 mapping [169]. Post-gadolinium T1 were acquired using Gadovist as a contrast agent at 10-15 min post injection for the ALL survivors. Images were acquired at apical, mid-ventricular and basal levels with a pixel resolution of 1.4x1.4x8.0mm. The overall acquisition time including the 3-plan Localizer scan was approximately 30 minutes.

5.3.3 Myocardial segmentation

Myocardial contours were semi-automatically segmented using an interactive implementation of cubic Bezier curves. In short axis view, three curves were used to segment myocardial area: endocardial left and right ventricular curves and epicardial curve. In a second step, resulting contour curves were re-parameterized and normalized using a percentage length-based discretization of each curve. Myocardial signal was then extracted using a polygon-to-mask algorithm from Matlab functions that converts polygonal contours into myocardial masks. Finally, myocardial skeleton was computed using a Binary-to-skeleton algorithm [194], which was further used to divide the myocardium into 20 segments using a modified version of the standard 17-segment AHA model (Figure 5.1) that include the right ventricle. Segments positions (Figure 5.1) were limited using skeleton junction points and skeleton curve lengths.

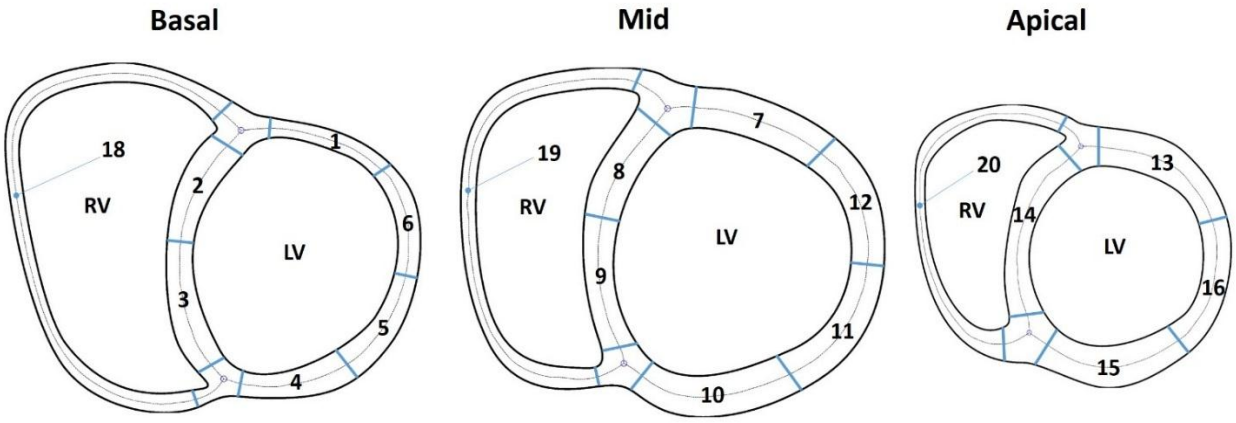

Figure 5.1: Myocardial segmental division in short-axis view. Segment 17 (Cerqueira, 2002), i.e., myocardial apex, was omitted due to excluded long axis views.

5.3.4 Image analysis

Pre- and post-gadolinium T1 along with T2 relaxation times means were evaluated at each segment using respective myocardial contours. The T1 maps were generated using phase sensitive inversion recovery (PSIR) fitting using a three parameter signal model with motion correction [193]. Pixel-wise myocardial T2-maps were generated using unsupervised curve-fitting based on a two-parameter equation with motion correction [169]. Resulting T1 and T2 relaxation times were displayed using a bullseye plot that illustrate T1 and T2 relaxation times mean for each myocardial segment [195]. The threshold used to extract myocardial signal was set at: [950-1400ms] for pre-gadolinium T1, [450-900ms] for post-gadolinium T1 and [30-60ms] for T2 relaxation times, based on our visual analysis of myocardial tissue relatively to adjacent tissues and in order to exclude adjacent tissue's signal. We also evaluated the partition coefficient (λ) [196] of gadolinium as being:

$$\lambda = \frac{\frac{1}{T1_{Post\ M}} - \frac{1}{T1_{Pre\ M}}}{\frac{1}{T1_{Post\ B}} - \frac{1}{T1_{Pre\ B}}} \tag{5.1}$$

Where Post = post-contrast, Pre = pre-contrast, M = myocardium and B = blood. An example of SR and HR maps in short-axis in a standard risk vs. high risk patient is shown in figure 5.2.

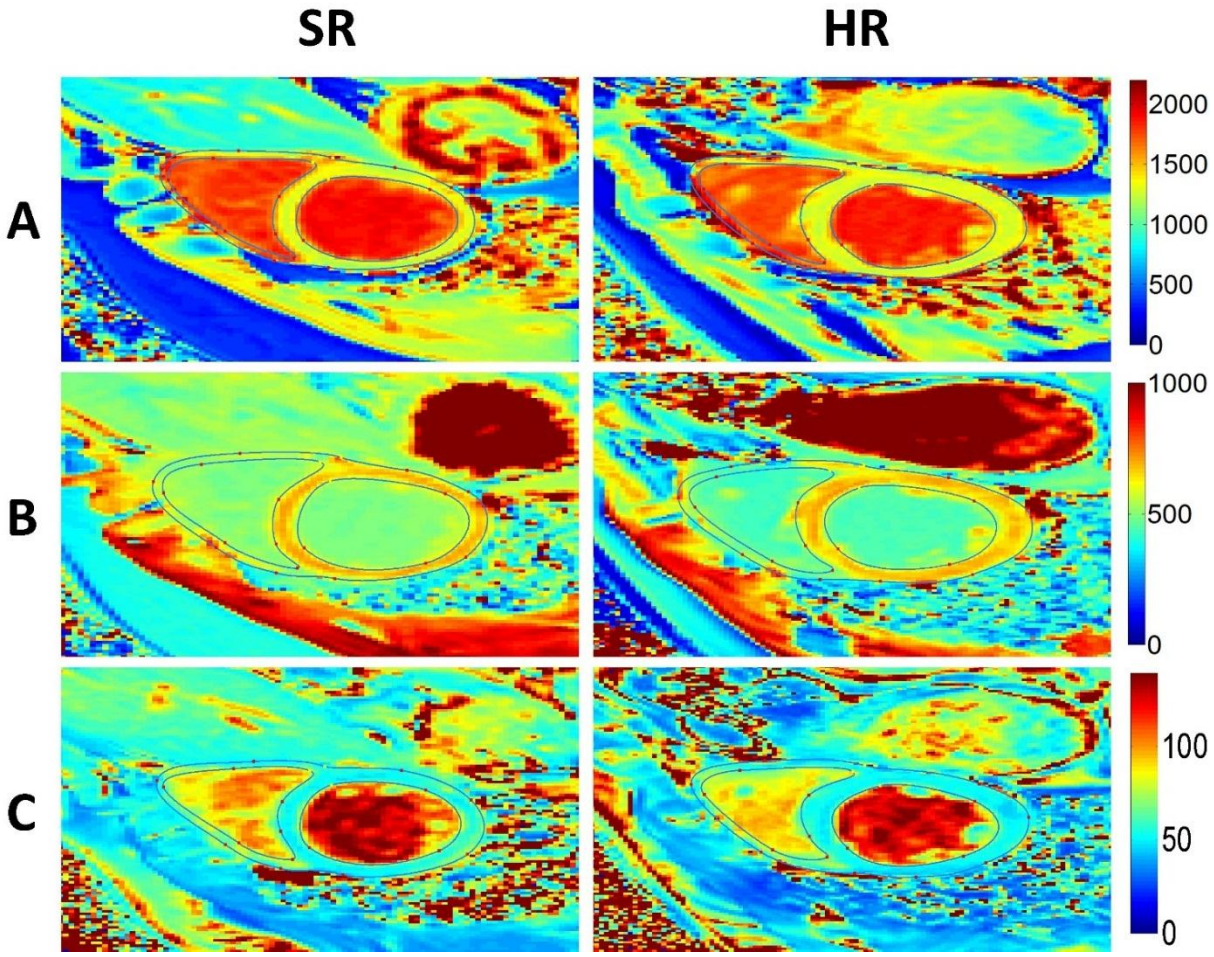

Figure 5.2: Myocardial T1 and T2 mapping at the mid-ventricular level of a standard risk vs. high risk patient. A: pre-gadolinium T1 maps (ms). B: post-gadolinium T1 maps (ms). C: T2 maps (ms).

5.3.5 Statistical analysis

Statistical comparison was done using a 1-way analysis of variance (ANOVA) on the mean relaxation times for each myocardial segment to compare the different groups of volunteers. A 1-way analysis of variance on pixels, i.e., including all pixels for each segment, was also done to compare the different groups. When normality or equal variance tests failed, a 1-way Kruskal-Wallis ANOVA on ranks was done.

Agglomerative hierarchical clustering (AHA) was also performed to verify if the different groups of volunteers (SR, HR and HV) could be retrieved from the MRI relaxation times. Each observation was considered as an initial cluster and the process successively merged clusters into larger clusters until it reached one big cluster containing all the samples. We used the Euclidian distance to determine a pairwise distance metric between each observation. The merging of clusters, or linkage, was based on the calculation of the Ward's distance between clusters. The successive clustering operations produced a binary clustering tree (dendrogram), whose roots contained all the observations.

Linear regressions were performed between T1 or T2 relaxation times and patients' age, weight, height, time between end of treatment and MRI acquisition and received doxorubicin dose.

All statistics were done using Microsoft Excel 2016 (Microsoft Corp, Redmond, WA, USA), except for the ANOVA that was done using SigmaPlot 12.0 (Systat Software Inc., San Jose, CA, USA) and the clustering which was done using XLSTATS software (Addinsoft, New York, USA).

5.4 Results

5.4.1 Bullseye analysis of mean T1 and T2 relaxation times

Small differences can be seen in pre-gadolinium T1 between SR and HR groups or between HR and healthy volunteers, especially near myocardial free wall (Figure 5.3). Post-gadolinium T1 was lower in the HR group compared to the SR group. Partition coefficient of gadolinium was higher in the SR and HR groups compared to the healthy volunteers group ($p<0.001$). These differences were distributed over the whole myocardial area rather than within specific myocardial segments. The same tendency was seen for T2. HR group had higher T2 as compared to SR group with segment 4 being the most affected by the differences.

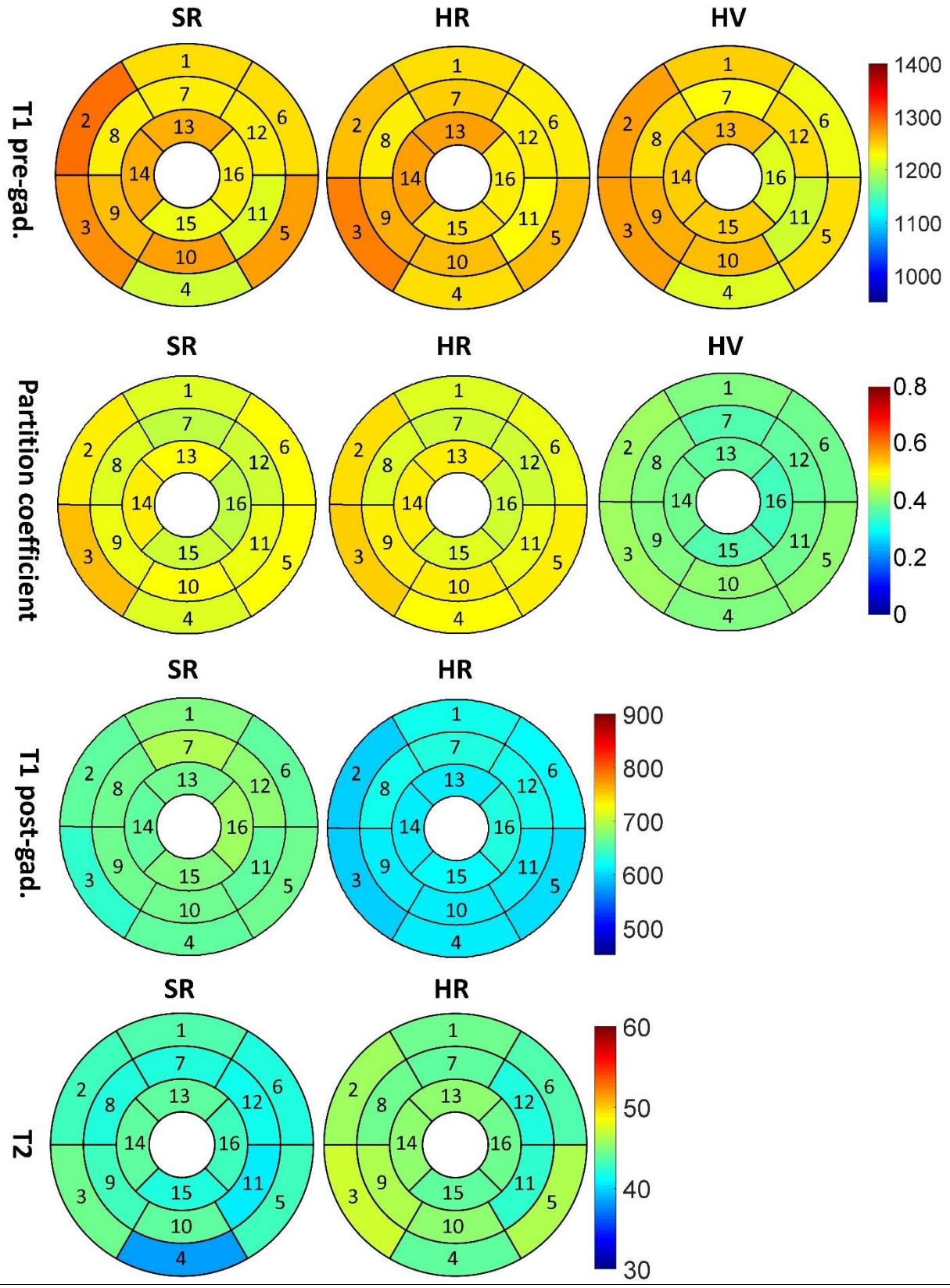
SR
HR
HV
T1 pre-gad.
1400
1300
1200
1100
1000
Partition coefficient
0.8
0.6
0.4
0.2
0
T1 post-gad.
900
800
700
600
500
T2
60
50
40
30

Figure 5.3: Myocardial segmental T1 and T2 relaxation times in ALL survivors (SR and HR groups) and healthy volunteers (HV).

5.4.2 ANOVAs between HR, SR and HV

Partition coefficient mean was 0.48 ± 0.01, 0.49 ± 0.01 and 0.38 ± 0.01 for SR, HR and HV respectively. Partition coefficient was significantly elevated in HR group compared to HV group ($p<0.001$) and in SR group compared to HV group ($p<0.001$). However, there were no significant differences between SR and HR groups ($p=0.42$). Furthermore, we found that 19 and 19 out of 19 segments presented higher partition coefficient in HR and SR groups compared to HV group, respectively. Though, there were no differences between SR group and HR group when comparing them segment by segment.

On the mean values per segment, pre-gadolinium T1 showed no significant differences between SR, HR and HV groups ($p = 0.69$). However, post-gadolinium T1 was significantly lower in the HR group compared to SR group. This finding was seen in 18 out of 19 myocardial segments. On the other hand, T2 relaxation times were significantly higher in HR group compared to SR group in 4 out of 19 segments, predominantly at apical level. Segment 8 ($p=0.04$), segment 14 ($p=0.04$), segment 15 ($p=0.002$) and segment 16 ($p=0.048$) were the most affected by these differences.

On the pixels' data, pre-gadolinium T1 was significantly lower in SR group in 8 out of 19 segments compared to HR group ($p < 0.01$). 5 out of 19 segments were significantly higher in SR group compared to HV group ($p < 0.005$) and 7 out of 19 segments were significantly higher in HR group compared to HV group ($p < 0.005$). Post-gadolinium T1 relaxation times were significantly lower in HR group compared to SR group in all myocardial segments ($p < 0.001$). T2 relaxation times were significantly higher in the HR group compared to the SR group in all myocardial segments ($p < 0.001$).

Within the high risk group, patients who received dexrazoxane had slightly higher but not significant post-gadolinium T1 relaxation times compared to patients who did not receive dexrazoxane in their treatment (627 ± 47 ms vs. 589 ± 30 ms, $p=0.06$). However, both pre-gadolinium T1 and T2 relaxation times were similar between the patients who received dexrazoxane and the patients who did not receive dexrazoxane (1253 ± 29 ms vs. 1246 ± 17 ms,

p=0.51 and 45 ± 3 ms vs. 44 ± 2 ms, p=0.55, respectively). Based on doxorubicin doses alone (<250 mg/m^2 vs. >250 mg/m^2), both T1 and T2 relaxation times failed to detect significant differences.

Segmental division of the myocardium revealed significant differences in pre- and post-gadolinium T1 between male and female patients. Within the left ventricle, pre-gadolinium T1 was significantly lower in male patients compared to female patients (1238 ± 20 ms vs. 1260 ± 18 ms, p=0.003) while post-gadolinium T1 was significantly higher in male patients compared to female patients (648 ± 55 ms vs. 606 ± 39 ms, p=0.02). Significant differences between the two genders were seen in 7 out of 19 segments for pre-gadolinium T1 and 16 out of 19 segments for post-gadolinium T1. T2 relaxation times though, remained similar between the two groups (44 ± 3 ms vs. 44 ± 2 ms, p=0.74).

5.4.3 Agglomerative hierarchical clustering analysis

Agglomerative hierarchical clustering on the different groups of volunteers showed three main distinct clusters (Figure 5.4). For pre-gadolinium T1, the 3 clusters contained mixed data from the 3 groups. However post-gadolinium T1 showed that the data from the HR and SR groups were included in 3 different clusters respectively. Segments 1, 3, 6, 8, 11, 14-16 were the most susceptible to dissociate each group in a separated cluster. For T2, the first cluster contained most of SR patients with an accuracy of 0.6 and a Matthews correlation coefficient (MCC) of 0.3. Segments 8 and 15 were the most susceptible to dissociate SR group in a separated cluster. A further analysis of the clusters on pre- and post-gadolinium T1 showed that the data of the HR patients who received dexrazoxane were included in a different cluster than the data of the HR patients who did not receive dexrazoxane in their treatment.

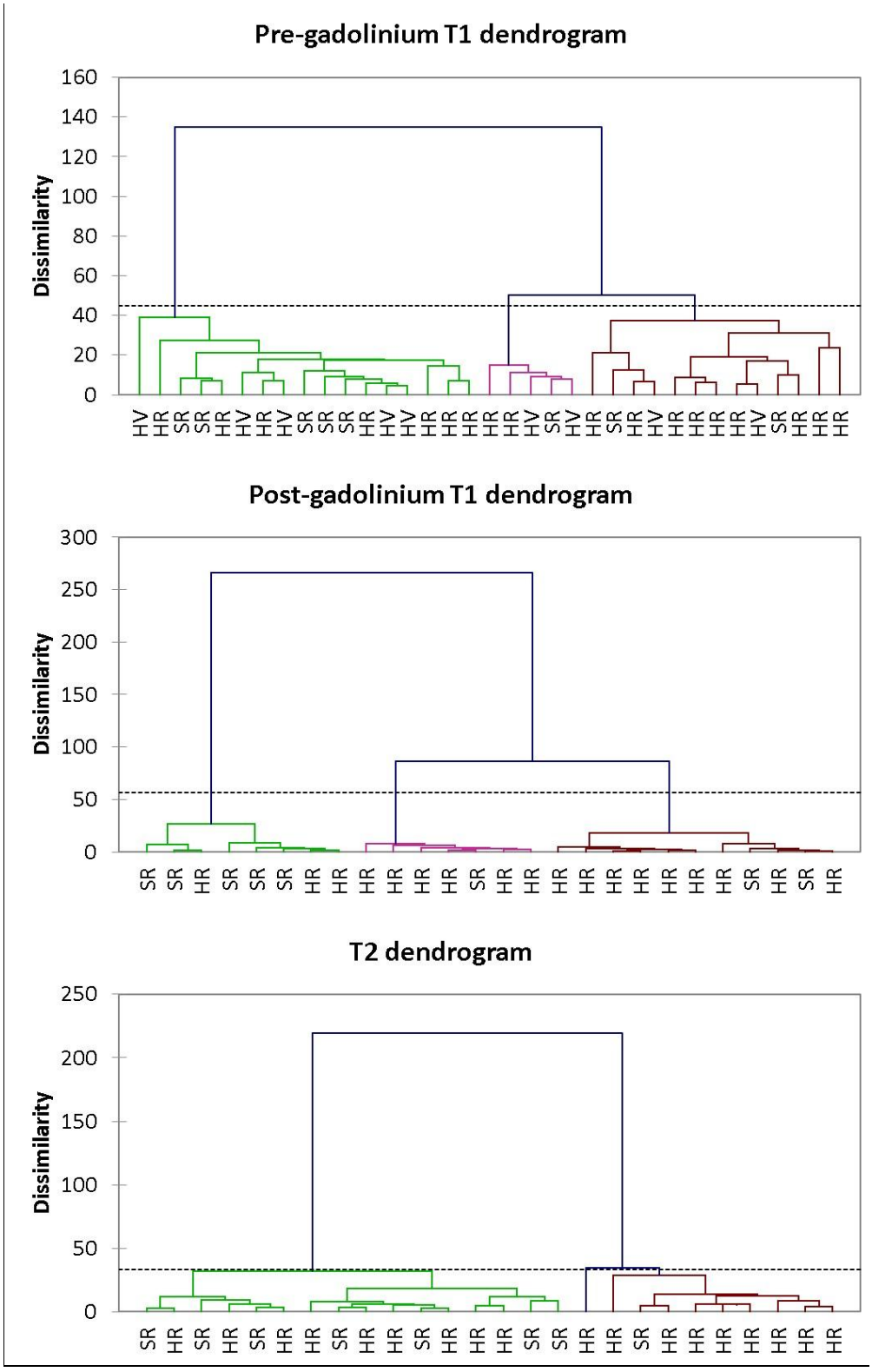

Figure 5.4: Hierarchical clustering analysis of T1 and T2 relaxation times. Legend: SR: standard risk group, HR: high risk group, HV: healthy volunteers group.

5.4.4 Linear regressions

Linear regressions between relaxation times and patients' age, weight, height, time between end of treatment and MRI acquisition and received doxorubicin dose showed no significant relationships. R-squared coefficients were equal or less than 0.25.

5.5 Discussion

The first aim of this study was to propose a contour-based estimation of T1 and T2 relaxation times based on the whole myocardial area. A robust method using skeleton-based segmentation was developed. Its advantages over the existing methods are that it allows both global and local analysis of the myocardium. Segmental division of the myocardium is completely automated and myocardial analysis is done in a very fast and simplified manner. The second aim was to evaluate T1 pre- and post-gadolinium enhancement and T2 relaxation times sensitivity to detect myocardial changes induced by doxorubicin-based chemotherapy in childhood ALL survivors. Local myocardial differences were found in pre-gadolinium T1 between SR and HR group and between ALL survivors and healthy volunteers. These differences were further amplified by post-gadolinium enhancement when comparing SR group to HR group. Partition coefficient of gadolinium confirmed the presence of a subnormal perfusion function in ALL survivors. T2 was slightly higher in the high risk group than in the standard risk group. Moreover, agglomerative hierarchical clustering revealed clear distinction between high risk and standard risk ALL survivors when comparing their respective post-gadolinium T1.

Our contour-based technique may better estimate relaxation times compared to methods based on regions of interests (ROIs) as it takes the whole myocardial area into account. Automatic segmental division of the myocardium often requires the exclusion of the right ventricle [191]. However, our technique includes both the left and right ventricle as myocardial skeleton is automatically extracted from endocardial and epicardial contour curves of the whole myocardium, and used to subdivide the myocardium into segments, including the right ventricle.

Relaxation times at 3T in ALL survivors (base: 1247/44ms, middle: 1243/44ms, apex: 1261/45ms) were respectively slightly higher for T1 pre-gadolinium and similar for T2 relaxation times as compared with reported data in the literature [197] (base: 1157/44ms, middle: 1159/45ms, apex:

1181/47ms). However, our values of relaxation times are superior as they are obtained automatically and evaluated in each myocardial segment using the standard AHA segment model.

The fact that ALL survivors, especially the HR group, had slightly higher pre-gadolinium T1 relaxation times compared to healthy volunteers may suggest reduced systolic function [198], oedema or protein deposition, but not lipid or iron deposition (associated to low T1 values) [199]. It is known that a decrease in post-gadolinium T1 relaxation times is related to myocardial diffuse fibrosis [166, 165] or fibrosis scar [200, 201] due to the retention of gadolinium contrast in fibrotic tissue that causes T1 shortening. In our cohort of ALL survivors, post-gadolinium T1 relaxation times were significantly lower in HR group compared to SR group in 18 out of 19 myocardial segments. On the other hand, partition coefficient, which was significantly elevated in ALL survivors compared to healthy volunteers may suggest the presence of a reduced perfusion function. It was shown before that in acutely infarcted myocardium, gadolinium had a higher partition coefficient [196]. The partition coefficient of gadolinium determines the fibrosis index [202]. The constant T2 between groups suggested no infarcted myocardium [169], no acute ischaemic or non-ischaemic injury due to associated changes in myocardial free water content [203-209].

Agglomerative hierarchical clustering revealed clear distinction between the different groups of volunteers when comparing their respective post-gadolinium T1. Some segments were more susceptible to distinguish the different groups from each other, particularly near the apical region of the heart. Clustering is a powerful technique to show the sensitivity of a parameter by separating potential groups based on this parameter. In our study, the inclusion of dexrazoxane in the treatment affected the clustering of the HR group, suggesting that combined doxorubicine and dexrazoxane treatment induce different cardiac changes than doxorubicine alone. Dexrazoxane act as a cardioprotective agent by reducing free radicals formation and is associated with significant reduction in the incidence of myocardial injury due to doxorubicin [210, 121]. In a study comparing the effect of doxorubicin alone and doxorubicin with dexrazoxane, it has been shown that dexrazoxane has the ability to reduce free radicals formation which reduces cardiomyocyte death but also the reduction of myocardial stress and inflammation [211].

In our cohort of ALL survivors, we believe that the use of dexrazoxane in their treatment may have significantly inhibited the apparition of further doxorubicin-induced cardiotoxicitiy.

The absence of differences on the relaxation times between patients who received a doxorubicine dose <250mg/m^2 and patients who received a doxorubicine dose >250mg/m^2 might be explained by overall moderate doxorubicin doses ranging between 59mg/m^2 and 334mg/m^2. The risk factor which takes into account the cumulative doxorubicin dose received during treatment, age at the beginning of the treatment and other clinical factors may be a better parameter than doxorubicin dose alone in distinguishing the severity of doxorubicin-induced cardiotoxicity, especially as it is multivariate and include the several factors that are reported to have significant risk to increase cardiotoxicity [212].

The result that female patients had higher pre-gadolinium T1 than male patients while post-gadolinium T1 was lower in female patients compared to male patients is in agreement with previously reported findings [191, 213, 214]. Based on these findings, the fact that 7 out of the 9 healthy volunteers included in this study were males may have pushed their pre-gadolinium T1 lower while post-gadolinium T1 higher.

The following limitations were encountered during this study. Both wall and segmental division of the myocardium were completely automated, however due to geometrical variations, images had to be normalized in terms of orientation and rotation in order to allow automation. Moreover, skeleton curves had to be slightly smoothed using kriging interpolator [215] due to pixelation effects when extracting such curves from a binary mask. Computation took less than a second to process each image, nevertheless it is important to mention that segmentation phase took an average of 3 minutes per patient, which include 3 short-axis images.

Depending on adjacent tissue's signal, contour-based estimation of T1 and T2 may overestimate or underestimate relaxation times within a given myocardial segment as it includes the whole myocardial wall. Some neighboring pixels may be unwantedly included while some myocardial pixels may be unwantedly excluded when extracting myocardial masks. However, with a comprehensive threshold this phenomenon of inclusion of noise pixels and exclusion of good pixels may be reduced to a negligible level. Right ventricular area was also assessed in this study. However, difficulties were encountered when delineating right ventricular walls as it is thinner than other regions and myocardial T1 relaxation times gets more difficult to distinguish from signal of the blood and adjacent tissues. Thus, right ventricular wall might be more prone to noise inclusion

and segmentation errors than septal or left ventricular walls. Both T1 and T2 maps were mostly noise-free within left ventricular and septal areas. Some T2 images had slight noise predominantly within the right ventricular area. To limit noise and adjacent tissue inclusion, we applied a comprehensive threshold. Lastly, we did not present post-gadolinium T1 comparison between the different groups because our cohort of ALL survivors received Gadovist as a contrast agent, whereas our healthy volunteers received MultiHance as a contrast agent. For this reason, we choose the partition coefficient, which should be insensitive to contrast agents variation, but also post contrast acquisition time.

5.6 Conclusion

Local myocardial changes were found between high risk and standard risk groups in terms of T2 and pre- and post-gadolinium T1 relaxation times. The partition coefficient confirmed the presence of an abnormal perfusion function in ALL survivors. The use of T1 and T2 relaxation times, particularly the partition coefficient, as early indices for myocardial tissue damages in the onset of doxorubicin-induced cardiotoxicity should be investigated with a larger cohort of cancer survivors to further assess its clinical value.

Acknowledgment

This work was financially supported by the Cole Foundation, the NSERC (Discovery grant and CREATE-MEDITIS Program), the FRQNT (team grant) and the CIHR (team grant).

CHAPTER 6 ARTICLE 3: MYOCARDIAL DISPLACEMENT ANALYSIS USING CARDIOVASCULAR CINE-MRI IN DOXORUBICIN-TREATED ACUTE LYMPHOBLASTIC LEUKEMIA SURVIVORS

Mohamed Aissiou[1,2], Farida Cheriet[2,3], Daniel Curnier[2,4], Matthias G. Friedrich[6], Tarik Hafyane[5], Maja Krajinovic[2], Caroline Laverdière[2], Daniel Sinnett[2], Gregor Andelfinger[2] and Delphine Périé[1,2]

[1]Mechanical Engineering Department, École Polytechnique de Montréal, Montreal, Canada.

[2]CHU Sainte-Justine Research center, Montreal, Canada.

[3]Computer and Software Engineering Departement, École Polytechnique de Montréal, Montreal, Canada.

[4]Kinesiology Department, University of Montreal, Montreal, Canada.

[5]Montreal Heart Institute, Research center, Montreal, Canada.

[6]McGill University, Montreal, Canada.

6.1 Abstract

Background: Displacement patterns analysis of the myocardium allows direct quantification of ventricular function, both locally and globally. In the presence of myocardial damage such as dilated cardiomyopathy, the architecture of myocardial fibers becomes abnormally stressed and resulting patterns of displacement change. Currently, very few techniques are available for tracking myocardial displacement and most of them look into ventricular function rather than displacement patterns. In this context, the aim of the current study was to estimate the effect of doxorubicin exposure during treatment for acute lymphoblastic leukemia (ALL) on 2D myocardial displacement patterns using cine-CMR.

Methods: Twenty-six ALL survivors who were previously exposed to Doxorubicin and 6 healthy volunteers were prospectively included in this study. Cine images were acquired using an ECG-gated cine sequence in 2-chamber, 4-chamber and short-axis views using 25 phases per cardiac cycle. In a first step, the myocardium was segmented using a custom-written MatLab program

where myocardial contours were extracted and parameterized using per-length normalization. In a second step, the myocardial skeleton was extracted and tracked during each phase. Finally, myocardial displacement along with functional indices were estimated and compared between ALL survivors and healthy volunteers.

Results: Patterns of displacement were similar between ALL survivors and healthy volunteers. However, cumulated displacements through systolic contraction were significantly reduced in cancer survivors compared to healthy volunteers ($p<0.001$). Moreover, these differences were further amplified through the rest of the cardiac cycle. Healthy volunteers had more area and length changes compared to cancer survivors ($p<0.001$), especially during systolic contraction. Likewise, wall thickness evolution through the cardiac cycle was lesser in ALL survivors compared to healthy volunteers ($p<0.001$). Thickening fraction remained similar between ALL survivors and healthy volunteers in all planes. Ejection fraction was significantly reduced in ALL survivors compared to healthy volunteers ($p<0.001$) when estimating it using 2-chambers and 4-chambers view. While most of ALL survivors had a stable clockwise and counter-clockwise twist, the overall normalized rotation was slightly desynchronized with the cardiac cycle, and less than in healthy volunteers ($p=0.02$).

Conclusion: Skeleton-based myocardial analysis provides new insights on local and global myocardial displacement patterns. The technique is less sensitive to tracking errors as resulting skeleton displacements are more stable than contour-based displacements and most importantly make the analysis of ventricular function easier. Displacement is significantly reduced in cancer survivors compared to healthy subjects, although the signature of displacement curves remains similar. Skeleton-based myocardial tracking may pave the way for three-dimensional tracking of the myocardium.

6.1.1 Keywords

Cardiovascular cine-MRI, myocardial tracking, myocardial displacement patterns, doxorubicin-induced cardiotoxicity, chemotherapy

6.2 Background

Doxorubicin chemotherapy is effective and widely used to treat acute lymphoblastic leukemia. However, its effectiveness is hindered by a wide spectrum of dose-dependent cardiotoxicity, including both morphological and functional changes affecting the myocardium. These changes include reduced left ventricular (LV) fractional shortening [121], ventricular dilatation [4], myocardial wall thinning [7], reduced ventricular contractile function along with radial strain decrease [4, 35]. Most of doxorubicin-induced myocardial damage is dose-dependant and may be progressive over time [121, 216], particularly in children who seem more susceptible to the cardiotoxic effects of doxorubicin [31]. Thus the need to detect myocardial damage early is crucial, especially in children where delayed cardiotoxicity may manifest years or decades later [79, 217].

Myocardial displacement patterns allow direct quantification of the cardiac function both locally and globally [218]. These displacement patterns are often investigated by using Doppler tissue imaging or echocardiographic speckle tracking [35, 219, 220]. In the presence of myocardial damage such as dilated cardiomyopathy, the architecture of myocardial fibers undergoes abnormal stress and displacement patterns change. In healthy hearts, these patterns provide a unique signature describing the resulting myocardial displacements seen on images [221]. Furthermore, tracking myocardial displacements is a challenging task since myocardial tissue displacement is three dimensional and geometrically inhomogeneous. Moreover, the accuracy of many advanced post-processing analysis techniques such as Doppler- or speckle-derived displacements relies mainly on accurate myocardial tracking.

Currently, very few techniques are available for tracking myocardial displacements in a closed-loop cardiac cycle to assess functional abnormalities. Several MRI sequences and models were proposed to track myocardial displacements including the use of phase-based strain imaging sequences such as HARP [222] and cine DENSE [223-225, 154, 226], tagging-based sequences [227] and others [228, 229, 63, 65]. While most of these techniques are limited by noise and spatial resolution, the main limiting factors remain long acquisition times, reduced accuracy in estimating displacements and most importantly segmentation stage which is most of the time error prone.

Contour-based models using cine CMR images have the potential to accurately extract myocardial displacements during the whole cardiac cycle [230-232], especially since cine MRI provides high quality cardiovascular images. Traditionally, myocardial displacements are obtained from

contours, segmented automatically or semi-automatically [233], either with or without anatomical reference points [234, 235]. Automated segmentation techniques include the deformable registration method, where the segmentation is based on an inverse consistent deformable registration approach [236]. Another fully automated segmentation technique includes the layered spatio-temporal forests algorithm, where the tracking is based on automatic machine learning to extract myocardial contours [237]. Semi-automated techniques include the contour-constrained optical flow tracking, where an optical flow algorithm is used to track, through the whole cardiac cycle, an initial contour manually drawn [238]. This technique is similar to the elastic registration technique, where the myocardial deformation field is parametrized using smooth basis functions, often B-splines in image processing, and used to track myocardial contours [239]. Another semi-automated technique include the block matching algorithm, where epicardial and endocardial contours are initially drawn on the first timeframe and subsequently tracked by using the blockmatching technique [240, 241]. Finally, another algorithm worth mentioning is the manually guide-point modeling, where a small number of guide points are placed interactively on a sparse subset of slices and frame and tracked through the whole cardiac cycle [242].

In general, only a few methods exploit the information provided by cardiac motion, partly because of the complexity and the variability of the motion model, but also because end-diastolic and end-systolic images are sufficient for estimating the cardiac function at a clinical level [232]. The use of 3D models, reconstructed from cardiovascular images, to track myocardial displacements in an automated manner is also worth mentioning [63, 243, 159]. The use of 3D modeling has the advantage of providing complex and sophisticated information in terms of myocardial motion. However, these models are often time consuming and error prone when it comes to 3D reconstruction and simulation [244]. In this context, the aim of the current study was to estimate the effect of doxorubicin exposure during treatment for acute lymphoblastic leukemia (ALL) on 2D myocardial displacement patterns using cine-CMR. We hypothesized that 2D displacement patterns within the middle slice of the myocardium can be accurately estimated from contour tracking and allow the detection cardiotoxic myocardial damage.

6.3 Method

6.3.1 Cohort of survivors

The present study is part of the PETALE project which is an ongoing prospective study being conducted at the Sainte-Justine University Hospital Center (UHC) in Montreal, Canada. The PETALE project addresses late chronic side effects in a cohort of Acute Lymphoblastic Leukemia survivors (QcALL) [192]. The main objective of PETALE is to identify genetic and biological biomarkers predicting long-term treatment-related health problems developments. Patients were recruited from the QcALL cohort after the study was approved by the institutional Review Board (IRB). We prospectively included 26 ALL survivors which have previously been exposed to Doxorubicin as a part of their chemotherapy protocol and 6 healthy volunteers. Within the ALL survivor group, eight (n=8) were included in the standard risk (SR) group and eighteen (n=18) were included in the high risk (HR) group, based on a risk index related to the severity of the pathology, cumulative doxorubicin dose and volunteer's age [245, 246]. Median cumulative dose of Doxorubicin was 60.5 mg/m^2 for SR and 286 mg/m^2 for HR. 10 patients also received Dexraxozane as a cardioprotective agent. 13 survivors were male and 13 were females with an average at-acquisition weight and height of 1.66 ± 0.13m and 71.3 ± 13.8kg, respectively. Median age at ALL diagnosis was 24.1 ± 9.0 years. MRI scans were performed 13.6 ± 7.3 years after treatment.

6.3.2 Cine-CMR acquisition

Cine-CMR were acquired using a standard, ECG-gated cine sequence (Steady State Free Precession/SSFP) on a clinical 3T MRI system (Skyra™, Siemens Healthcare, Erlangen, Germany) and an 18-channel phased array body matrix coil. Acquisition parameters were: Slice thickness 8mm, repetition time 34.6ms, effective echo time 1.2ms, flip angle 38°, iPAT factor 3, matrix 208×210 and in-plane pixel size 1.25×1.25mm. Approximately 14 slices were acquired in a short axis view and 2 slices in a long axis view (2-chamber and 4-chamber). For each slice, 25 phases of the cardiac cycle were acquired during multiple breath-holds. The overall acquisition time including the 3-plane localizer scan was approximately 15 minutes.

6.3.3 Myocardial segmentation and displacement tracking

Myocardial contours were semi-automatically segmented from the cine-CMR images (Figure 6.1) using an interactive implementation of cubic Bezier curves. We segmented one slice in 2-chamber, one slice in 4-chamber and one slice in short-axis view at the mid ventricular level. Once the first phase was segmented, at each of the following phases, a contour template based on the previous phase was proposed where the user needed only to correct contours relatively to the previous phase to limit intra-user errors. Resulting curves were re-parameterized using "cumulative percentage length" discretization and smoothed using geometrical kriging [215]. Myocardial displacements were also slightly smoothed temporarily to refine myocardial displacements through the cardiac cycle, but without altering the accuracy of segmentation. Furthermore, myocardial displacements were estimated using a skeleton-based approach. From a binary myocardial mask, a skeleton algorithm [194] was used to extract skeleton curves along with ending and junction points. Finally, skeleton curves along with end- and junction-points were further processed to compute perpendicular projections into myocardial contours (Figure 6.1-C).

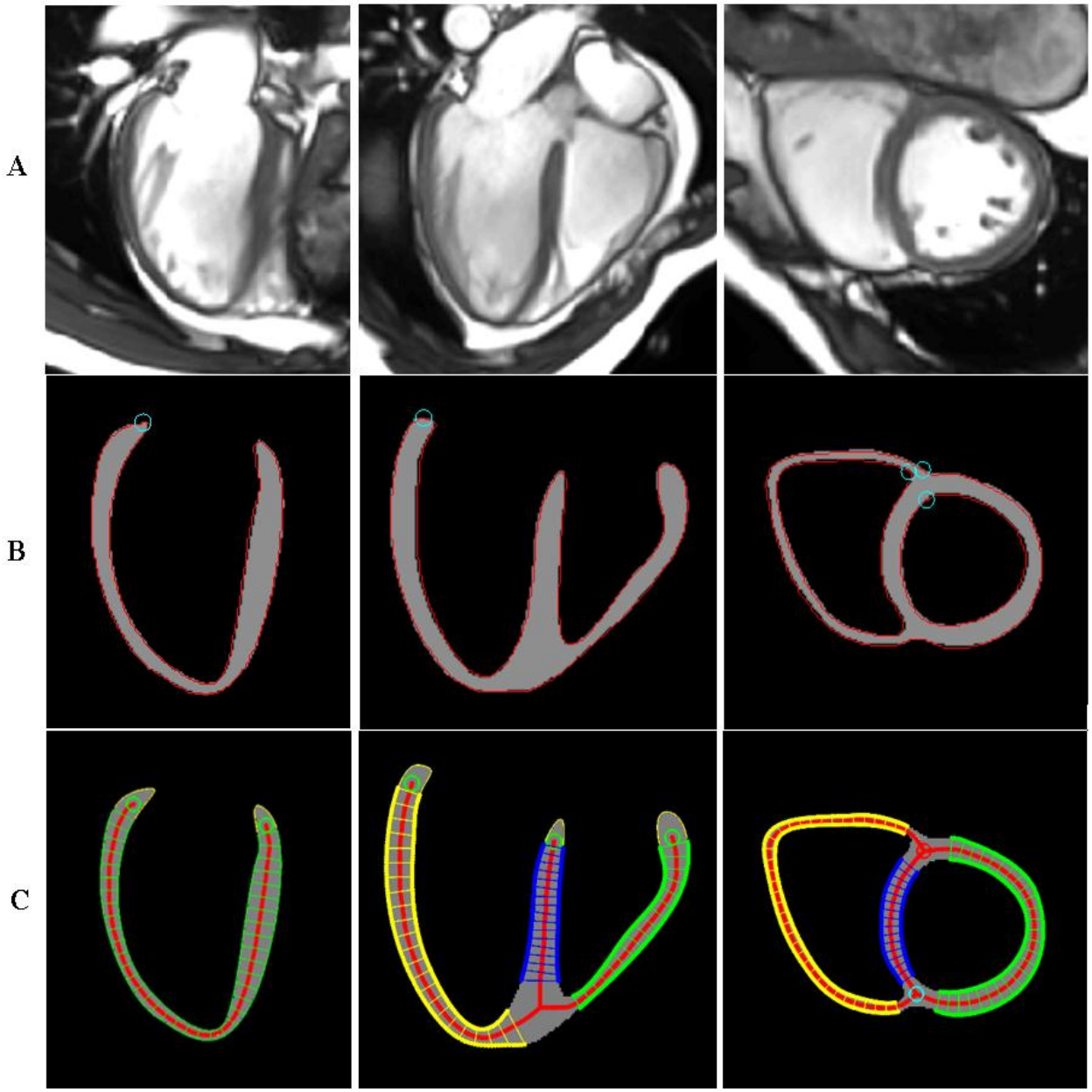

Figure 6.1: Cine-CMR images in 2-chamber (left), 4-chamber (middle) and short-axis (right) views (A) and the resulting segmentations: contour-based (B) and skeleton-based (C).

6.3.4 Contours extraction repeatability study

For the inter-observator repeatability study, 5 experimented operators segmented myocardial contours on same 2-chamber, 4-chamber and short-axis cine-CMR images of the heart. The following workflow was implemented: 1) Segmentation of myocardial contours through the

creation of a closed Bezier curve, 2) excluding the papillary muscle, 3) Exclusion of atrial structures and 4) Other technical software-related tasks such as location and direction of contour initiation.

For the intra-observator repeatability study, the same cine image was evaluated in a blinded fashion 10 times by the same operator and using the same workflow.

Once contours were obtained, the repeatability was evaluated using a standard deviation-based estimation model (Equation 6.1).

$$repeatability\ (\%) \approx 100 - \frac{100\ x\ Standard\_deviation(index)}{mean(index)} \tag{6.1}$$

Where $index$ represents either the resulting area or thickness estimation from one segmentation to another.

6.3.5 Displacements patterns analysis

Myocardial displacement curves were obtained as follow: Once myocardial contours were calibrated using perpendicular projections of skeleton curves, contours were unfolded into 1D and parametrized (Figure 6.2) using the percentage of cumulative length. From the first phase of the cardiac cycle and at each of the following phases, absolute displacement at each point along myocardial contours was added cumulatively. Resulting unfolded 1D displacements were evaluated at three times of the cardiac cycle: at the end of systole (1-TS), at the beginning of early diastole (1-TDP) and at the end of the cardiac cycle (1-END), which takes into account the total absolute displacement during the whole cardiac cycle. An example of myocardial displacement paths is shown in figure 6.3.

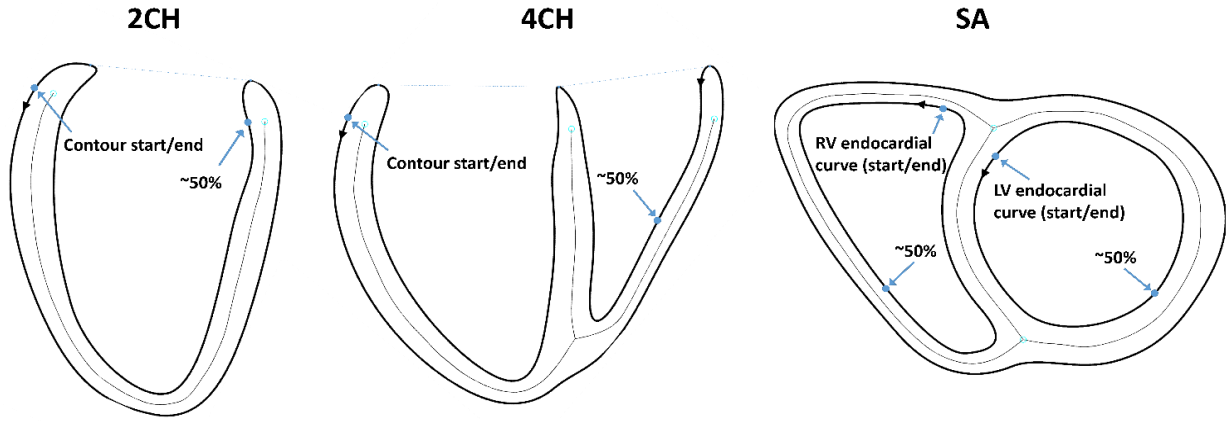

Figure 6.2: Myocardial skeleton-based characteristics in 2-chamber, 4-chamber and short-axis views. The starting point, middle point (50% of the curve) and the end point of the myocardial contours are shown.

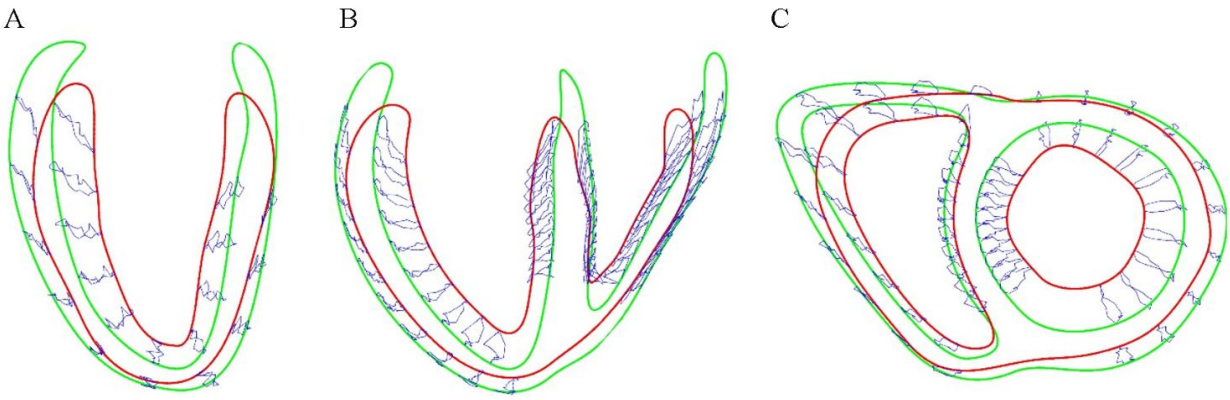

Figure 6.3: Myocardial displacement paths in 2-chamber (A), 4-chamber (B) and short-axis (C) views.

6.3.6 Myocardial characteristics during the cardiac cycle

Normalized ventricular area, myocardial wall thickness and endocardial contour lengths were also automatically assessed, using myocardial contours in 2-chamber, 4-chamber and short-axis view. In order to normalize the data, each myocardial characteristic was divided by the maximum value reached during the whole cardiac cycle. The evolution of normalized myocardial area along with

the mean of myocardial wall thickness and endocardial contours length were shown during the whole cardiac cycle.

6.3.7 Functional indices

Four functional indices were automatically estimated from myocardial contours and skeleton characteristics: ejection fraction (EF) ratio, diastolic fraction (DF) ratio, thickening fraction (TF) and LV rotation angle. Conventional ejection fraction ratio was calculated using endocardial curves of both, left and right ventricle (Equation 6.2). In 2-chamber and 4-chamber view, caps were added at atrioventricular junctions to close endocardial curve in order to estimate respective ventricular area (Figure 6.3).

$$EF\ (\%)\ =\ \frac{End\ diastolic\ area\ -\ End\ systolic\ area}{End\ diastolic\ area} \tag{6.2}$$

We also used the definition of the diastolic fraction ratio proposed by Okayama et al. [247] (Equation 6.3) and based on 30% diastolic return.

$$DF\ (\%) = \frac{Area\ at\ 30\%\ diastole\ -\ End\ systolic\ area}{End\ diastolic\ area -\ End\ systole\ area} \tag{6.3}$$

The thickening fraction (Equation 6.4) was based on the mean thickness of myocardial wall.

$$TF\ (\%)\ =\ \frac{End\ diastolic\ wall\ thickness\ -\ End\ systolic\ wall\ thickness}{End\ diastolic\ wall\ thickness} \tag{6.4}$$

Finally, to estimate LV rotation angle at the mid-ventricular level, the angle formed by the right ventricular insertion points in short-axis view (Figure 6.4) was followed during the whole cardiac cycle. Then, the maximal rotation angle through the cardiac cycle was further estimated in a global coordinate system.

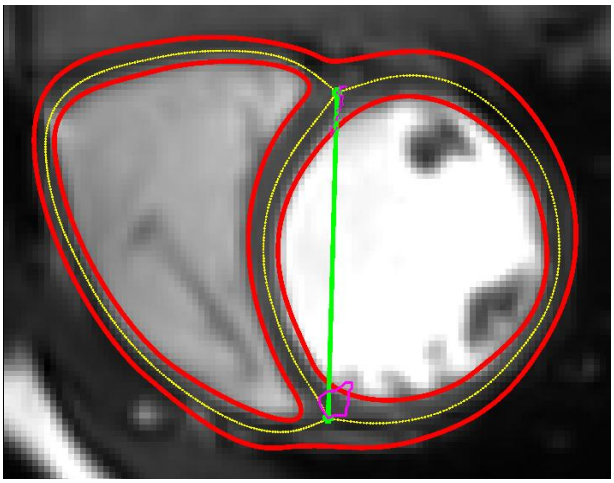

Figure 6.4: LV rotation angles measurement using short-axis junction points of the skeleton at mid-ventricular level.

6.3.8 Statistical analyses

In order to compare displacement patterns between SR and HR group and healthy volunteers, a Friedman repeated measures analysis of variance (ANOVA) on ranks was done on each displacement curve mean including 1-TS, 1-TDP and 1-END curves. However, to compare myocardial characteristics including myocardial area, endocardial contours length and wall thickness curves, a Kruskal-Wallis one-way ANOVA on ranks was done.

Functional indices were compared using a one-way analysis of variance. Similarly, when normality or equal variance tests failed, an analysis of variance on ranks using Kruskal-Wallis index was applied.

6.4 Results

6.4.1 Repeatability study

Intra-observer repeatability for myocardial area estimation was 97.3% and 96.3% for LV and RV contours, respectively. Thickness estimation repeatability was 96.2%, 96.7% and 97.3% for LV, SE and RV contours, respectively. In terms of contours position, the mean intra-observer position

error was 0.46mm, 0.43mm and 0.46mm from endocardial LV, endocardial RV and epicardial curve positions. Variations were higher at first image and tended to decrease through the cardiac cycle.

Inter-observer repeatability for myocardial area estimation was 77.9% and 91.9% for LV and RV contours, respectively. Extra-observator repeatability for thickness estimation was 80.5%, 83.2% and 73.3% for LV, SE and RV contours, respectively. The mean inter-observer position error was 1.85mm, 1.32mm and 1.04mm from endocardial LV, endocardial RV and epicardial curve positions. Again, variations were small at first image and tended to increase through the cardiac cycle.

6.4.2 Displacement patterns

Patterns of displacement were similar between cancer survivors and healthy volunteers (Figure 6.5). Cumulated displacements through systolic contraction, i.e., phase 1 to end-diastole (1-END) were significantly reduced in cancer survivors compared to healthy volunteers in all planes ($p<0.001$). Moreover, these differences were further amplified through the rest of the cardiac cycle.

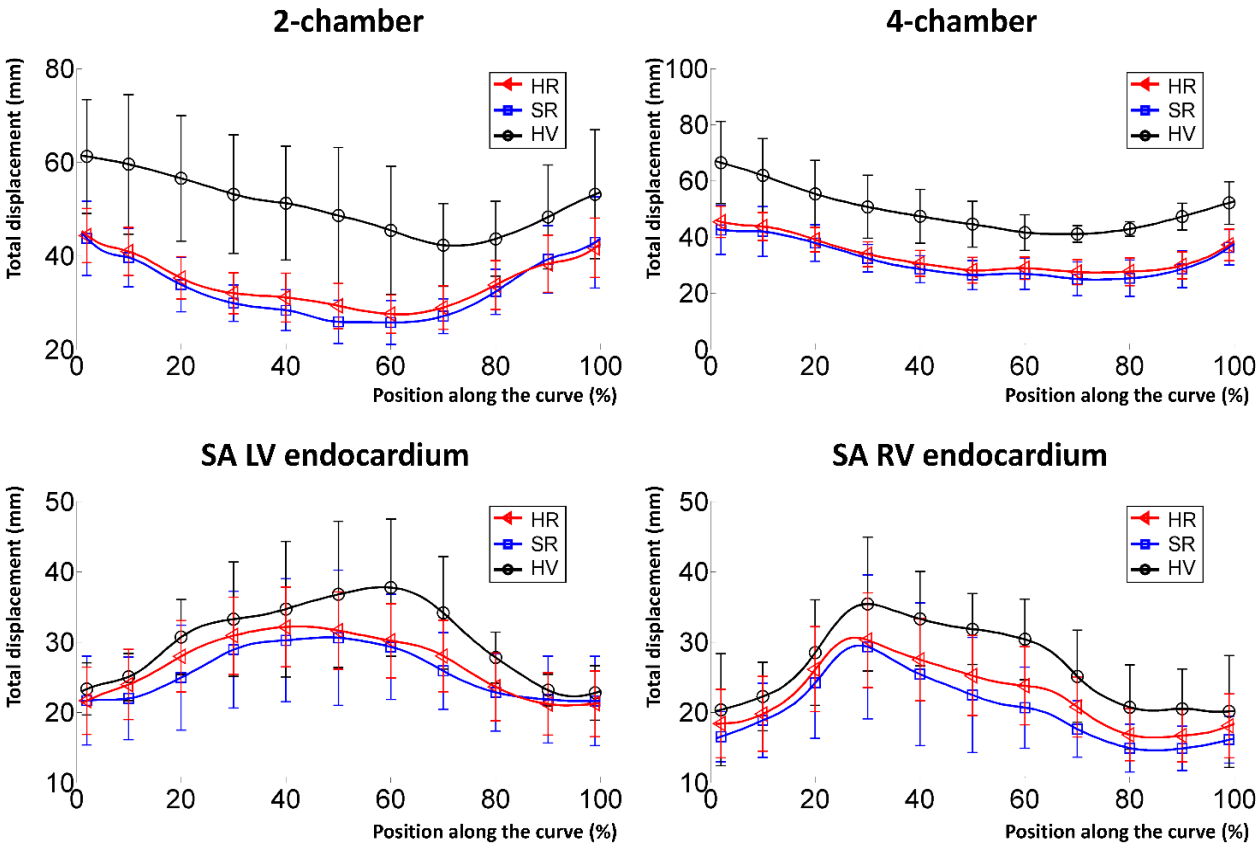

Figure 6.5: Myocardial displacement patterns generated during the whole cardiac cycle in 2-chamber, 4-chamber and short-axis (SA) views. Each curve represents unfolded contour displacement through the whole cardiac cycle.

6.4.3 Myocardial characteristics during the cardiac cycle

When looking into normalized LV area changes through the cardiac cycle in a 2-chamber view (Figure 6.6), healthy volunteers tended to have larger area changes compared to cancer survivors ($p<0.001$), especially during systolic contraction. This finding was further confirmed when comparing endocardial contour length evolution through the cardiac cycle. Likewise, myocardial contractile function, i.e. wall thickening, was reduced in cancer survivors compared to healthy volunteers ($p<0.001$). The same finding was seen in 4-chamber view (Figure 6.7). However, in short axis views (Figure 6.8), the differences in terms of ventricular area and endocardial contours length were smaller. On the other hand, the same findings were seen using right ventricular area,

length and wall thickness in a 4-chamber view. In short axis planes however, no differences were seen either between SR and HR or between the cohort of ALL survivors and healthy volunteers.

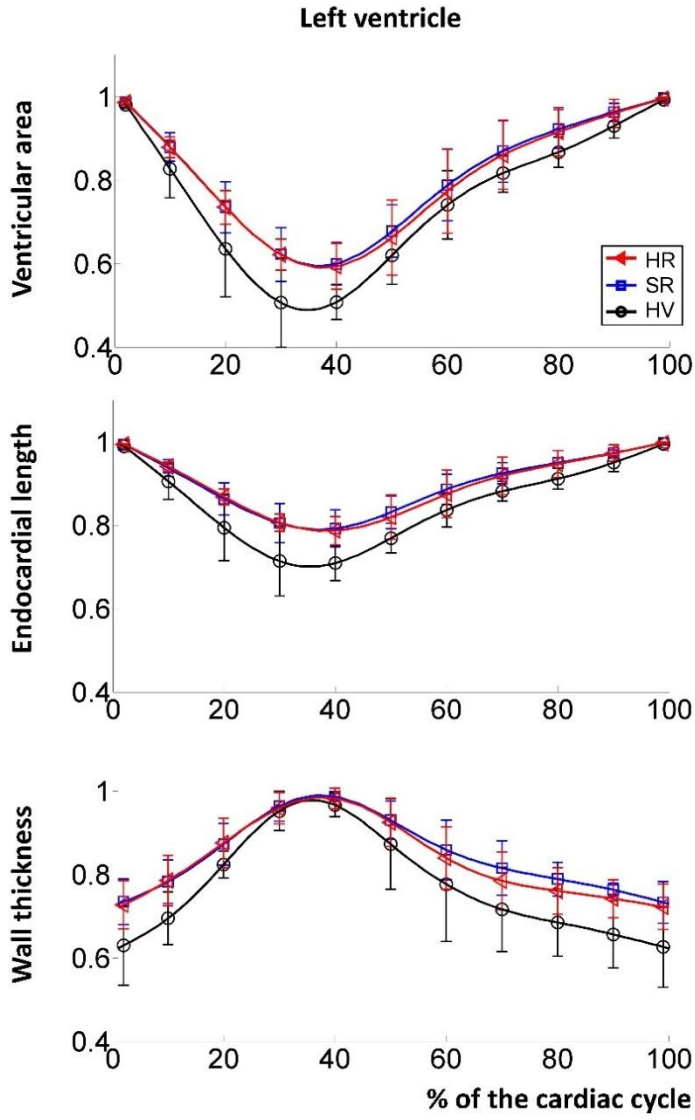

Figure 6.6: Normalized myocardial characteristics in 2-chamber view.

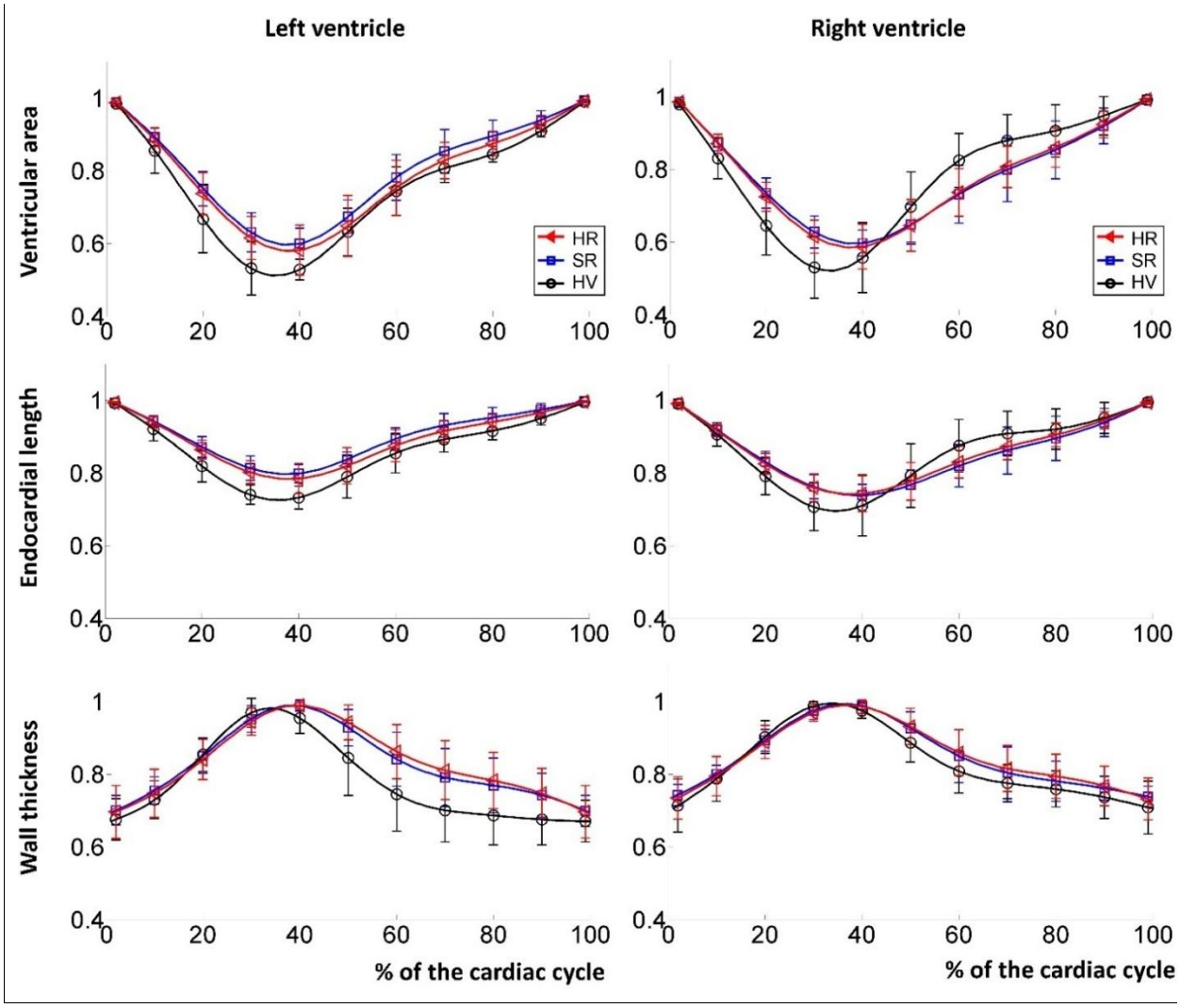

Figure 6.7: Normalized myocardial characteristics in 4-chamber view.

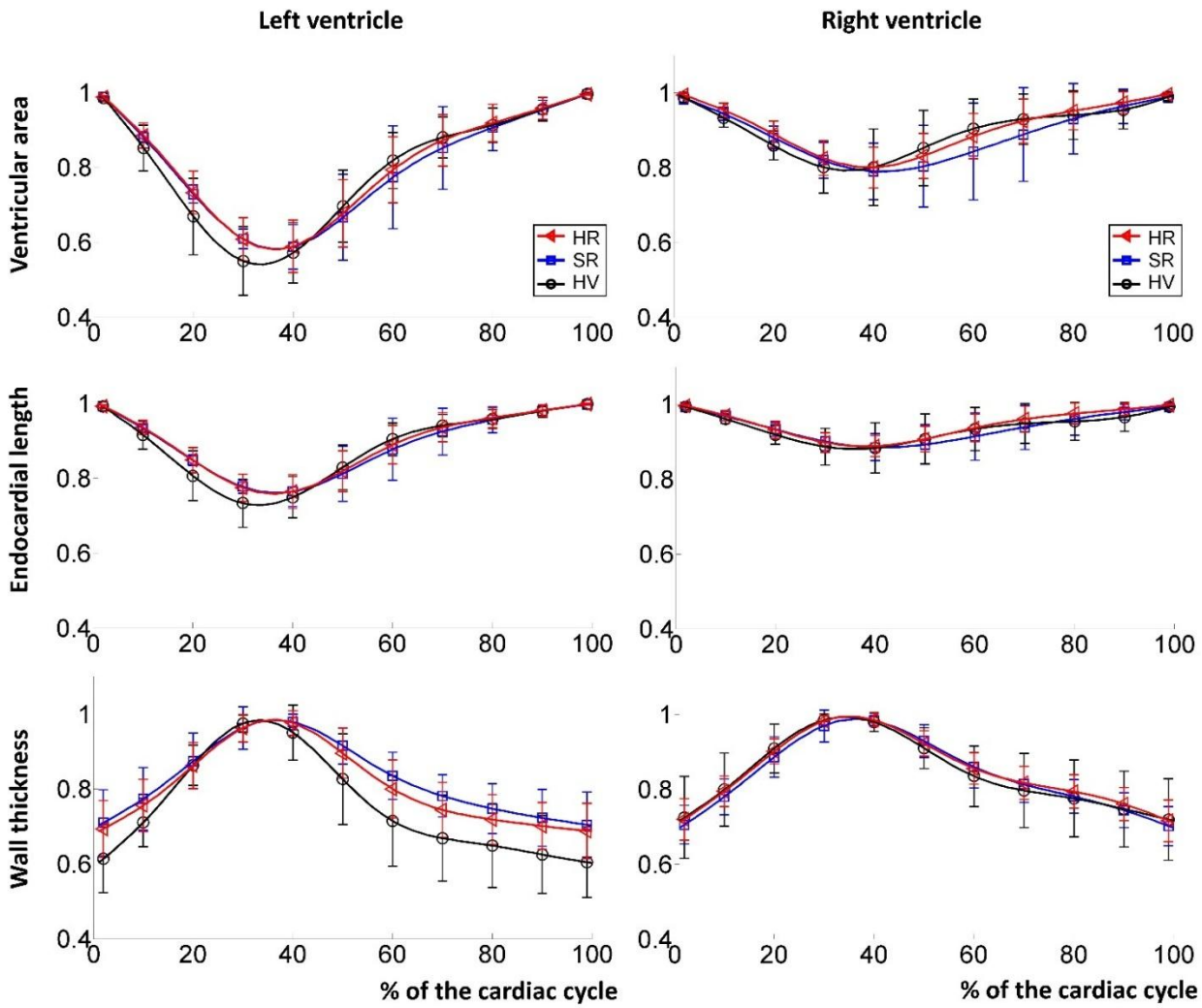

Figure 6.8: Normalized myocardial characteristics in short-axis view.

6.4.4 Functional indices

Thickening fraction remained similar between ALL survivors and healthy volunteers in all planes (Figure 6.9). LV ejection fraction was significantly reduced in ALL survivors compared to healthy volunteers when estimating it using 2-chamber (42±4% vs 53±6%, $p<0.001$) or 4-chamber (43±5% vs 50±4%, $p<0.001$) views. However, when using conventional short axis views, the index failed to detect any significant differences between both SR and HR groups (43±7% vs 43±6%, $p=0.37$) or between ALL survivors and healthy volunteers (43±6% vs 47±8%, $p=0.36$). Based on the standard deviation of indices from one volunteer to another, conventional ejection fraction index was the most stable as compared to the other indices as it had the lowest inter-volunteers standard deviation. The diastolic fraction in 4-chamber view was lower in ALL survivors as compared to

healthy volunteers (31±13% vs 50±16%, p=0.02), but only for the right ventricle. LV diastolic fraction in 4-chamber view was similar between ALL survivors and healthy volunteers (36±16% vs 35±20%, p=0.84). Similarly, LV diastolic fraction was similar between ALL survivors and healthy volunteers in 2-chamber (37±20% vs 40±15%, p=0.35) and short-axis views (42±18% vs 41±13%, p=0.44).

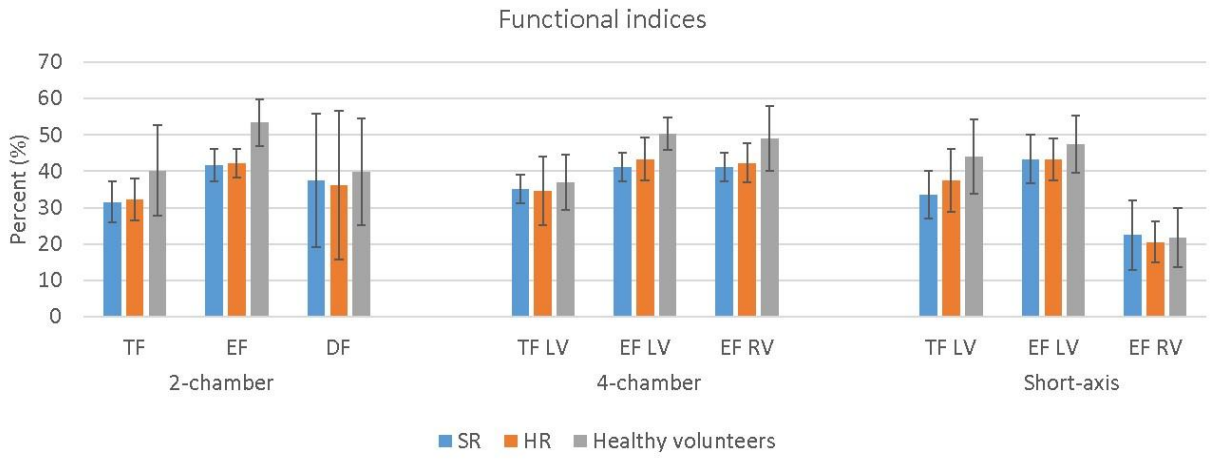

Figure 6.9: Myocardial skeleton-based functional indices in 2-chamber, 4-chamber and short-axis views. TF: thickening fraction, EF: ejection fraction, DF: diastolic fraction based on 30% diastolic return, RV: right ventricle, LV: left ventricle.

Cancer survivors had significant lower rotation angles (Figure 6.10) than healthy volunteers (5.7±2.5°, 8.6±4.2°, respectively, p=0.02). SR group had slightly lower rotation angle than HR group (4.9±1.1°, 6.1±2.9°, respectively, p=0.02). While most of ALL survivors had a stable clockwise and counter-clockwise twist, the overall normalized rotation seemed slightly unsynchronized with the cardiac cycle (Figure 6.10).

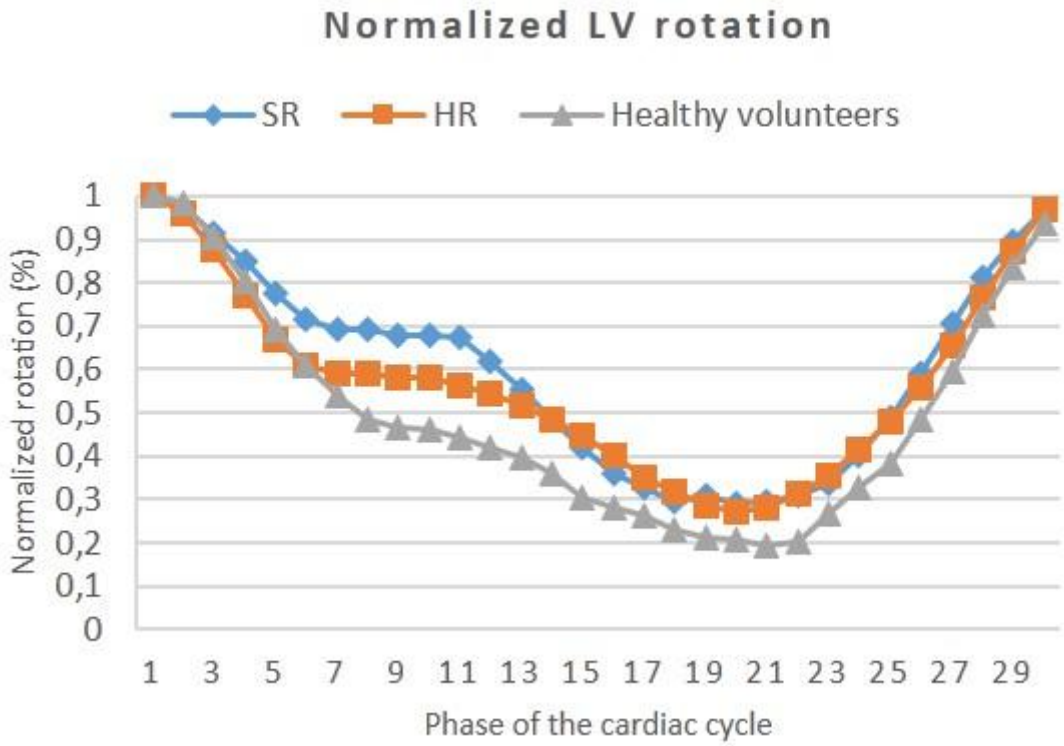

Figure 6.10: LV rotation angle distribution through the cardiac cycle.

6.5 Discussion

Parameters of myocardial displacement were found sensitive to identify abnormal function in patients after cardiotoxic chemotherapy. Their variation through the cardiac cycle allowed for a detailed analysis of functional abnormalities associated with doxorubicin therapy, more present during systole than during diastole. As traditional functional parameters were not significantly different between ALL survivors and healthy subjects, the data indicate that displacement parameters may be more sensitive biomarkers of doxorubicin-induced cardiotoxicity.

6.5.1 Advantages of skeleton-based technique

The proposed skeleton-based technique allowed for an accurate estimation of displacement patterns since displacements are calibrated using skeleton characteristics. Moreover, it did not require anatomical points to be manually selected as starting or ending points of contours. Such anatomical points are necessary in contour-based tracking [220] to associate contours from one phase to

another of the cardiac cycle. Using raw contours to track myocardial displacement, where displacements are obtained simply by subtracting position from one curve to another, induces sliding along myocardial contour curves that hampers the estimation of both, myocardial displacement patterns and functional indices. Even with the use of anatomical markers to parametrize myocardial contours, the induction of marker sliding along contours from one phase to another may be significant. Thus, anatomical markers were omitted during this study because of the difficulty finding a stable anatomical marker which can be accurately tracked through the whole cardiac cycle. Curvature-based tracking using raw contours to track myocardial displacement was also omitted for the same reasons. On the other hand, this sliding phenomenon was significantly reduced when using skeleton-based tracking due to the skeleton characteristics and curves that are relatively stable from one phase to another. The advantage of using kriging interpolator over a divergence-free displacement field [243, 159] is that we can smooth myocardial displacements when required. Smoothing is important especially when segmentation errors generate important noise within myocardial wall.

6.5.2 Segmentation errors and data normalization

All functional indices presented in this study were estimated automatically during the post-segmentation process, thus the accuracy of post-processing parameters was mostly dependent on the segmentation, which was the main source of errors. Reported segmentation errors for short axis cine-CMR images (1 to 3 mm) are equal to slightly higher than our inter-observer repeatability, but higher than our intra-observer repeatability [232, 248]. Small variations between ALL survivors in terms of contours geometry were noted mainly in 2-chamber and 4-chamber views, however, these variations are induced due to CMR acquisitions, more specifically, due to three-dimension slice localization. As opposed to whole-cycle tracking, functional indices required segmenting two or three phases instead of all phases of the cardiac cycle, thus involve less image processing. Furthermore, most of indices and results shown in this study were normalized to limit their sensitivities to image acquisition parameters and allow inter-volunteers comparison. It is important to keep in mind that from one survivor to another, myocardial geometry may change significantly. Orientation and position of MR acquisition plane along with the overall volume of the heart, which may also vary significantly, may further confirm the need to normalize both input and output data to allow inter-volunteers comparison.

6.5.3 Myocardial displacement patterns in cancer survivors

The similar myocardial displacement patterns between cancer survivors and healthy volunteers suggested that myocardial contours followed a specific signature in terms of displacements and this signature of displacements remained unchanged. The higher amplitude in healthy volunteers compared to ALL survivors along most of myocardial contours suggested that myocardial strain, conventionally investigated by echocardiography, may be reduced in this cohort of cancer survivors as it was found in an animal model [35]. Systolic dysfunction appeared with a reduction in both longitudinal and circumferential strain, while LV ejection fraction remained within the normal range in anthracycline-treated cancer survivors [249]. Radial displacement was also reported to be lower in anthracycline-treated cancer survivors [250]. Such parameters, used to quantify myocardial mechanics, may be predictors for overall mortality and major cardiac events following anthracycline-based treatments [250, 249]. Longitudinal strain in particular seem to have superior prognostic value when it comes to detecting clinical heart failure [249]. The fact that the same finding was seen in 2-chamber, 4-chamber and short-axis views, including both left and right ventricular endocardial curves, suggested that the whole 3D deformation of the heart may become altered due to doxorubicin-based treatment.

6.5.4 Myocardial characteristics

When comparing ventricular area and myocardial contour length, normalized ventricular area was the most stable parameter, i.e., with smallest inter-subject variations. Its similar evolution through the cardiac cycle between SR and HR group suggested that this parameter is insensitive to the risk factor. However, 10 survivors within the HR group received Dexrazoxane as a cardioprotective agent, which may have inhibited doxorubicin-induced cardiotoxicity and narrowed the differenced between SR and HR group in our cohort of patients. The differences between ALL survivors and healthy volunteers in 2-chamber and 4-chamber views, especially during systole, suggested that there is a clear reduction of cardiac output in ALL survivors. In these settings, we believe that the use of LV volumes may rather be more appropriate as it was previously reported that LV end-systolic volume significantly increases in cancer survivors [251-253], which may be a sign of early cardiotoxicity. An increase in LV end-systolic volume should be expressed by a lower ejection fraction. However, measuring volumes is more stable than quantifying the two dimensional ventricular area since such measurement is insensitive to errors due to slice position during images

acquisition. Contours length on the other hand was also stable from one volunteer to another. However, the smaller amplitudes of contours length compared to ventricular area induced less susceptible differences between ALL survivors and healthy volunteers.

6.5.5 Functional indices

The use of anthracyclines was previously reported to induce a reduction in the LV wall-thickness along with thickness-dimension ratio [254]. However, in our study the LV myocardial wall thickening fraction remained similar between ALL survivors and healthy volunteers in all myocardial planes, which suggested that the contractile function of the myocardium may not be as affected as previously found [254]. On the other hand, the fact that the distribution of normalized wall thickness over the cardiac cycle was lower in ALL survivors compared to healthy volunteers in 2-chamber and 4-chamber but not in short-axis gives different views on such parameter.

The LV ejection fraction was expected to be reduced [4, 8]. A significant reduction however was only observed when measurements were performed in 2-chamber and 4-chamber views, which might be due to the presence of regional myocardial tissue damage. Dietz et al. [250] reported a non-significant trend for a lower ejection fraction in cancer survivors. Several other studies however reported a significant reduction. In a report including 62 cancer survivors, subnormal LV ejection fraction was detected in 61% of cancer survivors while right ventricular ejection fraction in 53% [251]. In another study including 64 cancer survivors imaged with CMR, 49 (77%) had an abnormal LV ejection fraction [252]. In this study, the two methods used to calculate the ejection fraction, using either myocardial contour length or myocardial area, gave the same results. A significant reduction was seen in 2-chamber and 4-chamber views while normal values were obtained in conventional short axis views, which indicates subclinical changes of ventricular function. On the other hand, LV diastolic fraction ratio, which was expected to be reduced due to doxorubicin-based therapy [249], also failed to detect differences between cancer survivors and healthy volunteers using either 2-chamber, 4-chamber or short-axis view. Though, this index was less stable due to its higher standard deviation compared to other indices. Though, a further look at this index should be made, since it may detect abnormal myocardial diastolic function that is often reported in cancer survivors [255, 137, 256].

6.5.6 LV rotation

The reduction of LV rotation in cancer survivors confirm previously reported findings [257] and suggests a possible alteration of fiber integrity. LV rotation is a phenomenon seen in short axis views where the heart undergoes a rotation pattern during each cardiac cycle. LV rotation is closely related to both, systolic and diastolic function when acquired during the whole cardiac cycle and may be altered in multiple diseases such as systolic or diastolic heart failure, dilated cardiomyopathy, hypertrophic cardiomyopathy and constrictive pericarditis [258]. LV rotation is maximal during both clockwise and counter-clockwise rotation at the apex and minimal at basal level. Contrary to tagging MRI where tag lines tend to disappear at the end of systole contraction [259], thus limiting estimation accuracy, skeleton-based estimation is not sensitive to the phase of the cardiac cycle. The reported mean rotation angle at mid-ventricular level in healthy humans is 3.7±0.8° at epicardium and 7.0±2.1° at endocardium [260]. However, using circumferential points on tagging MRI to estimate LV rotation may provide variable results due to non-uniform deformation of the myocardium. Moreover, rotation angles differ significantly between endocardial- vs. epicardial-based measurement. A further look into this index in cancer survivors and healthy volunteers may be required to further assess its use as a new biomarker of LV rotation and as a potential clinical index of myocardial contractile function.

6.5.7 Study limitations

Three main limitations were encountered during this study. Firstly, the through-plane motion was not taken into account when estimating myocardial displacements. Thus, the 2D/planar analysis of displacements may not provide full characterization of myocardial behaviour. However, the same problem arises when using echocardiography images. Secondly, the duration of the different cardiac intervals (early and late diastole) were relatively different from one volunteer to another, thus, required manual selection of each key phase of the given cardiac interval, which added one to two minutes to process volunteers' data. Thirdly, this study included only 26 ALL survivors and 6 healthy volunteers. Though, a larger cohort of volunteers may be required to further confirm our findings.

6.6 Conclusion

Skeleton-based myocardial analysis provided new insights in terms of both local and global myocardial displacement patterns. The technique is less sensitive to tracking errors as resulting skeleton displacements are more stable than contour-based displacements and most importantly make the analysis of the cardiac function easier. Within the cohort of volunteers that were assessed in this study, displacement patterns were significantly lower in cancer survivors compared to healthy volunteers, although the signature of displacement curves remained similar. The use of skeleton-based myocardial tracking should further be considered and may open doors to a future three-dimensional tracking of the myocardium.

Acknowledgment

This work was financially supported by the Cole Foundation, the NSERC (Discovery grant and CREATE-MEDITIS Program), the FRQNT (team grant) and the CIHR (team grant). The authors would also like to thank Guillaume Gilbert for the acquisition of preliminary MRI data and technical assistance provided during the study.

CHAPTER 7 ARTICLE 4: MYOCARDIAL 2D STRAIN AND STRESS INDICES FOR THE DETECTION OF CARDIOTOXICITY IN ACUTE LYMPHOBLASTIC LEUKEMIA SURVIVORS

Mohamed Aissiou[1,2], Farida Cheriet[1,3], Daniel Curnier[2,5], Caroline Laverdière[2], Maja Krajinovic[2], Daniel Sinnett[2], Gregor Andelfinger[2], and Delphine Périé[1,2*]

[1]Mechanical Engineering Department, École Polytechnique de Montréal, Montreal, Canada.

[2]CHU Sainte-Justine Research center, Montreal, Canada.

[3]Computer and Software Engineering Departement, École Polytechnique de Montréal, Montreal, Canada.

[4]McGill University, Montreal, Canada

[5]Kinesiology Department, University of Montreal, Montreal, Canada.

7.1 Abstract

Background: Doxorubicin-based chemotherapy is an effective treatment for cancer, however its successes are hindered by its alterations of myocardial physiology at multiple stages. From molecular scale up to morphological and functional scale, the induction of multiple cardiotoxicities is reported. However, the heart is relatively complex to track since it has much fewer anatomical landmarks than other organs. The aim of this study was to develop a method based on cardiovascular cine-MRI and finite element modeling to evaluate 2D myocardial regional mechanical strain and stresses in childhood acute lymphoblastic leukemia (ALL) survivors who previously received doxorubicin therapy. We hypothesized that mechanical strain and stresses will enable the detection of any alterations to both contractile and relaxation functions of the myocardium.

Methods: We prospectively included 26 ALL survivors who underwent a doxorubicin-based chemotherapy for childhood leukemia and 6 healthy volunteers (HV). The ALL survivors group was divided into a standard risk (SR) group (n=8) and a high risk (HR) group (n=18), based on the cumulative doxorubicin dose received during treatment, age at the beginning of the treatment and other clinical factors. The MRI protocol consisted of an ECG-gated cine TruFISP sequence using

a Siemens 3T MRI system. Myocardial contours were semi-automatically segmented on the mid-ventricular 2-chamber, 4-chamber and short-axis images using an interactive implementation of cubic Bezier curves. Myocardial geometry was meshed at each phase of the cardiac cycle, and then deformed with myocardial displacements obtained from the calibrated contours. Strain and stresses were estimated using hyperplastic finite-element model and either linear or cumulative technique. Linear technique required only the first and last phases of the given cardiac interval while cumulative technique required each phase to be segmented and transitory strain and stresses cumulatively added through the cardiac interval. Mean strain and stresses (XY resultant or von Mises index) were evaluated during systole, early diastole and late diastole intervals. Statistical comparison between volunteers was done using a one-way analysis of variance.

Results: Von Mises strain and stresses were higher than XY strain and stresses during systole, early and late diastole. Linear strain and stresses were comparable to cumulative strain during systole. However, during diastole, cumulative strain and stresses were higher than linear strain and stresses. These differences were observed within the whole myocardial area rather than specific to some myocardial segments. During early diastole, myocardial strain remained similar between the groups ($p>0.1$). However, during late diastole, myocardial strain were significantly reduced in SR and HR groups compared to healthy volunteers ($p<0.004$). Myocardial stresses were significantly reduced during early diastole in SR and HR groups compared to healthy volunteers, but only in 4-chamber view (9.69 ± 4.91 kPa and 9.90 ± 4.51 kPa vs. 13.52 ± 6.00 kPa, respectively, $p=0.04$). During late diastole, myocardial stresses were reduced in both 2-chamber (8.55 ± 2.98 kPa and 6.59 ± 1.50 kPa vs. 10.6 ± 3.6 kPa, $p=0.004$) and 4-chamber (8.05 ± 4.18 kPa and 6.69 ± 2.53 kPa vs. 10.2 ± 4.3 kPa, $p=0.023$) views.

Conclusion: Our new skeleton-based technique provided robust results and accurate tracking of myocardial tissue for further quantification of apparent strain and mechanical stresses. Cumulative-based estimation of strain and stresses allows mesh restructuration at each phase and thus, is more appropriate for large displacements. The apparent strain and stresses were significantly lower in doxorubicin-treated ALL survivors, which may indicate a reduction in myocardial contractile and relaxation function. Taking into account the non-linear myocardial displacements through this cumulative-based estimation of strain and stresses help in detecting any alterations in myocardial tissue properties.

7.1.1 Keywords

Myocardial stresses, myocardial strain, finite-element modelling, doxorubicin-induced cardiomyopathies, chemotherapy, cine-CMR

7.2 Introduction

Doxorubicin-based chemotherapy is known as an effective treatment for cancer, however its successes are hindered by its alterations of myocardial physiology at multiple stages. At molecular scale, doxorubicin is known to induce reactive oxygen species [11, 13]. At electrophysiological scale, it induces premature ventricular contraction [4] and sinus tachycardia [2]. Lastly, at morphological and functional scale, the induction of wall thinning [7, 4] or ventricular contractile dysfunction [35, 4] is reported.

The use of mechanical strain and stresses may provide useful knowledge that may help in detecting doxorubicin-induced damage at a functional scale. Such parameters play an important role in the mechanical function of the heart [261], especially during passive ventricular filling. Reported use of these mechanical parameters include myocardial ischemia [262], systolic dysfunction [263] and regional myocardial function quantification [264, 265]. Most of reported studies use echocardiography to estimate myocardial strain and stresses. However, the geometric assumptions behind echocardiography, which affect both the M mode and two dimensional (2D) echocardiography, may lead to inaccurate measurement of strain and stresses [47].

Accurate estimation of myocardial strain and stresses requires accurate tracking of myocardial displacements. However, the heart is relatively complex to track since it exhibits much fewer anatomical landmarks than other organs such as the brain [266]. The standard technique used to track myocardial displacements remains the tagging sequence [267, 268]. Such technique requires complex algorithms and a contour model to track myocardial displacements, and its accuracy decreases through the cardiac cycle as the tagging signal decreases due to spin-lattice relaxation of the tagged tissue [269]. Alternative methods used to track myocardial displacements include elastic registration technique, where displacements are usually obtained directly from a phase-by-phase registration [270-273, 239]. Another technique is the contour-based segmentation with a model-based tracking, where the intra-myocardial displacement is interpolated from resulting contour displacements [274, 151]. Many of these 2D models serve as building stages for a 3-dimensional

model, which are more appropriate to take into account the through-plane motion for a better characterization of myocardial mechanical characteristics.

Reported finite element (FE) models include a promising 2D stochastic FE framework that simultaneously estimates left ventricular myocardium kinematics and mechanical parameters using a dynamic equation accounting for mass, damping and stiffness properties [71]. This model uses a contour-based tracking technique [275], but does not seem to exclude trabeculae carneaes during segmentation process, which can generate important errors in mechanical properties estimation. A 3D-based biventricular FE model was also proposed from interactive segmentation of cine MRI images and automatic reconstruction using 2D control curves [61]. The combined use of electrophysiological and mechanical heart models is also worth considering since they provide unprecedented potential to quantify myocardial alterations [61], especially in 3D analysis. Such models may not only allow the development of more sensitive clinical indices to detect cardiomyopathies [61], but also to locate regional alterations. However, although the model allows a direct estimation of myocardial mechanical properties, several limitations remain considerable including the absence of a robust parametric model. While the model does not incorporate patient-specific fibers orientation, it can generate fibers orientation from statistical atlas information. Such property is necessary in detecting regional alterations of the myocardium. A complete geometric model including both the ventricular and atrial part was obtained from an iterative adaptation approach using tomographic data, with reported segmentation errors of 4.5-7mm [62]. Another 3D FE model can automatically generate personalised biomechanical models from 3D cardiovascular images [63]. Although the model is fairly complex, include fibers orientation and allow the simulation of both systole and diastole, it however lacks the inclusion of the right ventricle. None of the FE based biventricular models [67, 57, 276, 277] provided the possibility of quantifying local myocardial alterations, as they are not parameterized and cannot be divided into the standard 17 segments model.

3D FE models have the advantage to represent the complex physiological behavior of the heart. However, due to the lack of myocardial subdivision standard, we chose a 2D analysis of myocardial mechanical strains and stresses. We hypothesized that 2D mechanical strain and stresses enable the detection of any alterations to both contractile and relaxation functions of the myocardium. The aim of this study was to develop a method based on cardiovascular cine-MRI (cine-CMR) and FE

modeling to evaluate 2D myocardial regional mechanical strain and stresses in childhood ALL survivors who previously received doxorubicin therapy for leukemia.

7.3 Methods

7.3.1 Cohort of volunteers

After approval by the institutional Review Board (IRB) and obtaining informed voluntary consent, we prospectively included 26 ALL survivors, from the PETALE study [192] and 6 healthy volunteers. These ALL survivors have previously undergone a doxorubicin-based chemotherapy for childhood leukemia. Within the ALL survivor group, eight (n=8) were included in the standard risk (SR) group and eighteen (n=18) were included in the high risk (HR) group, based on a risk index related to the severity of the pathology, cumulative doxorubicin dose and volunteer's age [245, 246]. 13 ALL survivors were male and 13 were females with an average at-acquisition weight and height of 1.7 ± 0.1m and 71.3 ± 13.8kg, respectively. Treatment was received on an average of 2.0 ± 0.5 years post-diagnosis whereas MRI acquisitions were made 13.6 ± 7.3 years post-treatment. The ALL survivors received doxorubicin doses of 241 ± 97 mg/m^2 while 10 of the HR group received dexrazoxane doses of 2749 ± 463 mg/m^2. The healthy volunteers (HV) mean age was 34 ± 9 year while their mean weight was 59 ± 7 kg.

7.3.2 MRI acquisition

The MR protocol consisted of an ECG-gated cine TruFISP sequence acquired during breath-holds, using a Siemens 3T MR system. Acquisition parameters were slice thickness 8 mm, repetition time 34.5 ms, effective echo time 1.2 ms, flip angle 36°, iPAT factor 3, matrix 208 × 210 and pixel spacing 1.25 × 1.25 mm. Approximately 14 slices were acquired in short-axis and 5 slices in long axis 4-chamber and 2-chamber views. For each slice, 25 phases of the cardiac cycle were acquired during multiple breath-holds. The overall acquisition time including the 3-plan Localizer scan was approximately 15 minutes.

7.3.3 Myocardial contours tracking

Myocardial contours were semi-automatically segmented using an interactive implementation of cubic Bezier curves. Segmentation was done at the mid-ventricular level in short-axis, 2-chamber

and 4-chamber views. Once the first phase was segmented, at each following phases a template, based on the previous phase, was proposed where the user needs only to apply relative displacement from one phase to another to limit intra-operator errors. In short axis view, three curves were used to segment myocardial area: endocardial left and right ventricular curves and epicardial curve whereas in 2-chamber and 4-chamber views, only one curve was required to segment the whole myocardial area (Figure 7.1). Resulting curves were re-parameterized using "cumulative percentage length" discretization and smoothed using geometrical kriging [215]. Intra-myocardial displacements were estimated using a skeleton-based approach. From binary myocardial mask, a skeleton algorithm [194] was used to extract skeleton curves along with ending and junction points. Finally, end and junction points were further processed to compute perpendicular projections onto initial myocardial contours. Myocardial contours characteristics and endocardial curves directions are shown in Figure 7.1.

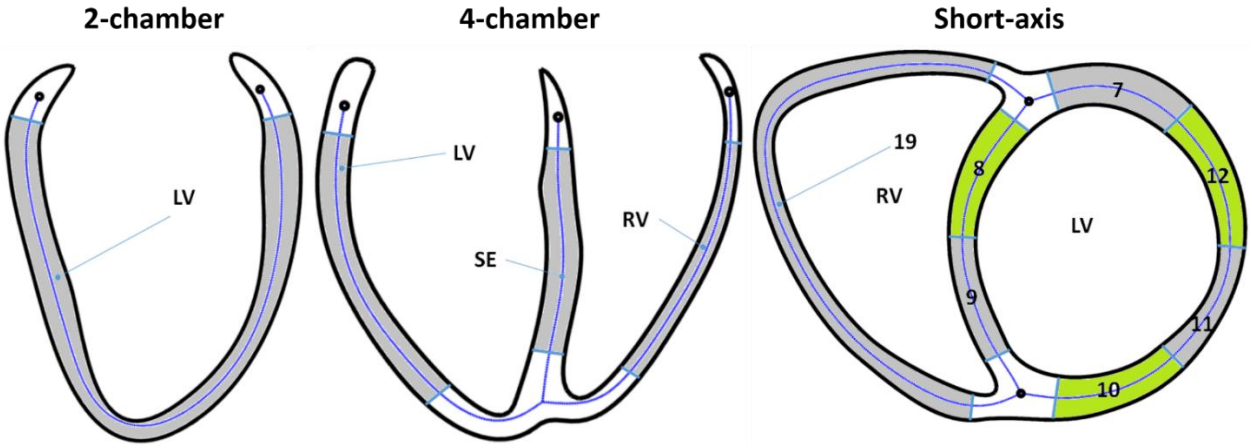

Figure 7.1: Myocardial regions for strain and stresses estimation. Legend: LV: left ventricle, SE: septum, RV: right ventricle. Note: numbers 7 to 12 and 19 correspond to myocardial segments based on the standard 17-segment AHA model.

7.3.4 Myocardial strain and stresses estimation

We used an isotropic hyperplastic model with a discrete distribution of Young's Modulus (Equation 7.1) estimated from published data [73], based on different strain (ϵ) intervals:

$$Young\ Modulus_i\ (\mathrm{N/mm^2}) \approx \begin{cases} 0.013\,, & \epsilon = 0.00,\ ..\ 0.05 \\ 0.016\,, & \epsilon = 0.05,\ ..\ 0.10 \\ 0.064\,, & \epsilon = 0.10,\ ..\ 0.15 \\ 0.1\,, & \epsilon = 0.15,\ ..0.20 \end{cases} \tag{7.1}$$

In a first step, the cardiac cycle was divided into three main intervals which included systole, early diastole (ED) and late diastole (LD) (Figure 7.2). Selection of the beginning and last phase of each interval was done manually by selecting end-systolic and end of early diastole phases. End diastole, i.e., start of systole, happened to always be the first phase as the MRI acquisition was ECG gated with the cardiac cycle. In a second step, myocardial geometry was meshed at each phase of the cardiac cycle using a meshing algorithm that generates 2D unstructured triangular meshes [278]. In a third step, intra-myocardial displacements were injected as loading condition into the FE model. In a fourth step, strain and stresses were estimated using either linear or cumulative technique (Figure 7.2). Linear technique required only the first and last phase of the given cardiac interval in order to estimate strain and stresses. However, cumulative technique required each phase to be segmented. The initial phase was geometrically deformed using kriging interpolator to fit the next phase in order to estimate transitory strain and stresses. These transitory strain and stresses were then cumulatively added through the cardiac interval. Finally, strain and stress indices were displayed using either XY resultant (Equation 7.2) or von Mises index (Equation 7.3), with plane stress assumption in a global coordinate system. For a given phase A-to-B simulation, results are always shown in the final resulting phase, for consistency.

$$\sigma_{XY} = \sqrt{{\sigma_X}^2 - {\sigma_Y}^2} \tag{7.2}$$

$$\sigma_{VM} = \sqrt{{\sigma_X}^2 - \sigma_X\sigma_Y + {\sigma_Y}^2 + 3{\sigma_{XY}}^2} \tag{7.3}$$

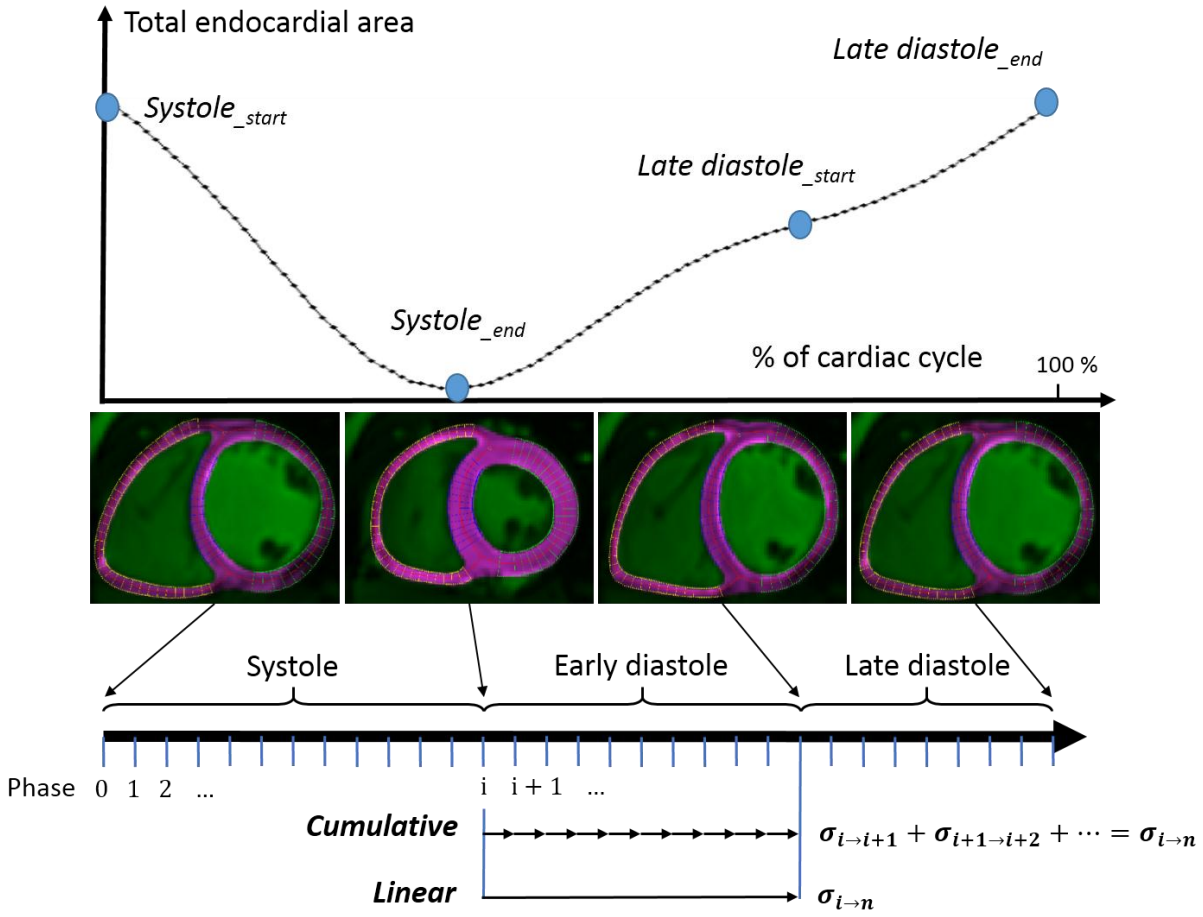

Figure 7.2: Comparison of linear and cumulative methods from stresses and strain estimation.

7.3.5 Strain and stresses sensitivity to segmentation errors

Contour repeatability and reproducibility were previously assessed. To summarize, for intra-observator repeatability, the same cine-CMR images were given blindly 5 times to the same operator. The main rules included: segmentation of myocardial contours using a closed contour curve, exclusion of auricular myocardium, exclusion of the papillary muscle and others software-related constraints such as where and in which direction to begin each myocardial contour curve. Once contours were segmented, the repeatability was evaluated in 2-chamber, 4-chamber and short-axis view using a standard deviation-based estimation model (Equation 7.4).

$$repeatability\ (\%) \approx 100 - \frac{100\ x\ Standard\_deviation(index)}{mean(index)} \quad (7.4)$$

Where $index$ represents either the resulting strain or stresses from one segmentation to another. For inter-observator repeatability, the same short-axis images were segmented blindly by three different operators using the same rules. Generated strain and stresses during systole were therefore used to estimate repeatability.

7.3.6 Statistical analysis

Statistical comparison between ALL survivors and healthy volunteers was done using a one-way analysis of variance (SigmaPlot 12.0, Systat Software, Inc., Point Richmond, CA). When normality test failed, a Kruskal-Wallis one-way analysis of variance on ranks was done.

7.4 Results

7.4.1 Repeatability study

Intra-observervator repeatability for myocardial strain estimation was 87.0% and 92.0% and 91.3% for 2-chamber, 4-chamber and short axis, respectively. Intra-observervator repeatability for myocardial stresses estimation was 74.8% and 85.7% and 86.4% for 2-chamber, 4-chamber and short axis, respectively. Myocardial stresses were slightly less repeatable than myocardial strain. In terms of mean strain estimation, the standard deviation of resulting strain was 16.8%, 10.9% and 7.4% in 2-chamber, 4-chamber and short axis, respectively. The standard deviation of resulting stresses was 20.4 kPa, 8.90 kPa and 4.30 kPa in 2-chamber, 4-chamber and short axis, respectively. Inter-observator repeatability for systolic strain and stresses estimation were 83% for strain and 70% for stresses. The standard deviation was 42% for strain and 28.6 kPa for stresses.

7.4.2 XY versus von Mises representation of strain and stresses.

Von Mises strain were higher than XY strain during systole, early and late diastole (Figure 7.3). The same finding was seen when estimating myocardial stresses.

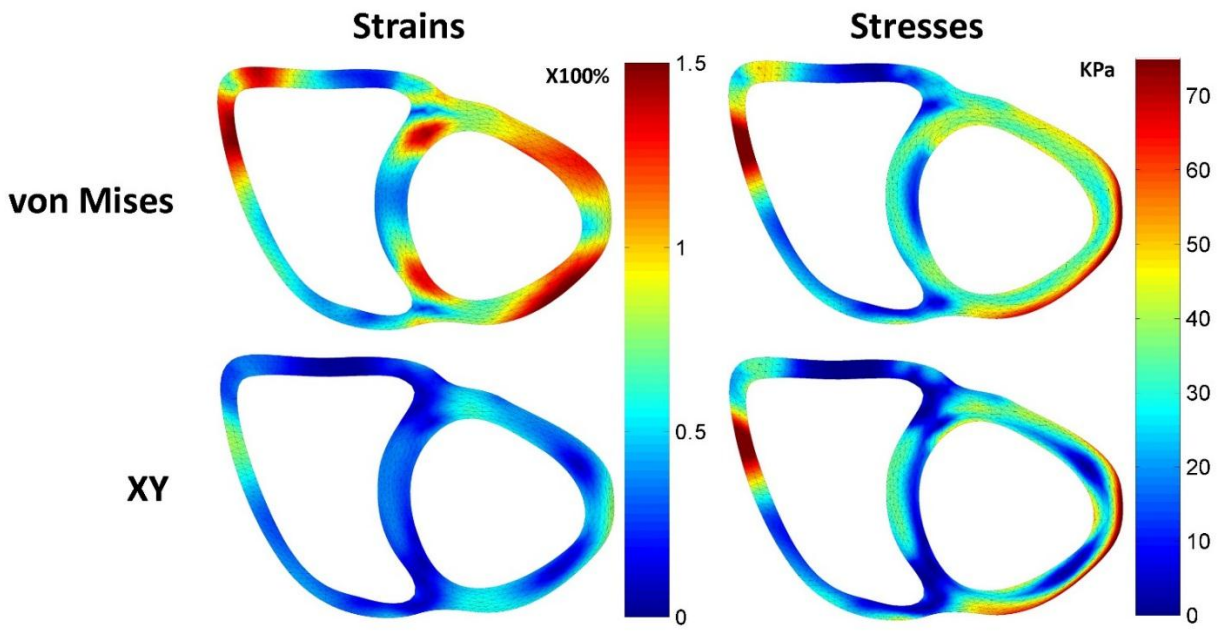

Figure 7.3: Comparison of linear von Mises and linear XY strain and stresses during diastole.

7.4.3 Linear versus cumulative strain and stresses

Linear strain were comparable to cumulative strain during systole (Figure 7.4). However, during diastole, cumulative strain were higher than linear strain. These differences were observed within the whole myocardial area rather than specific to some myocardial segments. Linear strain during systole were slightly higher than linear strain during diastole. However, cumulative strain during diastole were slightly higher than cumulative strain during systole. Furthermore, both linear and cumulative strain were higher during early diastole than during late diastole.

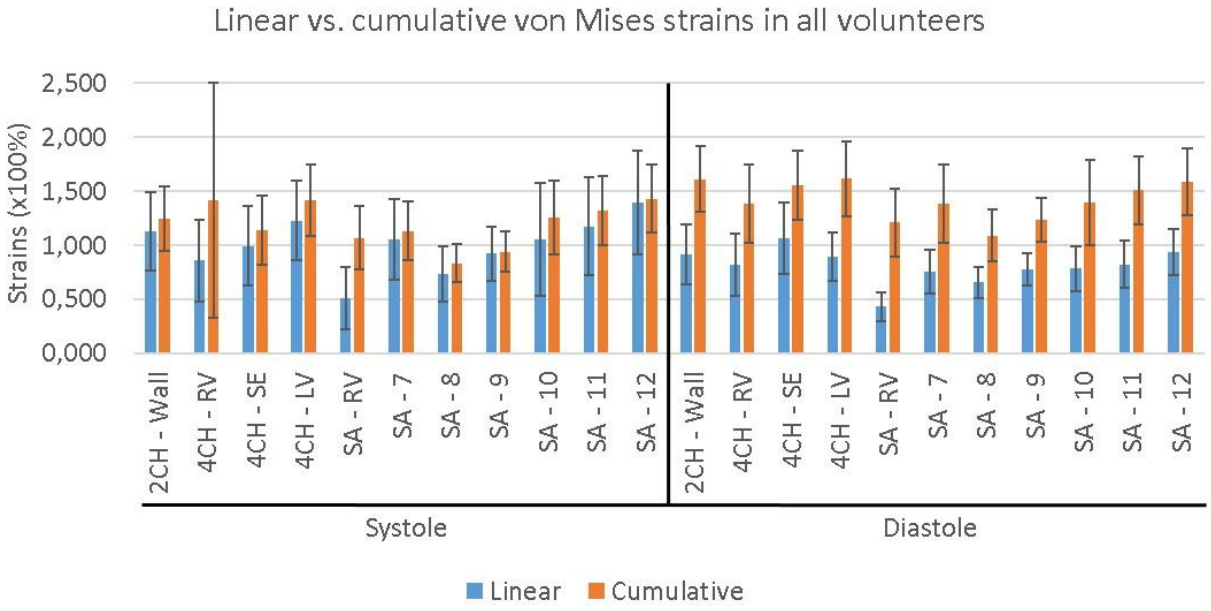

Figure 7.4: Comparison of linear and cumulative strain in the different myocardial segments. Legend: RV: right ventricle, LV: left ventricle, SE: septum, SA: short axis.

Stresses, but not strain, were underestimated when using cumulative estimation technique compared to the linear estimation technique (Figures 7.5 and 7.6). Strain and stresses generated during early diastole tended to be higher compared to strain and stresses generated during late diastole. All these finding were seen in both ALL survivors (both HR and SR groups) and healthy volunteers.

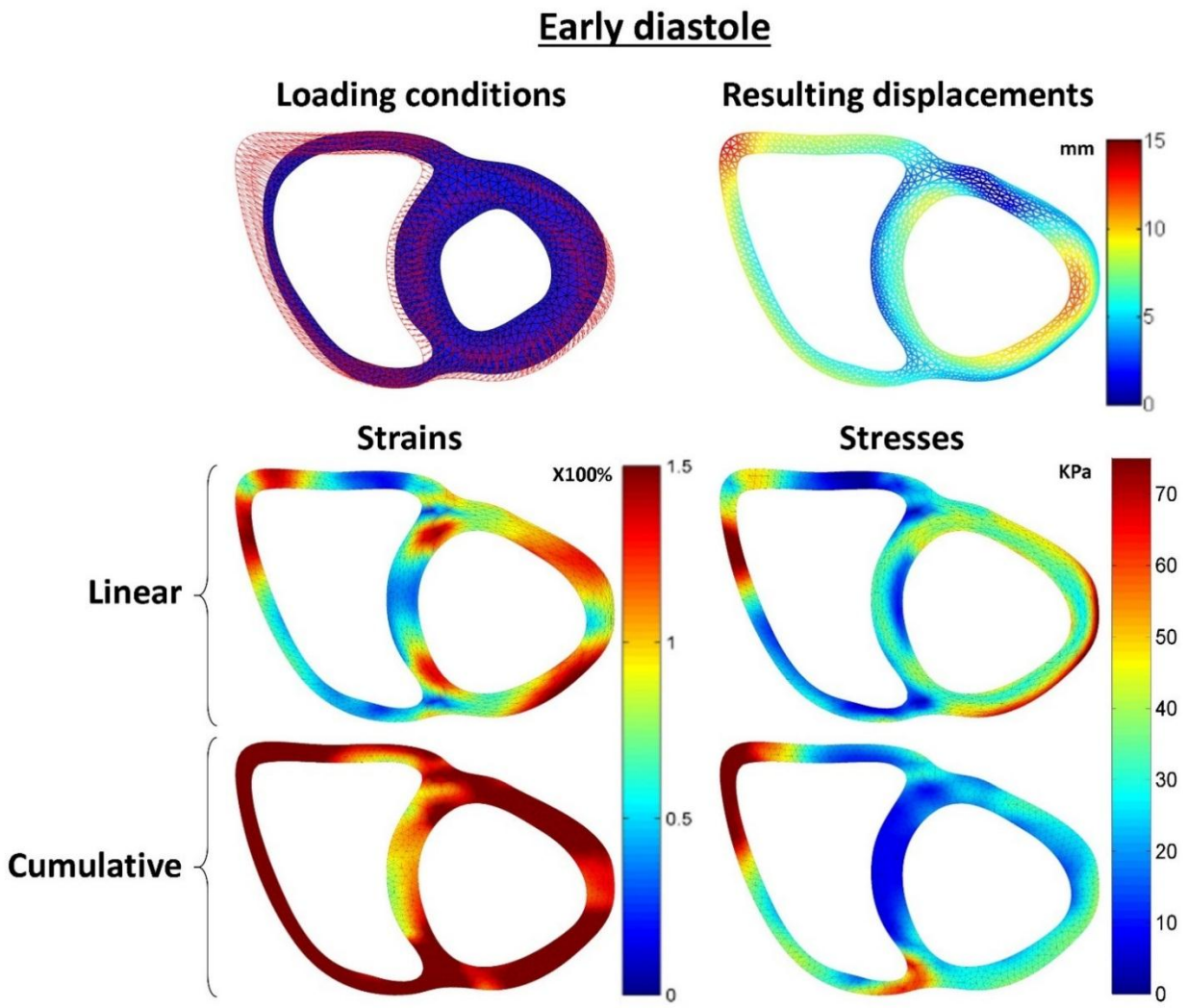

Figure 7.5: Early diastolic loading condition, resulting displacements and resulting von-Mises strain and stresses for an ALL survivor.

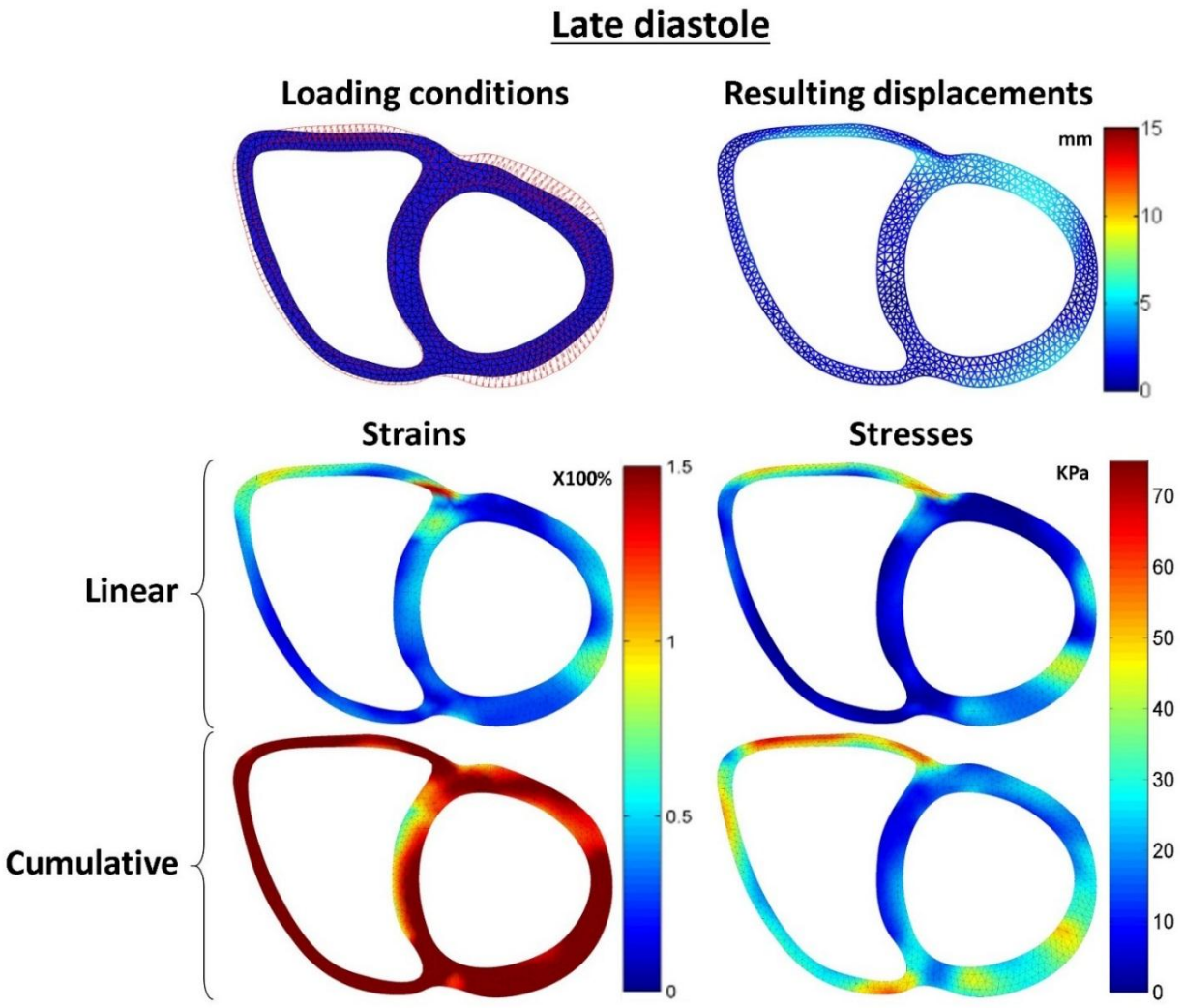

Figure 7.6: Late diastolic loading condition, resulting displacements and resulting von-Mises strain and stresses for the same ALL survivor as in Figure 7.6.

7.4.4 Volunteers groups analysis

ALL survivors had lower cumulative strain and stresses than healthy volunteers during diastolic relaxation, in 2-chamber, 4-chamber and short-axis views (Figure 7.7). Myocardial strain and stresses were slightly higher during early diastole compared to late diastole. During systole, SR and HR groups had also slightly lower cumulative von Mises strain and stresses than healthy volunteers.

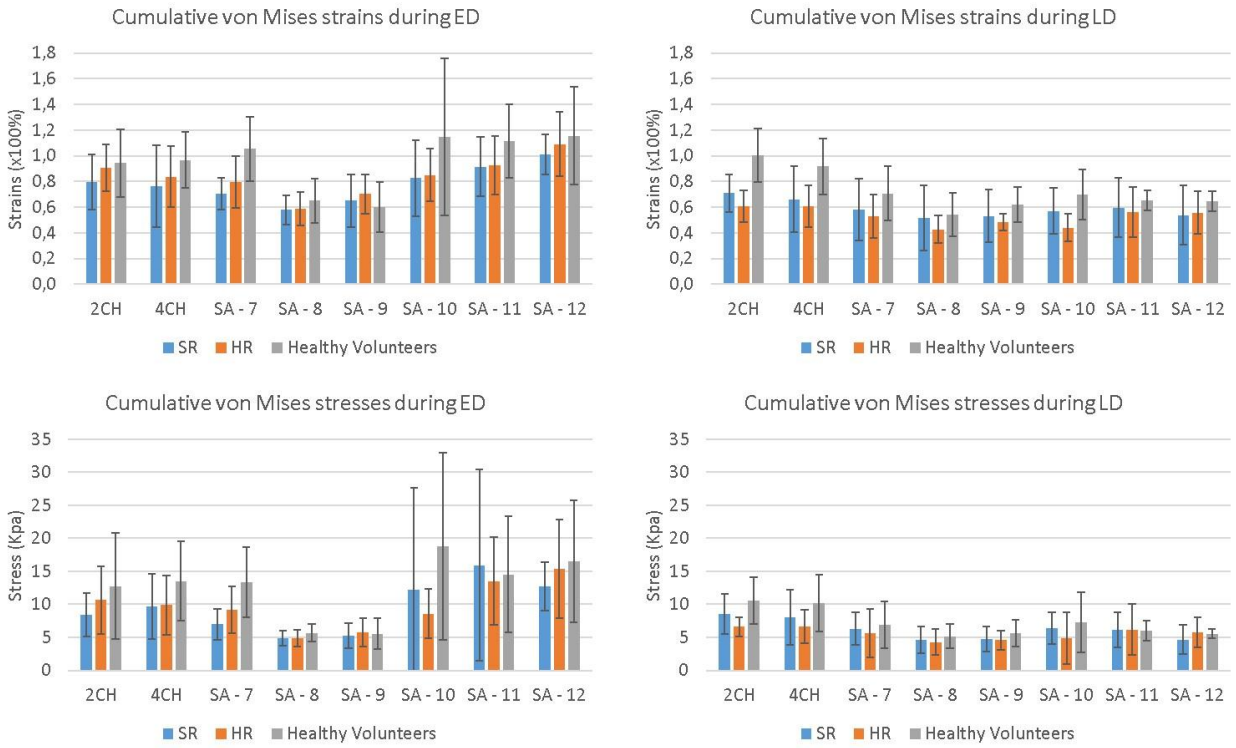

Figure 7.7: Cumulative von Mises strain and stresses comparison between ALL survivors and healthy volunteers, during early and late diastole.

During early diastole, myocardial strain remained similar between the different groups of volunteers (2-chamber: p=0.373, 4-chamber: p=0.176 and short-axis: p=0.127). However, during late diastole, myocardial strain were significantly reduced in SR and HR groups compared to healthy volunteers (71 ± 14% and 61 ± 12% vs. 100 ± 20%, respectively, p<0.001) in 2-chamber view. The same finding was seen in 4-chamber (66 ± 23% and 61 ± 17% vs. 92 ± 21%, respectively, p=0.004) and short-axis (57 ± 22% and 51 ± 16% vs. 68 ± 17%, respectively, p=0.008) views. In short-axis, this reduction was seen over the whole myocardial area rather than specific to some segments.

Myocardial stresses were significantly reduced during early diastole in SR and HR groups compared to healthy volunteers, but only in 4-chamber view (9.69 ± 4.91 kPa and 9.90 ± 4.51 kPa vs. 13.52 ± 6.00 kPa, respectively, p=0.038). During late diastole, myocardial stresses were reduced using both 2-chamber (8.55 ± 2.98 kPa and 6.59 ± 1.50 kPa vs. 10.6 ± 3.6 kPa, p=0.004) and 4-chamber (8.05 ± 4.18 kPa and 6.69 ± 2.53 kPa vs. 10.2 ± 4.3 kPa, p=0.023) views.

7.5 Discussion

The objective of this study, which was to develop a method based on cine-CMR and finite element modeling to evaluate 2D regional myocardial function in childhood ALL survivors, was successfully reached. Myocardial strain generated during late diastole were significantly reduced in ALL survivors compared to healthy volunteers in 4-chambers, 2-chambers and short-axis views, which may suggest a possible reduction in the myocardial relaxation function in ALL survivors. Myocardial stresses were significantly reduced in ALL survivors compared to healthy volunteers only in 4-chambers view. The fact that myocardial stresses remained similar between ALL survivors and healthy volunteers in 2-chambers and short-axis views suggests that myocardial changes may be local rather than generalized over the whole ventricular myocardium.

The use of raw contours may induce a sliding phenomenon along the curves which may result in incorrect strain estimation, especially in terms of shear strain in regions such as the right ventricular wall. Displacements from elastic registration [239] may be accurately estimated if myocardial displacements are small enough, which is not the case for myocardial displacements. Estimating myocardial displacements using skeleton-based technique provided an accurate estimation since it was based on geometry characteristics of the myocardium. Reconstituting contours from the skeleton provided accurate tracking of myocardial wall without sliding phenomenon, especially in short-axis view. However, errors on the estimation of end-points position seem to affect myocardial displacement estimation only in 2-chamber and 4-chamber views contrary to short-axis view where myocardial tracking is mainly based on junction point and seem to be less sensitive to pixelization errors.

XY and von Mises strain and stresses provided complementary information. Von Mises stresses take into account the shear component whereas the XY index does not. However, segmentation errors can generate large shear stresses, which encourages keeping the XY index that neglects such stresses. Shear strain and stresses are affected by errors, especially in regions such as left-right ventricular junctions in short axis. For this reason, these regions should not be included. Even with the use of calibrated contours, left-right ventricular junctions may result in important estimation errors.

Two routes were possible to estimate myocardial strain and stresses: linear- and cumulative-based estimation. Linear-based estimation is the most appropriate method to approximate the resulting

strain and stresses for a given myocardial displacement because it does not include transitory strain and stresses due to non-linear displacement of the myocardium. Moreover, the linear estimation technique is more realistic because the hyperelasticity is taken into account as the apparent Young Modulus is directly estimated for the given deformation. However cumulative-based estimation of strain and stresses may be more appropriate for large displacements as it allows mesh restructuration at each phase. Strain and stresses errors due to large displacements may affect both linear- and cumulative-based techniques, especially during late diastole, i.e., rapid filling phases. One workaround is to estimate strain and stresses iteratively by dividing displacements into multiple steps while applying a mesh restructuration at each step.

During the cardiac cycle, the myocardium experiences two types of deformations: an active contraction where myocardial fibers are stimulated to contract, and a passive relaxation where myocardial fibers relax. During early diastole, the myocardium is under a passive relaxation with a small component of active tension where ventricular pressure is constant while ventricular volumes increase due to blood inflow. During late diastole, the myocardium is mostly under passive relaxation, but with a slight increase in ventricular pressure and volumes due to auricular contraction. Finite-element analysis may be appropriate to the simulation of the late diastole only. In this case, from a mechanical point of view, ventricular pressure may be considered as loading conditions while myocardial deformation as resulting output [63]. We chose a different approach to be able to simulate both systole and diastole using myocardial displacements estimated from cine-CMR images as loading conditions.

The myocardium tends to follow an anisotropic mechanical behavior. However, during an experimental equal biaxial loading, the elasticity modulus tends to be isotropic [73]. Moreover, through the thickness of the myocardial wall, the presence of multiple fiber directions has been reported [279]. The combination of the three main directions of fibers, i.e., circular, oblique and helical, further justify our hypothesis of an isotropic model. Taking into account the anisotropic or possibly orthotropic behavior of the myocardium using MR-based diffusion tensor imaging will require important time to acquire volunteers' data, segment the images, fit the models and implement such data.

Both tissue Doppler-based strain imaging and speckle tracking echocardiography has been used to detect anthracycline cardiotoxicity. An important decrease of myocardial radial strain was reported

in rats who received moderate doses of doxorubicin [35, 280]. In humans, in both adults and children, systolic myocardial deformation was reduced with a significant decrease in both radial, circumferential and longitudinal strain after low-dose anthracycline treatment [281, 186, 282-286]. However, none of these studies have investigated myocardial strain during diastolic relaxation. To the best of our knowledge, our study is the first to use cine MRI to estimate 2D myocardial strain during both systole and diastole. Moreover, our finding for strain during systolic contraction is similar to these studies.

Three main limitations were encountered during this study. First, the technique presented in this paper did not take into account the through-plane motion of the myocardium [268]. In order to estimate the real stains and stresses that the myocardium undergoes during a specific cardiac cycle, advanced techniques that correct for the 3-dimensional through-plane motion [273, 287] would have to be used. For that reason, the presented strain and stresses should not be taken as real values of myocardial strain and stresses, but rather as indices used for the purpose of qualitative comparison between volunteers. Secondly, strain and stresses errors may be cumulated due to segmentation errors when using cumulative estimation techniques. However, by slightly smoothing the temporal displacement of myocardial contours through the cardiac cycle, these segmentation errors can be reduced significantly. Finally, meshing myocardial area required several steps to make sure the quality of the mesh was suitable for myocardial displacement. Although, phase-to-phase displacement may keep deformations small, comparing two distant phases with large myocardial deformations can result in wrong strain and stresses estimation, especially if the meshing size is small. During mesh optimization, we tried to keep the mesh size as homogenous as possible within the myocardial area along with an optimal angle size (~60°), while keeping at least two triangles within the myocardial wall thickness.

7.6 Conclusion

Our new skeleton-based technique provided robust results and accurate tracking of myocardial tissue for further quantification of apparent strain and mechanical stresses. Cumulative-based estimation of strain and stresses allows mesh restructuration at each phase and thus, is more appropriate for large displacements. The apparent strain and stresses were significantly lower in doxorubicin-treated ALL survivors, which may indicate a reduction in myocardial contractile and relaxation function. Taking into account the non-linear myocardial displacements through this

cumulative-based estimation of strain and stresses help in detecting any alterations in myocardial tissue properties.

Acknowledgment

This work was financially supported by the Cole Foundation, the NSERC (Discovery grant and CREATE-MEDITIS Program), the FRQNT (team grant) and the CIHR (team grant).

The authors would also like to thank Tarik Afyane for the acquisition of MRI data and technical assistance provided during the study.

CHAPTER 8 GENERAL DISCUSSION

The four objectives that were originally set were all met. First, we reviewed the different cardiotoxicities induced by doxorubicin. Second, we evaluated MRI T1 and T2 relaxation times sensitivity to detect myocardial damage. Third, we proposed a quantitative method for extracting and tracking 2D myocardial displacement using clinical cine MRI. Finally, we developed and proposed a finite-element model of the myocardium to evaluate mechanical properties changes within the myocardium. To answer to the two questions that were initially raised, myocardial tissue alterations appear to happen at a sub-clinical level, since the cardiac function remained normal in most of the cancer survivors included in this study. There cardiomyopathies affect both the morphology and the function part of the heart. Whether these alterations will progress toward a more damaging cardiomyopathies remain an open question.

The combined use of multi-parametric MRI (T1 and T2 relaxation times), clinical indices (fractional shortening, wall thickening, ejection fraction and apex rotation), displacement patterns (displacements and deformation) and biomechanical parameters (resulting von Mises and principal strains and stresses) provided a better understanding of doxorubicin-induced cardiotoxicity. Especially as the studies were conducted using the same cohort of cancer survivors and healthy volunteers, the proposed techniques helped us in determining which index may have the highest predictive power to detect subclinical myocardial damage that is susceptible to progress toward clinical significance.

The use of pre-gadolinium T1 relaxation times showed that there were local myocardial changes affecting some segments of the myocardium but not the whole myocardium in cancer survivors. The fact that HR group had higher pre-gadolinium T1 relaxation times compared to healthy volunteers may suggest a reduced systolic function or the presence of oedema or protein deposition in the myocardium. On the other hand, post-gadolinium T1 showed a significant decrease in HR group compared to SR group, which may also suggest that the HR group may have an abnormal perfusion function. This finding was further confirmed by a higher partition coefficient in HR group compared to HV group and also between SR group compared to HV group. Similarly, T2 relaxation times were significantly higher in the high risk group of cancer survivors compared to the standard risk group. This increase may indicate alterations in the myocardial tissue at this stage. However, whether such changes will progress towards a clinical level or not remain to be verified.

The use of myocardial displacement patterns as a biomarker to predict doxorubicin-induced cardiotoxicity is promising, especially as myocardial contractile function seems to be affected in doxorubicin-treated cancer survivors. Two main limitations were encountered during this study. The first one being due to segmentation errors. Segmentation errors cannot be eliminated but could be reduced significantly by segmenting only relative displacements from one phase to another. Thus, instead of segmenting each phase blindly, contours should be transposed to the next phase and optimized relatively to the previous phase, which should result in a refined segmentation, with enhanced reproducibility and reduced segmentation time. Moreover, during segmentation, we had to take into account the signal mean within the myocardial region and use a consistent color-scale to efficiently segment the myocardium. Varying the color-scale could result in either a thinner or thicker myocardial wall, which could alter indices estimation such as thickening fraction. The second limitation is related to pixelation effects when extracting myocardial skeleton curves. Several curve smoothing steps were required since skeleton curves were calculated in pixelated manner. To project skeleton curves on myocardial contours, we previously used an algorithm that detect proximal points. This technique did not work since it required strong smoothing to avoid projection lines crossing each other's. Moreover, due to myocardial wall contraction during the systolic stage, the algorithm resulted in errors near RV-LV junctions when trying to project skeletons into myocardial contours. Unfortunately, this problem persisted even when using perpendicular projections of the skeleton onto myocardial contours. Thus, we had to limit segments extremities and exclude RV-LV junctions.

Finally, the use of strain and stress indices seems the most susceptible to detect doxorubicin-induced cardiotoxicity. Reduction in strains and stresses during the cardiac cycle (see Appendix B) was see in doxorubicin-treated cancer survivors which may indicate a reduction in myocardial contractile function. Though, three main limitations were encountered during strains and stresses estimation. The first one reside in the segmentation process and whether to include or not papillary muscles and others structure. This limitation remains an important factor that may have a significant effect on the results. The second limitation is related to the choice of constitutive law. The proposed model consists of an isotropic hyperplastic model of myocardial mechanical behavior. While a better model would take into account the anisotropic behavior of the myocardium. This limitation should persist unless myocardial fibers orientation is known. We believe that the use of simulated fibers orientation should considerably enhance the finite-element

model. Finally, the last limitation is related to the through-plane motion, which was not taken into account. Because of such omission, the resulting strains and stresses should not be used for quantitative purposes. The use of a 3D model may be required to take into account such third-dimensional motion.

To answer to the two questions raised earlier, we can say that several cardiomyopathies are induced by doxorubicin. These cardiomyopathies affect not only the myocardial contractile function, but also the tissue composition of the myocardium. The fact that cancer survivors, especially the HR group, had slightly higher pre-gadolinium T1 relaxation times compared to healthy volunteers may suggest reduced systolic function or the presence of oedema or protein deposition. Furthermore, the partition coefficient which is insensitive to post-enhancement duration was significantly elevated in cancer survivors (both SR and HR group) compared to HV group, which may suggest the presence of a reduced perfusion function. The higher T2 values in HR group compared to SR group suggest that the fat and water contents of the myocardium may altered in this group of cancer survivors. On the other hand, the fact that myocardial displacement patterns along with left-ventricular apex rotation were significantly lower in cancer survivors compared to healthy volunteers suggest that the myocardial contractile function is definitely reduced in our cohort of cancer survivors. Similarly, the apparent strains and stresses were also significantly lower in cancer survivors compared to healthy volunteers, which should further confirm the presence of a reduced myocardial contractile function.

The second question which asks whether these doxorubicin-induced cardiomyopathies alter the myocardial function or not, we can say that most of alterations that affect the cardiac function remained subclinical. Thickening fraction remained similar between cancer survivors and healthy volunteers in all planes. Left ventricular ejection fraction was significantly reduced in cancer survivors compared to healthy volunteers when estimating it using 2-chamber or 4-chamber view. However, when using conventional short-axis view, the index failed to detect any significant differences between both SR and HR groups or between cancer survivors and healthy volunteers. On the other hand, diastolic fraction in 4-chamber view was lower in cancer survivors as compared to healthy volunteer, but only for the right ventricle. Left ventricular diastolic fraction in 4-chamber view was similar between cancer survivors and healthy volunteers. Similarly, LV diastolic fraction was similar between cancer survivors and healthy volunteers in 2-chamber and short-axis views. Conversely, cancer survivors had significant lower rotation angles compared to healthy volunteers.

Furthermore, SR group had slightly lower rotation angle than HR group, which may again suggest that the contractile function of the myocardium may be altered.

One common limitation to our study is related to the fact that our cohort of cancer survivors and healthy volunteers was relatively small. To further confirm the clinical application of our results, a study with a larger cohort of cancer survivors and healthy volunteers will be required, especially as the cohort of cancer survivors was further divided into SR and HR group. Another limitation to our models is related to the time required to segment patients' images. In this study, we choose the semi-automatic segmentation, which requires considerable time to segments patients' images. The reason behind this choice is because semi-automatic segmentation is often more accurate compared to automatic segmentation. Also, in order to segment a short-axis slice, which include 25 images, the required time is approximately 20 to 30 minutes, which is significant. However, we proposed an interpolation-based segmentation, which should reduce segmentation time significantly. To segment one slice of 25 images, segmentation time may be reduced to up to 2 minutes by including contours interpolation during the segmentation process. Finally, the last limitation is related to the choice of our cohort of cancer survivors and the cumulative doxorubicin doses received during the treatment. Most of cancer survivors received moderate doxorubicin-doses. Furthermore, most of cancer survivors have also received dexrazoxane as a cardioprotective agent, which may have inhibited doxorubicin-related cardiotoxicity.

CHAPTER 9 CONCLUSION AND RECOMMENDATIONS

To conclude, the presented techniques for detecting doxorubicin-induced cardiotoxicity are all promising. Most of myocardial injuries reported in this doctoral project remained at a subclinical level. Whether these changes will progress toward a more damaging cardiac injury such as late congestive heart failure remain an open question. We believe that all of the presented indices may have a say in detecting doxorubicin-induced cardiotoxicity.

This work is presented as a preliminary model for the detection of doxorubicin-induced cardiotoxicity. However, several improvements can be made to the presented techniques. The first improvement resides in the segmentation process. Segmentation process is considered the main source of errors when tracking myocardial displacements. Moreover, semi-automated segmentation is time consuming and may in this case not allow clinical application. Segmenting one slice takes between 30 to 60 seconds while segmenting the whole cardiac cycle, i.e., 30 slices, may take up to 30 minutes, depending on the user's ability to segment myocardial contours. However, with the use of slice interpolation (see Appendix A) one may reduce segmentation time to up to 2 minutes for the whole cardiac cycle. Moreover, with the use of smoothing and elastic registration (Appendix B and C), one may further reduce segmentation times. This reduction in time is important because segmenting of multiple heart may take considerable time.

The second improvement resides in the fine-element model (Appendix D). Currently, mechanical strains and stresses are obtained from myocardial displacements used as loading conditions (Appendix E and F). A hyperelastic model with an isotropic distribution of Young's Modulus was used. However, the heart follows an anisotropic behaviour. In this case, an improved model would include an orthotropic or possibly an anisotropic Young's Modulus in order to estimate strains and stresses.

The last improvement will be considering a more complex 3D model of the heart (Appendix G). Such model would take into account the through-plane motion and will benefit strains and stresses estimation. Currently 2D strains and stress are proposed only as a preliminary model because the through-plane motion was omitted. However, in order to estimate the actual strains and stresses that the myocardium undergoes during a specific interval of the cardiac cycle, one would have to include the through-plane motion. Finally, we propose a segmentation software developed under MatLab interface. This software facilitates the whole segmentation process by allowing semi-

automated segmentation (Appendix H). The use of template is proposed to reduce segmentation times. Manually segmenting a slice which includes 30 images would take approximately 30 minutes. However, by the use of templates and Bezier curves, we could reduce such segmentation to approximately 5 minutes.

This work should serve as building stage for a more complex 3D model of the human heart. A compromise however needs to be made between processing time and complexity of the model. We believe that with the use of a more complex 3D model, many of the previously discussed limitation should be solved in an easier manner. The inclusion of the through-plane motion would enhance significantly out estimation of myocardial displacements along with indices such as mechanical strains and stresses.

Finally, for the medium and long term, this project contributes to the advancement of knowledge in the field of doxorubicin-induced cardiomyopathies, myocardial tracking and multiparametric analysis of the myocardium. A graphical interface was designed in close collaboration with cardiologists, for myocardial segmentation, 3D visualization of myocardial contours and automatic processing of myocardial contours to extract T1 and T2 relaxation times, myocardial displacements patters and myocardial mechanical strains and stresses. The integration of this software tool at the clinical level is a first concrete step towards a more comprehensive management of doxorubicin-induced cardiomyopathies.

BIBLIOGRAPHY

1. Treat LH, McDannold N, Vykhodtseva N, Zhang Y, Tam K, Hynynen K. Targeted delivery of doxorubicin to the rat brain at therapeutic levels using MRI-guided focused ultrasound. International journal of cancer Journal international du cancer. 2007;121(4):901-7. doi:10.1002/ijc.22732.

2. Singal PK, Iliskovic N. Doxorubicin-induced cardiomyopathy. N Engl J Med. 1998;339(13):900-5. doi:10.1056/NEJM199809243391307.

3. Ahmet I, Sawa Y, Iwata K, Matsuda H. Gene transfection of hepatocyte growth factor attenuates cardiac remodeling in the canine heart: A novel gene therapy for cardiomyopathy. J Thorac Cardiovasc Surg. 2002;124(5):957-63.

4. Chatterjee K, Zhang J, Honbo N, Karliner JS. Doxorubicin cardiomyopathy. Cardiology. 2010;115(2):155-62. doi:10.1159/000265166.

5. Lefrak EA, Pitha J, Rosenheim S, Gottlieb JA. A clinicopathologic analysis of adriamycin cardiotoxicity. Cancer. 1973;32(2):302-14.

6. Koiwa Y, Kamada H, Shirato K, Saitoh Y, Kanai H, editors. Importance of regional myocardial layer function by phased tracking method in doxorubicin cardiomyopathy. Ultrasonics Symposium, 1999. Proceedings. 1999 IEEE; 1999 1999.

7. Koiwa Y, Kanai H, Hasegawa H, Saitoh Y, Shirato K. Left ventricular transmural systolic function by high-sensitivity velocity measurement "phased-tracking method" across the septum in doxorubicin cardiomyopathy. Ultrasound Med Biol. 2002;28(11-12):1395-403.

8. Hequet O, Le QH, Moullet I, Pauli E, Salles G, Espinouse D et al. Subclinical late cardiomyopathy after doxorubicin therapy for lymphoma in adults. J Clin Oncol. 2004;22(10):1864-71. doi:10.1200/JCO.2004.06.033.

9. Tallaj JA, Franco V, Rayburn BK, Pinderski L, Benza RL, Pamboukian S et al. Response of doxorubicin-induced cardiomyopathy to the current management strategy of heart failure. The Journal of heart and lung transplantation : the official publication of the International Society for Heart Transplantation. 2005;24(12):2196-201. doi:10.1016/j.healun.2004.12.108.

10. Katamadze NA, Lartsuliani KP, Kiknadze MP. Left ventricular function in patients with toxic cardiomyopathy and with idiopathic dilated cardiomyopathy treated with Doxorubicin. Georgian medical news. 2009(166):43-8.

11. Myers CE, McGuire WP, Liss RH, Ifrim I, Grotzinger K, Young RC. Adriamycin: the role of lipid peroxidation in cardiac toxicity and tumor response. Science. 1977;197(4299):165-7.

12. Mimnaugh EG, Gram TE, Trush MA. Stimulation of mouse heart and liver microsomal lipid peroxidation by anthracycline anticancer drugs: characterization and effects of reactive oxygen scavengers. J Pharmacol Exp Ther. 1983;226(3):806-16.

13. Li T, Singal PK. Adriamycin-induced early changes in myocardial antioxidant enzymes and their modulation by probucol. Circulation. 2000;102(17):2105-10.

14. Berthiaume JM, Wallace KB. Adriamycin-induced oxidative mitochondrial cardiotoxicity. Cell biology and toxicology. 2007;23(1):15-25. doi:10.1007/s10565-006-0140-y.

15. Green PS, Leeuwenburgh C. Mitochondrial dysfunction is an early indicator of doxorubicin-induced apoptosis. Biochim Biophys Acta. 2002;1588(1):94-101.

16. Danz ED, Skramsted J, Henry N, Bennett JA, Keller RS. Resveratrol prevents doxorubicin cardiotoxicity through mitochondrial stabilization and the Sirt1 pathway. Free radical biology & medicine. 2009;46(12):1589-97. doi:10.1016/j.freeradbiomed.2009.03.011.

17. Kluza J, Marchetti P, Gallego MA, Lancel S, Fournier C, Loyens A et al. Mitochondrial proliferation during apoptosis induced by anticancer agents: effects of doxorubicin and mitoxantrone on cancer and cardiac cells. Oncogene. 2004;23(42):7018-30. doi:10.1038/sj.onc.1207936.

18. Zhu SG, Kukreja RC, Das A, Chen Q, Lesnefsky EJ, Xi L. Dietary nitrate supplementation protects against Doxorubicin-induced cardiomyopathy by improving mitochondrial function. J Am Coll Cardiol. 2011;57(21):2181-9. doi:10.1016/j.jacc.2011.01.024.

19. Arai M, Tomaru K, Takizawa T, Sekiguchi K, Yokoyama T, Suzuki T et al. Sarcoplasmic reticulum genes are selectively down-regulated in cardiomyopathy produced by doxorubicin in rabbits. Journal of molecular and cellular cardiology. 1998;30(2):243-54. doi:10.1006/jmcc.1997.0588.

20. Shadle SE, Bammel BP, Cusack BJ, Knighton RA, Olson SJ, Mushlin PS et al. Daunorubicin cardiotoxicity: evidence for the importance of the quinone moiety in a free-radical-independent mechanism. Biochemical pharmacology. 2000;60(10):1435-44.

21. Zhou S, Starkov A, Froberg MK, Leino RL, Wallace KB. Cumulative and irreversible cardiac mitochondrial dysfunction induced by doxorubicin. Cancer Res. 2001;61(2):771-7.

22. Kwok JC, Richardson DR. Unexpected anthracycline-mediated alterations in iron-regulatory protein-RNA-binding activity: the iron and copper complexes of anthracyclines decrease RNA-binding activity. Molecular pharmacology. 2002;62(4):888-900.

23. Kwok JC, Richardson DR. Anthracyclines induce accumulation of iron in ferritin in myocardial and neoplastic cells: inhibition of the ferritin iron mobilization pathway. Molecular pharmacology. 2003;63(4):849-61.

24. Saad SY, Najjar TA, Al-Rikabi AC. The preventive role of deferoxamine against acute doxorubicin-induced cardiac, renal and hepatic toxicity in rats. Pharmacological research : the official journal of the Italian Pharmacological Society. 2001;43(3):211-8. doi:10.1006/phrs.2000.0769.

25. Wang S, Konorev EA, Kotamraju S, Joseph J, Kalivendi S, Kalyanaraman B. Doxorubicin induces apoptosis in normal and tumor cells via distinctly different mechanisms. intermediacy of H(2)O(2)- and p53-dependent pathways. J Biol Chem. 2004;279(24):25535-43. doi:10.1074/jbc.M400944200.

26. Eom YW, Kim MA, Park SS, Goo MJ, Kwon HJ, Sohn S et al. Two distinct modes of cell death induced by doxorubicin: apoptosis and cell death through mitotic catastrophe accompanied by senescence-like phenotype. Oncogene. 2005;24(30):4765-77. doi:10.1038/sj.onc.1208627.

27. Dartsch DC, Schaefer A, Boldt S, Kolch W, Marquardt H. Comparison of anthracycline-induced death of human leukemia cells: programmed cell death versus necrosis. Apoptosis : an international journal on programmed cell death. 2002;7(6):537-48.

28. Isner JM, Ferrans VJ, Cohen SR, Witkind BG, Virmani R, Gottdiener JS et al. Clinical and morphologic cardiac findings after anthracycline chemotherapy. Analysis of 64 patients studied at necropsy. The American journal of cardiology. 1983;51(7):1167-74.

29. Arola OJ, Saraste A, Pulkki K, Kallajoki M, Parvinen M, Voipio-Pulkki LM. Acute doxorubicin cardiotoxicity involves cardiomyocyte apoptosis. Cancer Res. 2000;60(7):1789-92.

30. Cigremis Y, Parlakpinar H, Polat A, Colak C, Ozturk F, Sahna E et al. Beneficial role of aminoguanidine on acute cardiomyopathy related to doxorubicin-treatment. Molecular and cellular biochemistry. 2006;285(1-2):149-54. doi:10.1007/s11010-005-9072-8.

31. Von Hoff DD, Layard MW, Basa P, Davis HL, Jr., Von Hoff AL, Rozencweig M et al. Risk factors for doxorubicin-induced congestive heart failure. Ann Intern Med. 1979;91(5):710-7.

32. Druck MN, Gulenchyn KY, Evans WK, Gotlieb A, Srigley JR, Bar-Shlomo BZ et al. Radionuclide angiography and endomyocardial biopsy in the assessment of doxorubicin cardiotoxicity. Cancer. 1984;53(8):1667-74.

33. Steinherz LJ, Steinherz PG, Tan CT, Heller G, Murphy ML. Cardiac toxicity 4 to 20 years after completing anthracycline therapy. JAMA : the journal of the American Medical Association. 1991;266(12):1672-7.

34. Ali MK, Ewer MS, Gibbs HR, Swafford J, Graff KL. Late doxorubicin-associated cardiotoxicity in children. The possible role of intercurrent viral infection. Cancer. 1994;74(1):182-8.

35. Migrino RQ, Aggarwal D, Konorev E, Brahmbhatt T, Bright M, Kalyanaraman B. Early detection of doxorubicin cardiomyopathy using two-dimensional strain echocardiography. Ultrasound Med Biol. 2008;34(2):208-14. doi:10.1016/j.ultrasmedbio.2007.07.018.

36. Ewer MS, Lippman SM. Type II chemotherapy-related cardiac dysfunction: time to recognize a new entity. J Clin Oncol. 2005;23(13):2900-2. doi:10.1200/JCO.2005.05.827.

37. Hydock DS, Lien CY, Jensen BT, Schneider CM, Hayward R. Exercise preconditioning provides long-term protection against early chronic doxorubicin cardiotoxicity. Integrative cancer therapies. 2011;10(1):47-57. doi:10.1177/1534735410392577.

38. Aissiou M, Périé D, Cheriet F, Dahdah NS, Laverdière C, Curnier D. Imaging of early modification in cardiomyopathy: the doxorubicin-induced model. The international journal of cardiovascular imaging. 2013;29(7):1459-76.

39. Minotti G, Menna P, Salvatorelli E, Cairo G, Gianni L. Anthracyclines: molecular advances and pharmacologic developments in antitumor activity and cardiotoxicity. Pharmacological reviews. 2004;56(2):185-229. doi:10.1124/pr.56.2.6.

40. Bu'Lock FA, Mott MG, Oakhill A, Martin RP. Left ventricular diastolic function after anthracycline chemotherapy in childhood: relation with systolic function, symptoms, and pathophysiology. British heart journal. 1995;73(4):340-50.

41. Lipshultz SE, Colan SD, Gelber RD, Perez-Atayde AR, Sallan SE, Sanders SP. Late cardiac effects of doxorubicin therapy for acute lymphoblastic leukemia in childhood. New England Journal of Medicine. 1991;324(12):808-15.

42. Torti FM, Bristow MM, Lum BL, Carter SK, Howes AE, Aston DA et al. Cardiotoxicity of epirubicin and doxorubicin: assessment by endomyocardial biopsy. Cancer Research. 1986;46(7):3722-7.

43. Ludke AR, Al-Shudiefat AA, Dhingra S, Jassal DS, Singal PK. A concise description of cardioprotective strategies in doxorubicin-induced cardiotoxicity. Canadian journal of physiology and pharmacology. 2009;87(10):756-63. doi:10.1139/Y09-059.

44. Shankar SM, Marina N, Hudson MM, Hodgson DC, Adams MJ, Landier W et al. Monitoring for cardiovascular disease in survivors of childhood cancer: report from the Cardiovascular Disease Task Force of the Children's Oncology Group. Pediatrics. 2008;121(2):e387-96. doi:10.1542/peds.2007-0575.

45. Hauser M, Gibson BS, Wilson N. Diagnosis of anthracycline-induced late cardiomyopathy by exercise-spiroergometry and stress-echocardiography. European journal of pediatrics. 2001;160(10):607-10.

46. Wassmuth R, Lentzsch S, Erdbruegger U, Schulz-Menger J, Doerken B, Dietz R et al. Subclinical cardiotoxic effects of anthracyclines as assessed by magnetic resonance imaging-a pilot study. American heart journal. 2001;141(6):1007-13. doi:10.1067/mhj.2001.115436.

47. Monaghan MJ. Role of real time 3D echocardiography in evaluating the left ventricle. Heart. 2006;92(1):131-6.

48. Klingensmith ME. The Washington manual of surgery. Lippincott Williams & Wilkins; 2008.

49. Netter FH. Atlas of human anatomy. Elsevier Health Sciences; 2010.

50. Klabunde R. Cardiovascular physiology concepts. Lippincott Williams & Wilkins; 2011.

51. Guyton A, Hall J. Textbook of medical physiology, 11th. 2006.

52. Stanisz GJ, Odrobina EE, Pun J, Escaravage M, Graham SJ, Bronskill MJ et al. T1, T2 relaxation and magnetization transfer in tissue at 3T. Magn Reson Med. 2005;54(3):507-12. doi:10.1002/mrm.20605.

53. Hundley WG, Bluemke DA, Finn JP, Flamm SD, Fogel MA, Friedrich MG et al. ACCF/ACR/AHA/NASCI/SCMR 2010 expert consensus document on cardiovascular magnetic resonance: a report of the American College of Cardiology Foundation Task Force on Expert Consensus Documents. J Am Coll Cardiol. 2010;55(23):2614-62. doi:10.1016/j.jacc.2009.11.011.

54. Giri S, Chung Y-C, Merchant A, Mihai G, Rajagopalan S, Raman SV et al. T2 quantification for improved detection of myocardial edema. Journal of cardiovascular magnetic resonance. 2009;11:56.

55. Anderson LJ, Holden S, Davis B, Prescott E, Charrier CC, Bunce NH et al. Cardiovascular T2-star (T2*) magnetic resonance for the early diagnosis of myocardial iron overload. European heart journal. 2001;22(23):2171-9.

56. Weber OM, Speier P, Scheffler K, Bieri O. Assessment of magnetization transfer effects in myocardial tissue using balanced steady-state free precession (bSSFP) cine MRI. Magn Reson Med. 2009;62(3):699-705. doi:10.1002/mrm.22053.

57. Niederer SA, Plank G, Chinchapatnam P, Ginks M, Lamata P, Rhode KS et al. Length-dependent tension in the failing heart and the efficacy of cardiac resynchronization therapy. Cardiovascular research. 2011;89(2):336-43. doi:10.1093/cvr/cvq318.

58. Chapelle D, Fernández M, Gerbeau JF, Moireau P, Sainte-Marie J, Zemzemi N. Numerical simulation of the electromechanical activity of the heart. Functional Imaging and Modeling of the Heart. 2009:357-65.

59. Zhukov L, Barr AH, editors. Heart-muscle fiber reconstruction from diffusion tensor MRI. Visualization, 2003. VIS 2003. IEEE; 2003 24-24 Oct. 2003.

60. Sosnovik DE, Garanger E, Aikawa E, Nahrendorf M, Figuiredo JL, Dai G et al. Molecular MRI of cardiomyocyte apoptosis with simultaneous delayed-enhancement MRI distinguishes apoptotic and necrotic myocytes in vivo: potential for midmyocardial salvage in acute ischemia. Circulation Cardiovascular imaging. 2009;2(6):460-7. doi:10.1161/CIRCIMAGING.109.859678.

61. Sermesant M, Chabiniok R, Chinchapatnam P, Mansi T, Billet F, Moireau P et al. Patient-specific electromechanical models of the heart for the prediction of pacing acute effects in CRT: a preliminary clinical validation. Medical image analysis. 2012;16(1):201-15. doi:10.1016/j.media.2011.07.003.

62. Peters J, Ecabert O, Schmitt H, Grass M, Weese J. Local cardiac wall motion estimation from retrospectively gated ct images. Functional Imaging and Modeling of the Heart. 2009:191-200.

63. Wang V, Hoogendoorn C, Engelbrecht G, Frangi A, Young A, Hunter P et al., editors. Unsupervised segmentation and personalised FE modelling of in vivo human myocardial mechanics based on an MRI atlas. Biomedical Imaging (ISBI), 2012 9th IEEE International Symposium on; 2012: IEEE.

64. Oertel H, Krittian S. Modelling the human cardiac fluid mechanics. KIT Scientific Publishing; 2012.

65. Chabiniok R, Moireau P, Lesault PF, Rahmouni A, Deux JF, Chapelle D. Estimation of tissue contractility from cardiac cine-MRI using a biomechanical heart model. Biomechanics and modeling in mechanobiology. 2012;11(5):609-30.

66. Wang H, Amini AA. Cardiac Motion and Deformation Recovery From MRI: A Review. Medical Imaging, IEEE Transactions on. 2012;31(2):487-503.

67. Aguado-Sierra J, Krishnamurthy A, Villongco C, Chuang J, Howard E, Gonzales MJ et al. Patient-specific modeling of dyssynchronous heart failure: a case study. Progress in biophysics and molecular biology. 2011;107(1):147-55.

68. Mao H, Wang L, Wong KC, Liu H, Shi P. Volumetric modeling electromechanics of the heart. Statistical Atlases and Computational Models of the Heart. Imaging and Modelling Challenges. Springer; 2012. p. 224-33.

69. Nash MP, Panfilov AV. Electromechanical model of excitable tissue to study reentrant cardiac arrhythmias. Progress in biophysics and molecular biology. 2004;85(2):501-22.

70. Hoffmeister BK, Handley SM, Wickline SA, Miller JG. Ultrasonic determination of the anisotropy of Young's modulus of fixed tendon and fixed myocardium. The Journal of the Acoustical Society of America. 1996;100(6):3933-40.

71. Shi P, Liu H. Stochastic finite element framework for simultaneous estimation of cardiac kinematic functions and material parameters. Medical image analysis. 2003;7(4):445-64.

72. Ghaemi H, Behdinan K, Spence AD. In vitro technique in estimation of passive mechanical properties of bovine heart: Part I. Experimental techniques and data. Medical engineering & physics. 2009;31(1):76-82. doi:http://dx.doi.org/10.1016/j.medengphy.2008.04.008.

73. Ghaemi H, Behdinan K, Spence A. In vitro technique in estimation of passive mechanical properties of bovine heart: Part II. Constitutive relation and finite element analysis. Medical engineering & physics. 2009;31(1):83-91.

74. Wang B, Tedder ME, Perez CE, Wang G, de Jongh Curry AL, To F et al. Structural and biomechanical characterizations of porcine myocardial extracellular matrix. Journal of Materials Science: Materials in Medicine. 2012:1-13.

75. Von Hoff DD, Rozencweig M, Piccart M. The cardiotoxicity of anticancer agents. Semin Oncol. 1982;9(1):23-33.

76. Allen A. The cardiotoxicity of chemotherapeutic drugs. Semin Oncol. 1992;19(5):529-42.

77. Eksborg S, Palm C, Bjork O. A comparative pharmacokinetic study of doxorubicin and 4'-epi-doxorubicin in children with acute lymphocytic leukemia using a limited sampling procedure. Anti-cancer drugs. 2000;11(2):129-36.

78. Wojtacki J, Lewicka-Nowak E, Lesniewski-Kmak K. Anthracycline-induced cardiotoxicity: clinical course, risk factors, pathogenesis, detection and prevention--review of the literature. Medical science monitor : international medical journal of experimental and clinical research. 2000;6(2):411-20.

79. Lipshultz SE, Lipsitz SR, Sallan SE, Dalton VM, Mone SM, Gelber RD et al. Chronic progressive cardiac dysfunction years after doxorubicin therapy for childhood acute lymphoblastic leukemia. J Clin Oncol. 2005;23(12):2629-36. doi:10.1200/JCO.2005.12.121.

80. Vaniscotte A, Pleydell D, Raoul F, Quere JP, Jiamin Q, Wang Q et al. Modelling and spatial discrimination of small mammal assemblages: an example from western Sichuan (China). Ecological modelling. 2009;220(9-10):1218-31. doi:10.1016/j.ecolmodel.2009.02.019.

81. Wang H, Laughton CA. Evaluation of molecular modelling methods to predict the sequence-selectivity of DNA minor groove binding ligands. Physical chemistry chemical physics : PCCP. 2009;11(45):10722-8. doi:10.1039/b911702d.

82. He Y, Zeng ZY, Zhong GQ, Li JY, Li WK, Li W. [Mitochondrial connexin43 and postconditioning protection in rabbits underwent myocardial ischemia/reperfusion injury]. Zhonghua xin xue guan bing za zhi. 2010;38(4):357-62.

83. Gao J, Zhong MK, Fan ZD, Yuan N, Zhou YB, Zhang F et al. SOD1 overexpression in paraventricular nucleus improves post-infarct myocardial remodeling and ventricular function. Pflugers Archiv : European journal of physiology. 2012;463(2):297-307. doi:10.1007/s00424-011-1036-0.

84. Hannan EL, Zhong Y, Jacobs AK, Holmes DR, Walford G, Venditti FJ et al. Effect of onset-to-door time and door-to-balloon time on mortality in patients undergoing percutaneous coronary interventions for st-segment elevation myocardial infarction. The American journal of cardiology. 2010;106(2):143-7. doi:10.1016/j.amjcard.2010.02.029.

85. Zhong JJ, Lin ZJ, Gao QG, Liu WP, Dan QH, Cai HP et al. [(99)Tc(m)-MIBI exercise stress single photon emission computed tomography myocardial perfusion imaging of patients with myocardial bridge]. Zhonghua xin xue guan bing za zhi. 2010;38(2):156-9.

86. Martins RM, Fonseca RH, Duarte MM, Reuters VS, Ferreira MM, Almeida C et al. Impact of subclinical hypothyroidism treatment in systolic and diastolic cardiac function. Arquivos brasileiros de endocrinologia e metabologia. 2011;55(7):460-7.

87. Childs H, Ma L, Ma M, Clarke J, Cocker M, Green J et al. Comparison of long and short axis quantification of left ventricular volume parameters by cardiovascular magnetic resonance, with ex-vivo validation. Journal of cardiovascular magnetic resonance : official journal of the Society for Cardiovascular Magnetic Resonance. 2011;13:40. doi:10.1186/1532-429X-13-40.

88. Panjrath GS, Jain D. Monitoring chemotherapy-induced cardiotoxicity: role of cardiac nuclear imaging. Journal of nuclear cardiology : official publication of the American Society of Nuclear Cardiology. 2006;13(3):415-26. doi:10.1016/j.nuclcard.2006.03.002.

89. Lipshultz SE, Colan SD, Gelber RD, Perez-Atayde AR, Sallan SE, Sanders SP. Late cardiac effects of doxorubicin therapy for acute lymphoblastic leukemia in childhood. The New England journal of medicine. 1991;324(12):808-15. doi:10.1056/NEJM199103213241205.

90. Adams MJ, Lipshultz SE. Pathophysiology of anthracycline- and radiation-associated cardiomyopathies: implications for screening and prevention. Pediatr Blood Cancer. 2005;44(7):600-6. doi:10.1002/pbc.20352.

91. Olson RD, Gambliel HA, Vestal RE, Shadle SE, Charlier HA, Jr., Cusack BJ. Doxorubicin cardiac dysfunction: effects on calcium regulatory proteins, sarcoplasmic reticulum, and triiodothyronine. Cardiovascular toxicology. 2005;5(3):269-83.

92. Vandecruys E, Mondelaers V, De Wolf D, Benoit Y, Suys B. Late cardiotoxicity after low dose of anthracycline therapy for acute lymphoblastic leukemia in childhood. Journal of cancer survivorship : research and practice. 2012;6(1):95-101. doi:10.1007/s11764-011-0186-6.

93. Elbl L, Hrstkova H, Chaloupka V. The late consequences of anthracycline treatment on left ventricular function after treatment for childhood cancer. European journal of pediatrics. 2003;162(10):690-6. doi:10.1007/s00431-003-1275-y.

94. Giantris A, Abdurrahman L, Hinkle A, Asselin B, Lipshultz SE. Anthracycline-induced cardiotoxicity in children and young adults. Critical reviews in oncology/hematology. 1998;27(1):53-68.

95. Ito T, Fujio Y, Takahashi K, Azuma J. Degradation of NFAT5, a transcriptional regulator of osmotic stress-related genes, is a critical event for doxorubicin-induced cytotoxicity in cardiac myocytes. J Biol Chem. 2007;282(2):1152-60. doi:10.1074/jbc.M609547200.

96. Zhang J, Clark JR, Jr., Herman EH, Ferrans VJ. Doxorubicin-induced apoptosis in spontaneously hypertensive rats: differential effects in heart, kidney and intestine, and

inhibition by ICRF-187. Journal of molecular and cellular cardiology. 1996;28(9):1931-43. doi:10.1006/jmcc.1996.0186.

97. Gilleron M, Marechal X, Montaigne D, Franczak J, Neviere R, Lancel S. NADPH oxidases participate to doxorubicin-induced cardiac myocyte apoptosis. Biochemical and biophysical research communications. 2009;388(4):727-31. doi:10.1016/j.bbrc.2009.08.085.

98. L'Ecuyer T, Sanjeev S, Thomas R, Novak R, Das L, Campbell W et al. DNA damage is an early event in doxorubicin-induced cardiac myocyte death. Am J Physiol Heart Circ Physiol. 2006;291(3):H1273-80. doi:10.1152/ajpheart.00738.2005.

99. Pacher P, Liaudet L, Bai P, Mabley JG, Kaminski PM, Virag L et al. Potent metalloporphyrin peroxynitrite decomposition catalyst protects against the development of doxorubicin-induced cardiac dysfunction. Circulation. 2003;107(6):896-904.

100. Ahmed HH, Mannaa F, Elmegeed GA, Doss SH. Cardioprotective activity of melatonin and its novel synthesized derivatives on doxorubicin-induced cardiotoxicity. Bioorganic & medicinal chemistry. 2005;13(5):1847-57. doi:10.1016/j.bmc.2004.10.066.

101. Naidu MU, Kumar KV, Mohan IK, Sundaram C, Singh S. Protective effect of Gingko biloba extract against doxorubicin-induced cardiotoxicity in mice. Indian journal of experimental biology. 2002;40(8):894-900.

102. Janero DR. Malondialdehyde and thiobarbituric acid-reactivity as diagnostic indices of lipid peroxidation and peroxidative tissue injury. Free radical biology & medicine. 1990;9(6):515-40.

103. Takemura G, Fujiwara H. Doxorubicin-induced cardiomyopathy from the cardiotoxic mechanisms to management. Progress in cardiovascular diseases. 2007;49(5):330-52. doi:10.1016/j.pcad.2006.10.002.

104. Davies KJ, Doroshow JH. Redox cycling of anthracyclines by cardiac mitochondria. I. Anthracycline radical formation by NADH dehydrogenase. J Biol Chem. 1986;261(7):3060-7.

105. Berlin V, Haseltine WA. Reduction of adriamycin to a semiquinone-free radical by NADPH cytochrome P-450 reductase produces DNA cleavage in a reaction mediated by molecular oxygen. J Biol Chem. 1981;256(10):4747-56.

106. Bachur NR, Gordon SL, Gee MV, Kon H. NADPH cytochrome P-450 reductase activation of quinone anticancer agents to free radicals. Proc Natl Acad Sci U S A. 1979;76(2):954-7.

107. Chandran K, Aggarwal D, Migrino RQ, Joseph J, McAllister D, Konorev EA et al. Doxorubicin inactivates myocardial cytochrome c oxidase in rats: cardioprotection by Mito-Q. Biophys J. 2009;96(4):1388-98. doi:10.1016/j.bpj.2008.10.042.

108. Kalyanaraman B, Joseph J, Kalivendi S, Wang S, Konorev E, Kotamraju S. Doxorubicin-induced apoptosis: implications in cardiotoxicity. Molecular and cellular biochemistry. 2002;234-235(1-2):119-24.

109. Wang S, Kotamraju S, Konorev E, Kalivendi S, Joseph J, Kalyanaraman B. Activation of nuclear factor-kappaB during doxorubicin-induced apoptosis in endothelial cells and myocytes is pro-apoptotic: the role of hydrogen peroxide. The Biochemical journal. 2002;367(Pt 3):729-40. doi:10.1042/BJ20020752.

110. Tsang WP, Chau SP, Kong SK, Fung KP, Kwok TT. Reactive oxygen species mediate doxorubicin induced p53-independent apoptosis. Life sciences. 2003;73(16):2047-58.

111. Pentassuglia L, Graf M, Lane H, Kuramochi Y, Cote G, Timolati F et al. Inhibition of ErbB2 by receptor tyrosine kinase inhibitors causes myofibrillar structural damage without cell death in adult rat cardiomyocytes. Experimental cell research. 2009;315(7):1302-12. doi:10.1016/j.yexcr.2009.02.001.

112. Holmberg SR, Williams AJ. Patterns of interaction between anthraquinone drugs and the calcium-release channel from cardiac sarcoplasmic reticulum. Circ Res. 1990;67(2):272-83.

113. Dodd DA, Atkinson JB, Olson RD, Buck S, Cusack BJ, Fleischer S et al. Doxorubicin cardiomyopathy is associated with a decrease in calcium release channel of the sarcoplasmic reticulum in a chronic rabbit model. The Journal of clinical investigation. 1993;91(4):1697-705. doi:10.1172/JCI116379.

114. DeAtley SM, Aksenov MY, Aksenova MV, Harris B, Hadley R, Cole Harper P et al. Antioxidants protect against reactive oxygen species associated with adriamycin-treated cardiomyocytes. Cancer letters. 1999;136(1):41-6.

115. Bers DM. Calcium cycling and signaling in cardiac myocytes. Annual review of physiology. 2008;70:23-49. doi:10.1146/annurev.physiol.70.113006.100455.

116. Octavia Y, Tocchetti CG, Gabrielson KL, Janssens S, Crijns HJ, Moens AL. Doxorubicin-induced cardiomyopathy: from molecular mechanisms to therapeutic strategies. Journal of molecular and cellular cardiology. 2012;52(6):1213-25. doi:10.1016/j.yjmcc.2012.03.006.

117. Olson RD, Li X, Palade P, Shadle SE, Mushlin PS, Gambliel HA et al. Sarcoplasmic reticulum calcium release is stimulated and inhibited by daunorubicin and daunorubicinol. Toxicology and applied pharmacology. 2000;169(2):168-76. doi:10.1006/taap.2000.9065.

118. Torti FM, Bristow MM, Lum BL, Carter SK, Howes AE, Aston DA et al. Cardiotoxicity of epirubicin and doxorubicin: assessment by endomyocardial biopsy. Cancer research. 1986;46(7):3722-7.

119. Billingham ME, Mason JW, Bristow MR, Daniels JR. Anthracycline cardiomyopathy monitored by morphologic changes. Cancer Treat Rep. 1978;62(6):865-72.

120. Bristow MR, Sageman WS, Scott RH, Billingham ME, Bowden RE, Kernoff RS et al. Acute and chronic cardiovascular effects of doxorubicin in the dog: the cardiovascular pharmacology of drug-induced histamine release. Journal of cardiovascular pharmacology. 1980;2(5):487-515.

121. Lipshultz SE, Scully RE, Lipsitz SR, Sallan SE, Silverman LB, Miller TL et al. Assessment of dexrazoxane as a cardioprotectant in doxorubicin-treated children with high-risk acute lymphoblastic leukaemia: long-term follow-up of a prospective, randomised, multicentre trial. The lancet oncology. 2010;11(10):950-61. doi:10.1016/S1470-2045(10)70204-7.

122. Jensen BV, Skovsgaard T, Nielsen SL. Functional monitoring of anthracycline cardiotoxicity: a prospective, blinded, long-term observational study of outcome in 120 patients. Annals of oncology : official journal of the European Society for Medical Oncology / ESMO. 2002;13(5):699-709.

123. Albini A, Pennesi G, Donatelli F, Cammarota R, De Flora S, Noonan DM. Cardiotoxicity of anticancer drugs: the need for cardio-oncology and cardio-oncological prevention. J Natl Cancer Inst. 2010;102(1):14-25. doi:10.1093/jnci/djp440.

124. Lang RM, Bierig M, Devereux RB, Flachskampf FA, Foster E, Pellikka PA et al. Recommendations for chamber quantification: a report from the American Society of Echocardiography's Guidelines and Standards Committee and the Chamber Quantification Writing Group, developed in conjunction with the European Association of Echocardiography, a branch of the European Society of Cardiology. Journal of the American Society of Echocardiography : official publication of the American Society of Echocardiography. 2005;18(12):1440-63. doi:10.1016/j.echo.2005.10.005.

125. Steinherz LJ, Wexler LH. The prevention of anthracycline cardiomyopathy. Progress in Pediatric Cardiology. 1998;8(3):97-108. doi:10.1016/s1058-9813(98)00006-x.

126. Armstrong GT, Plana JC, Zhang N, Srivastava D, Green DM, Ness KK et al. Screening adult survivors of childhood cancer for cardiomyopathy: comparison of echocardiography and cardiac magnetic resonance imaging. J Clin Oncol. 2012;30(23):2876-84. doi:10.1200/JCO.2011.40.3584.

127. Khoo NS, Young A, Occleshaw C, Cowan B, Zeng IS, Gentles TL. Assessments of right ventricular volume and function using three-dimensional echocardiography in older children and adults with congenital heart disease: comparison with cardiac magnetic resonance imaging. Journal of the American Society of Echocardiography : official publication of the American Society of Echocardiography. 2009;22(11):1279-88. doi:10.1016/j.echo.2009.08.011.

128. Piegari E, Di Salvo G, Castaldi B, Vitelli MR, Rodolico G, Golino P et al. Myocardial strain analysis in a doxorubicin-induced cardiomyopathy model. Ultrasound Med Biol. 2008;34(3):370-8. doi:10.1016/j.ultrasmedbio.2007.08.002.

129. Tassan-Mangina S, Codorean D, Metivier M, Costa B, Himberlin C, Jouannaud C et al. Tissue Doppler imaging and conventional echocardiography after anthracycline treatment in adults: early and late alterations of left ventricular function during a prospective study. European journal of echocardiography : the journal of the Working Group on Echocardiography of the European Society of Cardiology. 2006;7(2):141-6. doi:10.1016/j.euje.2005.04.009.

130. Mavinkurve-Groothuis AM, Weijers G, Groot-Loonen J, Pourier M, Feuth T, de Korte CL et al. Interobserver, intraobserver and intrapatient reliability scores of myocardial strain imaging with 2-d echocardiography in patients treated with anthracyclines. Ultrasound Med Biol. 2009;35(4):697-704. doi:10.1016/j.ultrasmedbio.2008.09.026.

131. Watts RG, George M, Johnson WH, Jr. Pretreatment and routine echocardiogram monitoring during chemotherapy for anthracycline-induced cardiotoxicity rarely identifies significant cardiac dysfunction or alters treatment decisions: a 5-year review at a single pediatric oncology center. Cancer. 2012;118(7):1919-24. doi:10.1002/cncr.26481.

132. Avelar T, Pauliks LB, Freiberg AS. Clinical impact of the baseline echocardiogram in children with high-risk acute lymphoblastic leukemia. Pediatr Blood Cancer. 2011;57(2):227-30. doi:10.1002/pbc.23066.

133. Cottin Y, L'Huillier I, Casasnovas O, Geoffroy C, Caillot D, Zeller M et al. Dobutamine stress echocardiography identifies anthracycline cardiotoxicity. European journal of echocardiography : the journal of the Working Group on Echocardiography of the European Society of Cardiology. 2000;1(3):180-3. doi:10.1053/euje.2000.0037.

134. Weesner KM, Bledsoe M, Chauvenet A, Wofford M. Exercise echocardiography in the detection of anthracycline cardiotoxicity. Cancer. 1991;68(2):435-8.

135. Smibert E, Carlin JB, Vidmar S, Wilkinson LC, Newton M, Weintraub RG. Exercise echocardiography reflects cumulative anthracycline exposure during childhood. Pediatr Blood Cancer. 2004;42(7):556-62. doi:10.1002/pbc.20016.

136. Hamada H, Ohkubo T, Maeda M, Ogawa S. Evaluation of cardiac reserved function by high-dose dobutamine-stress echocardiography in asymptomatic anthracycline-treated survivors of childhood cancer. Pediatrics international : official journal of the Japan Pediatric Society. 2006;48(3):313-20. doi:10.1111/j.1442-200X.2006.02210.x.

137. De Wolf D, Suys B, Maurus R, Benoit Y, Verhaaren H, Matthijs D et al. Dobutamine stress echocardiography in the evaluation of late anthracycline cardiotoxicity in childhood cancer survivors. Pediatric research. 1996;39(3):504-12. doi:10.1203/00006450-199603000-00020.

138. Tei C, Ling LH, Hodge DO, Bailey KR, Oh JK, Rodeheffer RJ et al. New index of combined systolic and diastolic myocardial performance: a simple and reproducible measure of cardiac function--a study in normals and dilated cardiomyopathy. Journal of cardiology. 1995;26(6):357-66.

139. Lakoumentas JA, Panou FK, Kotseroglou VK, Aggeli KI, Harbis PK. The Tei index of myocardial performance: applications in cardiology. Hellenic journal of cardiology : HJC = Hellenike kardiologike epitheorese. 2005;46(1):52-8.

140. Ishii M, Tsutsumi T, Himeno W, Eto G, Furui J, Hashino K et al. Sequential evaluation of left ventricular myocardial performance in children after anthracycline therapy. The American journal of cardiology. 2000;86(11):1279-81, A9.

141. Sato T, Harada K, Tamura M, Watanabe A, Ishii M, Takada G. Cardiorespiratory exercise capacity and its relation to a new Doppler index in children previously treated with anthracycline. Journal of the American Society of Echocardiography : official publication of the American Society of Echocardiography. 2001;14(4):256-63.

142. Senju N, Ikeda S, Koga S, Miyahara Y, Tsukasaki K, Tomonaga M et al. The echocardiographic Tei-index reflects early myocardial damage induced by anthracyclines in patients with hematological malignancies. Heart and vessels. 2007;22(6):393-7. doi:10.1007/s00380-007-0985-x.

143. Bicudo LS, Tsutsui JM, Shiozaki A, Rochitte CE, Arteaga E, Mady C et al. Value of real time three-dimensional echocardiography in patients with hypertrophic cardiomyopathy: comparison with two-dimensional echocardiography and magnetic resonance imaging. Echocardiography. 2008;25(7):717-26. doi:10.1111/j.1540-8175.2008.00684.x.

144. Hung J, Lang R, Flachskampf F, Shernan SK, McCulloch ML, Adams DB et al. 3D echocardiography: a review of the current status and future directions. Journal of the American Society of Echocardiography : official publication of the American Society of Echocardiography. 2007;20(3):213-33. doi:10.1016/j.echo.2007.01.010.

145. Mulvagh SL, DeMaria AN, Feinstein SB, Burns PN, Kaul S, Miller JG et al. Contrast echocardiography: current and future applications. Journal of the American Society of Echocardiography : official publication of the American Society of Echocardiography. 2000;13(4):331-42.

146. Eitel I, von Knobelsdorff-Brenkenhoff F, Bernhardt P, Carbone I, Muellerleile K, Aldrovandi A et al. Clinical characteristics and cardiovascular magnetic resonance findings in stress (takotsubo) cardiomyopathy. JAMA : the journal of the American Medical Association. 2011;306(3):277-86. doi:10.1001/jama.2011.992.

147. Jurcut R, Wildiers H, Ganame J, D'Hooge J, Paridaens R, Voigt JU. Detection and monitoring of cardiotoxicity-what does modern cardiology offer? Supportive care in cancer : official journal of the Multinational Association of Supportive Care in Cancer. 2008;16(5):437-45. doi:10.1007/s00520-007-0397-6.

148. Hundley WG, Bluemke DA, Finn JP, Flamm SD, Fogel MA, Friedrich MG et al. ACCF/ACR/AHA/NASCI/SCMR 2010 expert consensus document on cardiovascular magnetic resonance: a report of the American College of Cardiology Foundation Task Force on Expert Consensus Documents. Circulation. 2010;121(22):2462-508. doi:10.1161/CIR.0b013e3181d44a8f.

149. Francone M, Carbone I, Agati L, Bucciarelli Ducci C, Mangia M, Iacucci I et al. Utility of T2-weighted short-tau inversion recovery (STIR) sequences in cardiac MRI: an overview of clinical applications in ischaemic and non-ischaemic heart disease. Radiol Med. 2011;116(1):32-46. doi:10.1007/s11547-010-0594-0.

150. Positano V, Pingitore A, Giorgetti A, Favilli B, Santarelli MF, Landini L et al. A fast and effective method to assess myocardial necrosis by means of contrast magnetic resonance imaging. Journal of cardiovascular magnetic resonance : official journal of the Society for Cardiovascular Magnetic Resonance. 2005;7(2):487-94.

151. Wang VY, Lam HI, Ennis DB, Cowan BR, Young AA, Nash MP. Modelling passive diastolic mechanics with quantitative MRI of cardiac structure and function. Medical image analysis. 2009;13(5):773-84. doi:10.1016/j.media.2009.07.006.

152. Fonseca CG, Backhaus M, Bluemke DA, Britten RD, Chung JD, Cowan BR et al. The Cardiac Atlas Project--an imaging database for computational modeling and statistical atlases of the heart. Bioinformatics. 2011;27(16):2288-95. doi:10.1093/bioinformatics/btr360.

153. Young AA, Frangi AF. Computational cardiac atlases: from patient to population and back. Experimental physiology. 2009;94(5):578-96. doi:10.1113/expphysiol.2008.044081.

154. Zhong X, Spottiswoode BS, Meyer CH, Kramer CM, Epstein FH. Imaging three-dimensional myocardial mechanics using navigator-gated volumetric spiral cine DENSE MRI. Magn Reson Med. 2010;64(4):1089-97. doi:10.1002/mrm.22503.

155. Nagueh SF, Appleton CP, Gillebert TC, Marino PN, Oh JK, Smiseth OA et al. Recommendations for the evaluation of left ventricular diastolic function by echocardiography. European journal of echocardiography : the journal of the Working Group on Echocardiography of the European Society of Cardiology. 2009;10(2):165-93. doi:10.1093/ejechocard/jep007.

156. Senior R, Becher H, Monaghan M, Agati L, Zamorano J, Vanoverschelde JL et al. Contrast echocardiography: evidence-based recommendations by European Association of Echocardiography. European journal of echocardiography : the journal of the Working Group on Echocardiography of the European Society of Cardiology. 2009;10(2):194-212. doi:10.1093/ejechocard/jep005.

157. Périé D, Dahdah N, Foudis A, Curnier D. Multi-parametric MRI as an indirect evaluation tool of the mechanical properties of cardiac tissues. BMC Cardiovascular Disorders. 2013;Submitted.

158. Grenier R, Périé D, Gilbert G, Beaudoin G, Curnier D. Assessment of Mechanical Properties of Muscles from Multi-Parametric Magnetic Resonance Imaging. Medical Engineering and Physics. 2013;Submitted.

159. Bistoquet A, Oshinski J, Škrinjar O. Myocardial deformation recovery from cine MRI using a nearly incompressible biventricular model. Medical image analysis. 2008;12(1):69-85.

160. Niederer SA, Plank G, Chinchapatnam P, Ginks M, Lamata P, Rhode KS et al. Length-dependent tension in the failing heart and the efficacy of cardiac resynchronization therapy. Cardiovascular research. 2011;89(2):336-43.

161. Chabiniok R, Moireau P, Lesault P-F, Rahmouni A, Deux J-F, Chapelle D. Estimation of tissue contractility from cardiac cine-MRI using a biomechanical heart model. Biomechanics and modeling in mechanobiology. 2012;11(5):609-30.

162. Chapelle D, Fernández MA, Gerbeau J-F, Moireau P, Sainte-Marie J, Zemzemi N. Numerical simulation of the electromechanical activity of the heart. Functional Imaging and Modeling of the Heart. Springer; 2009. p. 357-65.

163. Aguado-Sierra J, Krishnamurthy A, Villongco C, Chuang J, Howard E, Gonzales MJ et al. Patient-specific modeling of dyssynchronous heart failure: a case study. Progress in biophysics and molecular biology. 2011;107(1):147-55.

164. Sermesant M, Chabiniok R, Chinchapatnam P, Mansi T, Billet F, Moireau P et al. Patient-specific electromechanical models of the heart for the prediction of pacing acute effects in CRT: a preliminary clinical validation. Medical image analysis. 2012;16(1):201-15.

165. Iles L, Pfluger H, Phrommintikul A, Cherayath J, Aksit P, Gupta SN et al. Evaluation of diffuse myocardial fibrosis in heart failure with cardiac magnetic resonance contrast-enhanced T1 mapping. J Am Coll Cardiol. 2008;52(19):1574-80. doi:10.1016/j.jacc.2008.06.049.

166. Mewton N, Liu CY, Croisille P, Bluemke D, Lima JA. Assessment of myocardial fibrosis with cardiovascular magnetic resonance. J Am Coll Cardiol. 2011;57(8):891-903. doi:10.1016/j.jacc.2010.11.013.

167. Messroghli DR, Niendorf T, Schulz-Menger J, Dietz R, Friedrich MG. T1 Mapping in Patients with Acute Myocardial Infarction: MYOCARDIAL INFARCTION AND SCAR. Journal of Cardiovascular Magnetic Resonance. 2003;5(2):353-9.

168. Messroghli DR, Walters K, Plein S, Sparrow P, Friedrich MG, Ridgway JP et al. Myocardial T1 mapping: application to patients with acute and chronic myocardial infarction. Magnetic Resonance in Medicine. 2007;58(1):34-40.

169. Giri S, Chung YC, Merchant A, Mihai G, Rajagopalan S, Raman SV et al. T2 quantification for improved detection of myocardial edema. Journal of cardiovascular magnetic resonance : official journal of the Society for Cardiovascular Magnetic Resonance. 2009;11:56. doi:10.1186/1532-429X-11-56.

170. Sparrow P, Amirabadi A, Sussman MS, Paul N, Merchant N. Quantitative assessment of myocardial T2 relaxation times in cardiac amyloidosis. Journal of Magnetic Resonance Imaging. 2009;30(5):942-6.

171. Wood JC, Otto-Duessel M, Aguilar M, Nick H, Nelson MD, Coates TD et al. Cardiac iron determines cardiac T2*, T2, and T1 in the gerbil model of iron cardiomyopathy. Circulation. 2005;112(4):535-43. doi:10.1161/CIRCULATIONAHA.104.504415.

172. Kondur AK, Li T, Vaitkevicius P, Afonso L. Quantification of myocardial iron overload by cardiovascular magnetic resonance imaging T2* and review of the literature. Clinical cardiology. 2009;32(6):E55-9. doi:10.1002/clc.20310.

173. Atanasijevic T, Shusteff M, Fam P, Jasanoff A. Calcium-sensitive MRI contrast agents based on superparamagnetic iron oxide nanoparticles and calmodulin. Proc Natl Acad Sci U S A. 2006;103(40):14707-12. doi:10.1073/pnas.0606749103.

174. Kim YJ, Choi BW, Hur J, Lee HJ, Seo JS, Kim TH et al. Delayed enhancement in hypertrophic cardiomyopathy: comparison with myocardial tagging MRI. J Magn Reson Imaging. 2008;27(5):1054-60. doi:10.1002/jmri.21366.

175. Teraoka K, Hirano M, Ookubo H, Sasaki K, Katsuyama H, Amino M et al. Delayed contrast enhancement of MRI in hypertrophic cardiomyopathy. Magn Reson Imaging. 2004;22(2):155-61. doi:10.1016/j.mri.2003.08.009.

176. Tandri H, Saranathan M, Rodriguez ER, Martinez C, Bomma C, Nasir K et al. Noninvasive detection of myocardial fibrosis in arrhythmogenic right ventricular cardiomyopathy using delayed-enhancement magnetic resonance imaging. J Am Coll Cardiol. 2005;45(1):98-103. doi:10.1016/j.jacc.2004.09.053.

177. Perel RD, Slaughter RE, Strugnell WE. Subendocardial late gadolinium enhancement in two patients with anthracycline cardiotoxicity following treatment for Ewing's sarcoma. Journal of cardiovascular magnetic resonance : official journal of the Society for Cardiovascular Magnetic Resonance. 2006;8(6):789-91. doi:10.1080/10976640600737664.

178. Skjold A, Amundsen BH, Wiseth R, Stoylen A, Haraldseth O, Larsson HB et al. Manganese dipyridoxyl-diphosphate (MnDPDP) as a viability marker in patients with myocardial infarction. J Magn Reson Imaging. 2007;26(3):720-7. doi:10.1002/jmri.21065.

179. Hu TC, Pautler RG, MacGowan GA, Koretsky AP. Manganese-enhanced MRI of mouse heart during changes in inotropy. Magn Reson Med. 2001;46(5):884-90.

180. Nordhoy W, Anthonsen HW, Bruvold M, Jynge P, Krane J, Brurok H. Manganese ions as intracellular contrast agents: proton relaxation and calcium interactions in rat myocardium. NMR Biomed. 2003;16(2):82-95. doi:10.1002/nbm.817.

181. Waghorn B, Edwards T, Yang Y, Chuang KH, Yanasak N, Hu TC. Monitoring dynamic alterations in calcium homeostasis by T (1)-weighted and T (1)-mapping cardiac manganese-

enhanced MRI in a murine myocardial infarction model. NMR Biomed. 2008;21(10):1102-11. doi:10.1002/nbm.1287.

182. Bers DM. Calcium fluxes involved in control of cardiac myocyte contraction. Circ Res. 2000;87(4):275-81.

183. Holloway CJ, Suttie J, Dass S, Neubauer S. Clinical cardiac magnetic resonance spectroscopy. Progress in cardiovascular diseases. 2011;54(3):320-7. doi:10.1016/j.pcad.2011.08.002.

184. Junjing Z, Yan Z, Baolu Z. Scavenging effects of dexrazoxane on free radicals. Journal of clinical biochemistry and nutrition. 2010;47(3):238.

185. Aissiou M, Perie D, Cheriet F, Dahdah NS, Laverdiere C, Curnier D. Imaging of early modification in cardiomyopathy: the doxorubicin-induced model. The international journal of cardiovascular imaging. 2013. doi:10.1007/s10554-013-0248-0.

186. Sawaya H, Sebag IA, Plana JC, Januzzi JL, Ky B, Cohen V et al. Early detection and prediction of cardiotoxicity in chemotherapy-treated patients. The American journal of cardiology. 2011;107(9):1375-80.

187. Verhaert D, Thavendiranathan P, Giri S, Mihai G, Rajagopalan S, Simonetti OP et al. Direct T2 quantification of myocardial edema in acute ischemic injury. JACC: Cardiovascular Imaging. 2011;4(3):269-78.

188. Ferreira VM, Piechnik SK, Dall'Armellina E, Karamitsos TD, Francis JM, Choudhury RP et al. Non-contrast T1-mapping detects acute myocardial edema with high diagnostic accuracy: a comparison to T2-weighted cardiovascular magnetic resonance. Journal of cardiovascular magnetic resonance : official journal of the Society for Cardiovascular Magnetic Resonance. 2012;14(1):42.

189. Lightfoot JC, D'Agostino RB, Hamilton CA, Jordan J, Torti FM, Kock ND et al. Novel approach to early detection of doxorubicin cardiotoxicity by gadolinium-enhanced cardiovascular magnetic resonance imaging in an experimental model. Circulation: Cardiovascular Imaging. 2010;3(5):550-8.

190. Jiji RS, Kramer CM, Salerno M. Non-invasive imaging and monitoring cardiotoxicity of cancer therapeutic drugs. Journal of Nuclear Cardiology. 2012;19(2):377-88.

191. Tham EB, Haykowsky MJ, Chow K, Spavor M, Kaneko S, Khoo NS et al. Diffuse myocardial fibrosis by T1-mapping in children with subclinical anthracycline cardiotoxicity: relationship to exercise capacity, cumulative dose and remodeling. Journal of cardiovascular magnetic resonance : official journal of the Society for Cardiovascular Magnetic Resonance. 2013;15:48.

192. Krajinovic M, Labuda D, Richer C, Karimi S, Sinnett D. Susceptibility to childhood acute lymphoblastic leukemia: influence of CYP1A1, CYP2D6, GSTM1, and GSTT1 genetic polymorphisms. Blood. 1999;93(5):1496-501.

193. Deichmann R, Haase A. Quantification of T 1 values by SNAPSHOT-FLASH NMR imaging. Journal of Magnetic Resonance (1969). 1992;96(3):608-12.

194. Fetterman M. Anaskel written in Matlab (http://www.mathworks.ca/matlabcentral/fileexchange/25246-anaskel-written-in-matlab), MATLAB Central File Exchange. Retrieved June 13, 2014. 2005().

195. Lam A. Simplified creation of a bullseye (http://www.mathworks.com/matlabcentral/fileexchange/47454-bullseye-plot-zip), MATLAB Central File Exchange. Retrieved February 02, 2016. 2014().

196. Flacke SJ, Fischer SE, Lorenz CH. Measurement of the Gadopentetate Dimeglumine Partition Coefficient in Human Myocardium in Vivo: Normal Distribution and Elevation in Acute and Chronic Infarction 1. Radiology. 2001;218(3):703-10.

197. von Knobelsdorff-Brenkenhoff F, Prothmann M, Dieringer MA, Wassmuth R, Greiser A, Schwenke C et al. Myocardial T1 and T2 mapping at 3 T: reference values, influencing factors and implications. Journal of cardiovascular magnetic resonance : official journal of the Society for Cardiovascular Magnetic Resonance. 2013;15(1):53.

198. Krombach GA, Hahn C, Tomars M, Buecker A, Grawe A, Günther RW et al. Cardiac amyloidosis: MR imaging findings and T1 quantification, comparison with control subjects. Journal of Magnetic Resonance Imaging. 2007;25(6):1283-7.

199. Moon JC, Messroghli DR, Kellman P, Piechnik SK, Robson MD, Ugander M et al. Myocardial T1 mapping and extracellular volume quantification: a Society for Cardiovascular Magnetic Resonance (SCMR) and CMR Working Group of the European Society of Cardiology consensus statement. Journal of cardiovascular magnetic resonance : official journal of the Society for Cardiovascular Magnetic Resonance. 2013;15(1):92.

200. Kellman P, Wilson JR, Xue H, Ugander M, Arai AE. Extracellular volume fraction mapping in the myocardium, part 1: evaluation of an automated method. Journal of cardiovascular magnetic resonance : official journal of the Society for Cardiovascular Magnetic Resonance. 2012;14(1):63.

201. Kellman P, Wilson JR, Xue H, Bandettini WP, Shanbhag SM, Druey KM et al. Extracellular volume fraction mapping in the myocardium, part 2: initial clinical experience. Journal of cardiovascular magnetic resonance : official journal of the Society for Cardiovascular Magnetic Resonance. 2012;14(64):10.1186.

202. Broberg CS, Chugh SS, Conklin C, Sahn DJ, Jerosch-Herold M. Quantification of diffuse myocardial fibrosis and its association with myocardial dysfunction in congenital heart disease. Circulation: Cardiovascular Imaging. 2010;3(6):727-34.

203. Abdel-Aty H, Boyé P, Bock P, Kumar A, Friedrich MG. Stenotic mitral valve prosthesis with left atrial thrombus. Journal of Cardiovascular Magnetic Resonance. 2005;7(2):421-3.

204. Abdel-Aty H, Simonetti O, Friedrich MG. T2-weighted cardiovascular magnetic resonance imaging. Journal of magnetic resonance imaging. 2007;26(3):452-9.

205. Abdel-Aty H, Cocker M, Meek C, Tyberg JV, Friedrich MG. Edema as a very early marker for acute myocardial ischemia: a cardiovascular magnetic resonance study. Journal of the American College of Cardiology. 2009;53(14):1194-201.

206. Arai AE. Using magnetic resonance imaging to characterize recent myocardial injury utility in acute coronary syndrome and other clinical scenarios. Circulation. 2008;118(8):795-6.

207. Butler CR, Thompson R, Haykowsky M, Toma M, Paterson I. Cardiovascular magnetic resonance in the diagnosis of acute heart transplant rejection: a review. Journal of Cardiovascular Magnetic Resonance. 2009;11(1):1-11.

208. Francone M, Bucciarelli-Ducci C, Carbone I, Canali E, Scardala R, Calabrese FA et al. Impact of primary coronary angioplasty delay on myocardial salvage, infarct size, and microvascular damage in patients with ST-segment elevation myocardial infarction: insight from cardiovascular magnetic resonance. Journal of the American College of Cardiology. 2009;54(23):2145-53.

209. Kellman P, Aletras AH, Mancini C, McVeigh ER, Arai AE. T2-prepared SSFP improves diagnostic confidence in edema imaging in acute myocardial infarction compared to turbo spin echo. Magnetic resonance in medicine. 2007;57(5):891-7.

210. Lipshultz SE, Rifai N, Dalton VM, Levy DE, Silverman LB, Lipsitz SR et al. The effect of dexrazoxane on myocardial injury in doxorubicin-treated children with acute lymphoblastic leukemia. New England Journal of Medicine. 2004;351(2):145-53.

211. Lipshultz SE, Miller TL, Scully RE, Lipsitz SR, Rifai N, Silverman LB et al. Changes in cardiac biomarkers during doxorubicin treatment of pediatric patients with high-risk acute lymphoblastic leukemia: associations with long-term echocardiographic outcomes. Journal of Clinical Oncology. 2012;30(10):1042-9.

212. Kremer L, Van der Pal H, Offringa M, Van Dalen E, Voute P. Frequency and risk factors of subclinical cardiotoxicity after anthracycline therapy in children: a systematic review. Annals of Oncology. 2002;13(6):819-29.

213. Moon JC, Treibel TA, Schelbert EB. T1 mapping for diffuse myocardial fibrosis: a key biomarker in cardiac disease? Journal of the American College of Cardiology. 2013;62(14):1288-9.

214. Piechnik SK, Ferreira VM, Lewandowski AJ, Ntusi N, Banerjee R, Holloway C et al. Normal variation of magnetic resonance T1 relaxation times in the human population at 1.5 T using ShMOLLI. Journal of cardiovascular magnetic resonance : official journal of the Society for Cardiovascular Magnetic Resonance. 2013;15(1):13.

215. Aissiou M, Périé D, Gervais J, Trochu F. Development of a progressive dual kriging technique for 2D and 3D multi-parametric MRI data interpolation. Computer Methods in Biomechanics and Biomedical Engineering: Imaging & Visualization. 2013;1(2):69-78. doi:10.1080/21681163.2013.765712.

216. Nysom K, Holm K, Lipsitz SR, Mone SM, Colan SD, Orav EJ et al. Relationship between cumulative anthracycline dose and late cardiotoxicity in childhood acute lymphoblastic leukemia. Journal of Clinical Oncology. 1998;16(2):545-50.

217. Gianni L, Herman EH, Lipshultz SE, Minotti G, Sarvazyan N, Sawyer DB. Anthracycline cardiotoxicity: from bench to bedside. Journal of Clinical Oncology. 2008;26(22):3777-84.

218. Sun JP, Popović ZB, Greenberg NL, Xu X-F, Asher CR, Stewart WJ et al. Noninvasive quantification of regional myocardial function using Doppler-derived velocity, displacement, strain rate, and strain in healthy volunteers: effects of aging. Journal of the American Society of Echocardiography. 2004;17(2):132-8.

219. Oliveira MS, Melo MB, Carvalho JL, Melo IM, Lavor MS, Gomes DA et al. Doxorubicin cardiotoxicity and cardiac function improvement after stem cell therapy diagnosed by strain echocardiography. Journal of cancer science & therapy. 2013;5(2):052.

220. Duchateau N, Sitges M, Doltra A, Fernández-Armenta J, Solanes N, Rigol M et al. Myocardial motion and deformation patterns in an experimental swine model of acute LBBB/CRT and chronic infarct. The international journal of cardiovascular imaging. 2014;30(5):875-87.

221. Mor-Avi V, Lang RM, Badano LP, Belohlavek M, Cardim NM, Derumeaux G et al. Current and evolving echocardiographic techniques for the quantitative evaluation of cardiac mechanics: ASE/EAE consensus statement on methodology and indications: endorsed by the Japanese Society of Echocardiography. Journal of the American Society of Echocardiography. 2011;24(3):277-313.

222. Pan L, Prince JL, Lima JA, Osman NF. Fast tracking of cardiac motion using 3D-HARP. IEEE Trans Biomed Eng. 2005;52(8):1425-35. doi:10.1109/TBME.2005.851490.

223. Spottiswoode BS, Zhong X, Hess AT, Kramer CM, Meintjes EM, Mayosi BM et al. Tracking myocardial motion from cine DENSE images using spatiotemporal phase unwrapping and temporal fitting. IEEE Trans Med Imaging. 2007;26(1):15-30. doi:10.1109/TMI.2006.884215.

224. Hess AT, Zhong X, Spottiswoode BS, Epstein FH, Meintjes EM. Myocardial 3D strain calculation by combining cine displacement encoding with stimulated echoes (DENSE) and cine strain encoding (SENC) imaging. Magn Reson Med. 2009;62(1):77-84. doi:10.1002/mrm.21984.

225. Sampath S, Osman NF, Prince JL. A combined harmonic phase and strain-encoded pulse sequence for measuring three-dimensional strain. Magn Reson Imaging. 2009;27(1):55-61. doi:10.1016/j.mri.2008.05.020.

226. Auger DA, Zhong X, Epstein FH, Spottiswoode BS. Mapping right ventricular myocardial mechanics using 3D cine DENSE cardiovascular magnetic resonance. Journal of cardiovascular magnetic resonance : official journal of the Society for Cardiovascular Magnetic Resonance. 2012;14:4. doi:10.1186/1532-429X-14-4.

227. Rutz AK, Ryf S, Plein S, Boesiger P, Kozerke S. Accelerated whole-heart 3D CSPAMM for myocardial motion quantification. Magn Reson Med. 2008;59(4):755-63. doi:10.1002/mrm.21363.

228. Wang VY, Lam H, Ennis DB, Cowan BR, Young AA, Nash MP. Modelling passive diastolic mechanics with quantitative MRI of cardiac structure and function. Medical image analysis. 2009;13(5):773-84.

229. Lombaert H, Cheriet F, editors. Spatio-temporal segmentation of the heart in 4d mri images using graph cuts with motion cues. Biomedical Imaging: From Nano to Macro, 2010 IEEE International Symposium on; 2010: IEEE.

230. Lu Y, Radau P, Connelly K, Dick A, Wright G. Automatic image-driven segmentation of left ventricle in cardiac cine MRI. The MIDAS Journal. 2009;49:2.

231. Lu Y-L, Connelly KA, Dick AJ, Wright GA, Radau PE. Automatic functional analysis of left ventricle in cardiac cine MRI. Quantitative imaging in medicine and surgery. 2013;3(4):200.

232. Petitjean C, Dacher J-N. A review of segmentation methods in short axis cardiac MR images. Medical image analysis. 2011;15(2):169-84.

233. Suinesiaputra A, Cowan BR, Al-Agamy AO, Elattar MA, Ayache N, Fahmy AS et al. A collaborative resource to build consensus for automated left ventricular segmentation of cardiac MR images. Medical image analysis. 2014;18(1):50-62.

234. Papademetris X, Sinusas AJ, Dione DP, Duncan JS. Estimation of 3D left ventricular deformation from echocardiography. Medical image analysis. 2001;5(1):17-28.

235. Mansi T, Peyrat J-M, Sermesant M, Delingette H, Blanc J, Boudjemline Y et al. Physically-constrained diffeomorphic demons for the estimation of 3D myocardium strain from cine-MRI. Functional Imaging and Modeling of the Heart. Springer; 2009. p. 201-10.

236. Jolly M-P, Guetter C, Guehring J, editors. Cardiac segmentation in MR cine data using inverse consistent deformable registration. Biomedical Imaging: From Nano to Macro, 2010 IEEE International Symposium on; 2010: IEEE.

237. Margeta J, Geremia E, Criminisi A, Ayache N. Layered spatio-temporal forests for left ventricle segmentation from 4D cardiac MRI data. Statistical Atlases and Computational Models of the Heart. Imaging and Modelling Challenges. Springer; 2011. p. 109-19.

238. Fahmy AS, Al-Agamy AO, Khalifa A. Myocardial segmentation using contour-constrained optical flow tracking. Statistical Atlases and Computational Models of the Heart. Imaging and Modelling Challenges. Springer; 2011. p. 120-8.

239. Heyde B, Jasaityte R, Barbosa D, Robesyn V, Bouchez S, Wouters P et al. Elastic image registration versus speckle tracking for 2-d myocardial motion estimation: A direct comparison in vivo. Medical Imaging, IEEE Transactions on. 2013;32(2):449-59.

240. Shi YQ, Sun H. Image and video compression for multimedia engineering: Fundamentals, algorithms, and standards. CRC press; 1999.

241. Ourselin S, Roche A, Prima S, Ayache N, editors. Block matching: A general framework to improve robustness of rigid registration of medical images. Medical Image Computing and Computer-Assisted Intervention–MICCAI 2000; 2000: Springer.

242. Li B, Liu Y, Occleshaw CJ, Cowan BR, Young AA. In-line automated tracking for ventricular function with magnetic resonance imaging. JACC: Cardiovascular Imaging. 2010;3(8):860-6.

243. Bistoquet A, Oshinski J, Skrinjar O. Left ventricular deformation recovery from cine MRI using an incompressible model. Medical Imaging, IEEE Transactions on. 2007;26(9):1136-53.

244. Wenk JF, Ge L, Zhang Z, Soleimani M, Potter DD, Wallace AW et al. A coupled biventricular finite element and lumped-parameter circulatory system model of heart failure. 2012.

245. Silverman LB, Stevenson KE, O'Brien JE, Asselin BL, Barr RD, Clavell L et al. Long-term results of Dana-Farber Cancer Institute ALL Consortium protocols for children with newly diagnosed acute lymphoblastic leukemia (1985–2000). Leukemia. 2010;24(2):320-34.

246. Barry E, DeAngelo DJ, Neuberg D, Stevenson K, Loh ML, Asselin BL et al. Favorable outcome for adolescents with acute lymphoblastic leukemia treated on Dana-Farber Cancer Institute acute lymphoblastic leukemia consortium protocols. Journal of Clinical Oncology. 2007;25(7):813-9.

247. Okayama S, Nakano T, Uemura S, Fujimoto S, Somekawa S, Watanabe M et al. Evaluation of left ventricular diastolic function by fractional area change using cine cardiovascular

magnetic resonance: a feasibility study. Journal of cardiovascular magnetic resonance : official journal of the Society for Cardiovascular Magnetic Resonance. 2013;15:87. doi:10.1186/1532-429X-15-87.

248. Grosgeorge D, Petitjean C, Caudron J, Fares J, Dacher J-N. Automatic cardiac ventricle segmentation in MR images: a validation study. International journal of computer assisted radiology and surgery. 2011;6(5):573-81.

249. Armstrong GT, Joshi VM, Ness KK, Marwick TH, Zhang N, Srivastava D et al. Comprehensive echocardiographic detection of treatment-related cardiac dysfunction in adult survivors of childhood cancer: results from the St. Jude lifetime cohort study. Journal of the American College of Cardiology. 2015;65(23):2511-22.

250. Dietz AC, Sivanandam S, Konety S, Kaufman CL, Gage RM, Kelly AS et al. Evaluation of traditional and novel measures of cardiac function to detect anthracycline-induced cardiotoxicity in survivors of childhood cancer. Journal of Cancer Survivorship. 2014;8(2):183-9.

251. Ylänen K, Poutanen T, Savikurki-Heikkilä P, Rinta-Kiikka I, Eerola A, Vettenranta K. Cardiac magnetic resonance imaging in the evaluation of the late effects of anthracyclines among long-term survivors of childhood cancer. Journal of the American College of Cardiology. 2013;61(14):1539-47.

252. Ylänen K, Poutanen T, Savukoski T, Eerola A, Vettenranta K. Cardiac biomarkers indicate a need for sensitive cardiac imaging among long-term childhood cancer survivors exposed to anthracyclines. Acta Paediatrica. 2015;104(3):313-9.

253. Ylänen K, Eerola A, Vettenranta K, Poutanen T. Three-dimensional echocardiography and cardiac magnetic resonance imaging in the screening of long-term survivors of childhood cancer after cardiotoxic therapy. The American journal of cardiology. 2014;113(11):1886-92.

254. Armenian SH, Gelehrter SK, Vase T, Venkatramani R, Landier W, Wilson KD et al. Screening for cardiac dysfunction in anthracycline-exposed childhood cancer survivors. Clinical Cancer Research. 2014;20(24):6314-23.

255. Meinardi M, Gietema J, Van Der Graaf W, Van Veldhuisen D, Runne M, Sluiter W et al. Cardiovascular morbidity in long-term survivors of metastatic testicular cancer. Journal of Clinical Oncology. 2000;18(8):1725-32.

256. Ho E, Brown A, Barrett P, Morgan RB, King G, Kennedy MJ et al. Subclinical anthracycline- and trastuzumab-induced cardiotoxicity in the long-term follow-up of asymptomatic breast cancer survivors: a speckle tracking echocardiographic study. Heart. 2010;96(9):701-7.

257. Cheung Yf, Li Sn, Chan GC, Wong SJ, Ha Sy. Left ventricular twisting and untwisting motion in childhood cancer survivors. Echocardiography. 2011;28(7):738-45.

258. Sengupta PP, Tajik AJ, Chandrasekaran K, Khandheria BK. Twist mechanics of the left ventricle: principles and application. JACC: Cardiovascular Imaging. 2008;1(3):366-76.

259. Götte MJ, Germans T, Rüssel IK, Zwanenburg JJ, Marcus JT, van Rossum AC et al. Myocardial strain and torsion quantified by cardiovascular magnetic resonance tissue tagging: studies in normal and impaired left ventricular function. Journal of the American College of Cardiology. 2006;48(10):2002-11.

260. Buchalter MB, Weiss JL, Rogers WJ, Zerhouni EA, Weisfeldt ML, Beyar R et al. Noninvasive quantification of left ventricular rotational deformation in normal humans using magnetic resonance imaging myocardial tagging. Circulation. 1990;81(4):1236-44.

261. Dokos S, Smaill BH, Young AA, LeGrice IJ. Shear properties of passive ventricular myocardium. American Journal of Physiology-Heart and Circulatory Physiology. 2002;283(6):H2650-H9.

262. Liu H, Wong LN, Shi P, editors. Cardiac motion and material properties analysis using data confidence weighted extended kalman filter framework. Acoustics, Speech, and Signal Processing, 2003. Proceedings.(ICASSP'03). 2003 IEEE International Conference on; 2003: IEEE.

263. Reisner SA, Lysyansky P, Agmon Y, Mutlak D, Lessick J, Friedman Z. Global longitudinal strain: a novel index of left ventricular systolic function. Journal of the American Society of Echocardiography. 2004;17(6):630-3.

264. Urheim S, Edvardsen T, Torp H, Angelsen B, Smiseth OA. Myocardial strain by Doppler echocardiography validation of a new method to quantify regional myocardial function. Circulation. 2000;102(10):1158-64.

265. Edvardsen T, Gerber BL, Garot J, Bluemke DA, Lima JA, Smiseth OA. Quantitative assessment of intrinsic regional myocardial deformation by Doppler strain rate echocardiography in humans validation against three-dimensional tagged magnetic resonance imaging. Circulation. 2002;106(1):50-6.

266. Mäkelä T, Clarysse P, Sipilä O, Pauna N, Pham QC, Katila T et al. A review of cardiac image registration methods. Medical Imaging, IEEE Transactions on. 2002;21(9):1011-21.

267. Zerhouni EA, Parish DM, Rogers WJ, Yang A, Shapiro EP. Human heart: tagging with MR imaging--a method for noninvasive assessment of myocardial motion. Radiology. 1988;169(1):59-63.

268. Young A, Kraitchman DL, Dougherty L, Axel L. Tracking and finite element analysis of stripe deformation in magnetic resonance tagging. Medical Imaging, IEEE Transactions on. 1995;14(3):413-21.

269. Hillenbrand HB, Lima JA, Bluemke DA, Beache GM, McVeigh ER. Assessment of myocardial systolic function by tagged magnetic resonance imaging. Journal of Cardiovascular Magnetic Resonance. 2000;2(1):57-66.

270. Kybic J, Unser M. Fast parametric elastic image registration. Image Processing, IEEE Transactions on. 2003;12(11):1427-42.

271. Gee J, Sundaram T, Hasegawa I, Uematsu H, Hatabu H. Characterization of regional pulmonary mechanics from serial magnetic resonance imaging data 1. Academic radiology. 2003;10(10):1147-52.

272. Crum WR, Rueckert D, Jenkinson M, Kennedy D, Smith SM. A framework for detailed objective comparison of non-rigid registration algorithms in neuroimaging. Medical Image Computing and Computer-Assisted Intervention–MICCAI 2004. Springer; 2004. p. 679-86.

273. Ledesma-Carbayo MJ, Kybic J, Desco M, Santos A, Sühling M, Hunziker P et al. Spatio-temporal nonrigid registration for ultrasound cardiac motion estimation. Medical Imaging, IEEE Transactions on. 2005;24(9):1113-26.

274. Comaniciu D, Zhou XS, Krishnan S. Robust real-time myocardial border tracking for echocardiography: an information fusion approach. Medical Imaging, IEEE Transactions on. 2004;23(7):849-60.

275. Shi J, Malik J. Normalized cuts and image segmentation. Pattern Analysis and Machine Intelligence, IEEE Transactions on. 2000;22(8):888-905.

276. Constantino J, Hu Y, Trayanova NA. A computational approach to understanding the cardiac electromechanical activation sequence in the normal and failing heart, with translation to the clinical practice of CRT. Progress in biophysics and molecular biology. 2012.

277. Wenk JF, Ge L, Zhang Z, Soleimani M, Potter DD, Wallace AW et al. A coupled biventricular finite element and lumped-parameter circulatory system model of heart failure. Computer methods in biomechanics and biomedical engineering. 2013;16(8):807-18.

278. Engwirda D. MESH2D - Automatic Mesh Generation (http://www.mathworks.com/matlabcentral/fileexchange/25555-mesh2d-automatic-mesh-generation), MATLAB Central File Exchange. Retrieved January 13, 2016. 2009.

279. Malmivuo J, Plonsey R. Bioelectromagnetism: principles and applications of bioelectric and biomagnetic fields. Oxford University Press, USA; 1995.

280. Piegari E, Di Salvo G, Castaldi B, Vitelli MR, Rodolico G, Golino P et al. Myocardial strain analysis in a doxorubicin-induced cardiomyopathy model. Ultrasound in medicine & biology. 2008;34(3):370-8.

281. Tsai H-R, Gjesdal O, Wethal T, Haugaa KH, Fosså A, Fosså SD et al. Left ventricular function assessed by two-dimensional speckle tracking echocardiography in long-term survivors of Hodgkin's lymphoma treated by mediastinal radiotherapy with or without anthracycline therapy. The American journal of cardiology. 2011;107(3):472-7.

282. Poterucha JT, Kutty S, Lindquist RK, Li L, Eidem BW. Changes in left ventricular longitudinal strain with anthracycline chemotherapy in adolescents precede subsequent decreased left ventricular ejection fraction. Journal of the American Society of Echocardiography. 2012;25(7):733-40.

283. Mavinkurve-Groothuis AM, Marcus KA, Pourier M, Loonen J, Feuth T, Hoogerbrugge PM et al. Myocardial 2D strain echocardiography and cardiac biomarkers in children during and shortly after anthracycline therapy for acute lymphoblastic leukaemia (ALL): a prospective study. European Heart Journal-Cardiovascular Imaging. 2013;14(6):562-9.

284. Cheung Y-f, Hong W-j, Chan GC, Wong SJ, Ha S-y. Left ventricular myocardial deformation and mechanical dyssynchrony in children with normal ventricular shortening fraction after anthracycline therapy. Heart. 2010;96(14):1137-41.

285. Stoodley PW, Richards DA, Hui R, Boyd A, Harnett PR, Meikle SR et al. Two-dimensional myocardial strain imaging detects changes in left ventricular systolic function immediately after anthracycline chemotherapy. European Heart Journal-Cardiovascular Imaging. 2011;12(12):945-52.

286. Stoodley PW, Richards DA, Boyd A, Hui R, Harnett PR, Meikle SR et al. Left ventricular systolic function in HER2/neu negative breast cancer patients treated with anthracycline chemotherapy: a comparative analysis of left ventricular ejection fraction and myocardial strain imaging over 12 months. European journal of cancer. 2013;49(16):3396-403.

287. Ibrahim ESH, Stuber M, Fahmy AS, Abd-Elmoniem KZ, Sasano T, Abraham MR et al. Real-time MR imaging of myocardial regional function using strain-encoding (SENC) with tissue through-plane motion tracking. Journal of Magnetic Resonance Imaging. 2007;26(6):1461-70.

288. Yun Y. Data processing for modeling with the NIR data (http://www.mathworks.com/matlabcentral/fileexchange/48493-data-processing-for-modeling-with-the-nir-data/content/Functions/smooth.m), MATLAB Central File Exchange. Retrieved February 08, 2016. 2014().

289. Kwon YW, Bang H. The finite element method using MATLAB. CRC; 2000.

290. Zienkiewicz OC, Taylor RL, Zhu JZ. The finite element method: its basis and fundamentals. Butterworth-Heinemann; 2005.

APPENDIX A – MYOCARDIAL CYCLE SIMULATION FROM KEY PHASES

Using all phases to simulate myocardial contraction provide reference contour data, on the other hand may consume an important amount of work in order to segment the myocardium through the whole cardiac cycle (i.e., ~25-30 phases). The use of templates and «contours initialisation technique» facilitated greatly this work. However, in order to speed up segmentation process, one may either combine manual segmentation with elastic registration or if permissible, segment only key phases of the cardiac cycle and interpolate the temporal displacements of myocardial contours. In both cases, a manual post-correction of contours is required to obtain accurate contours. The first phase, i.e., end-diastole, is most of the time required along with the end-systolic and end-early-diastole (i.e., the first phase representing late diastole period). These three phases provide key geometries of the myocardium during the cardiac cycle (Figure A.1), and in any case, should be manually segmented. To improve accuracy, a compromise can be made between manual post-correction of contours, and adding more phases to the initial segmentation process to interpolate myocardial displacement. Segmenting 30 phases, using templates and «contours initialisation technique» may require between one to two minutes of work. With the combination of interpolation/correction or elastic-registration/correction (Figure A.2), segmentation time may be reduced significantly.

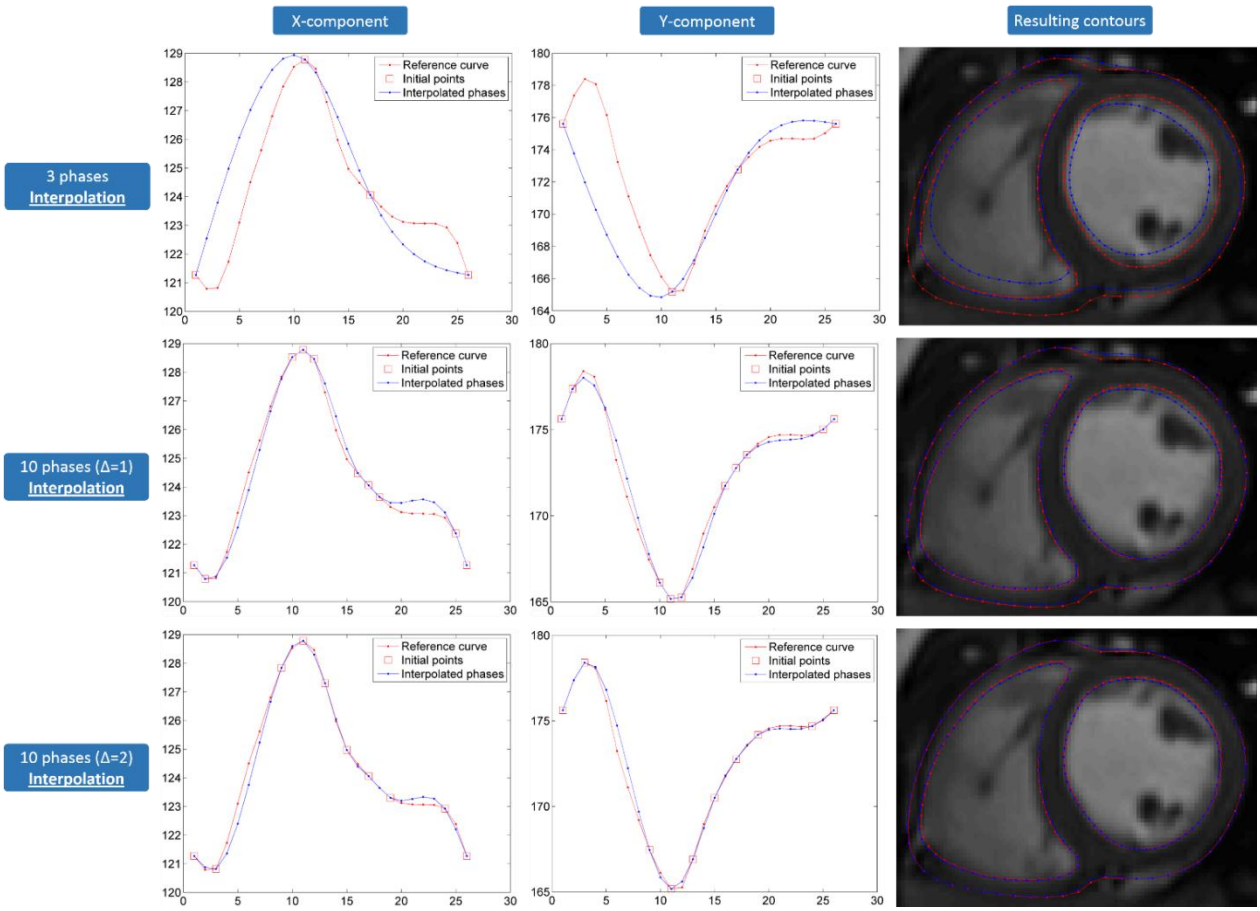

Figure A.1: Temporal interpolation of myocardial contours using: 3 key phases + 7x1-phase elastically registered steps (top) and 3 key phases + 7x2-phase elastically registered steps (bottom).

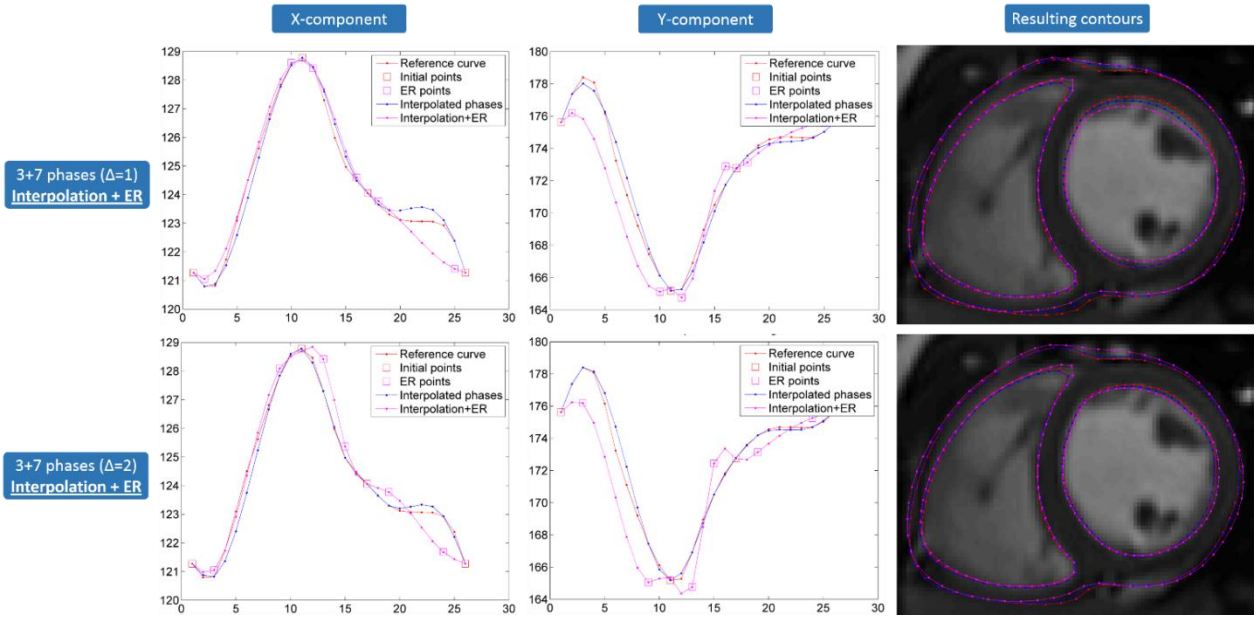

Figure A.2: Temporal interpolation of myocardial contours using: 3 key phases + 7x1-phase elastically registered steps (top) and 3 key phases + 7x2-phase elastically registered steps (bottom).

An attempt to reduce myocardial displacements was done by interpolating a slice between each two phases of the cardiac cycle (Figure A.3). Which resulted in 51 images: 26 (initial) plus 25 (interpolated) images. However, even with smaller myocardial displacements between two phases did not improve myocardial tracking accuracy.

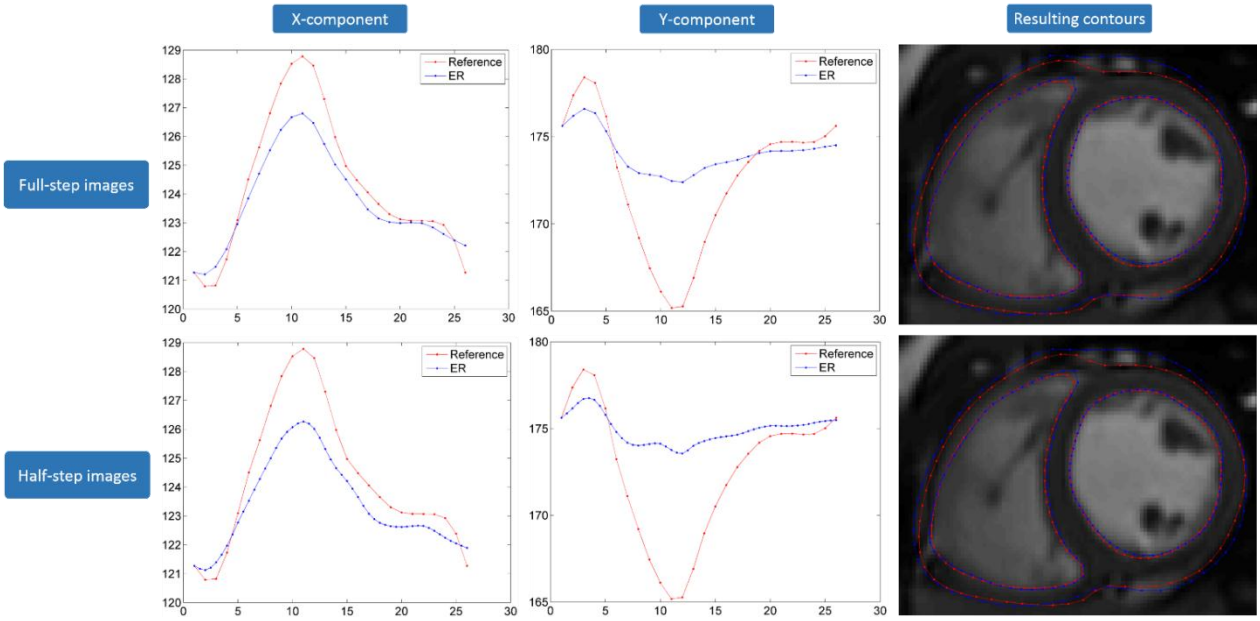

Figure A.3: Temporal interpolation of myocardial contours using elastic registration with: 26 phases (top) and 26+25=51 reconstructed images with interpolated mid-phases (bottom). Resulting contours are shown during the 5th phase, i.e., mid-systole.

APPENDIX B – MYOCARDIAL DISPLACEMENTS SMOOTHING

In order to reduce segmentation errors, while trying to avoid contours displacements, a slight smoothing was added to the x and y components of the temporal displacement of each point along myocardial contours. By doing so, contours displacements were fairly stabilized through the cardiac cycle, while keeping as much as possible the accuracy of the contours (see Figures B.1 to B.3). Moreover, smoothing may significantly reduce segmentation fluctuations, i.e., segmentation errors, during low displacement periods. Smoothing was accomplished using a 1D custom smooth function with an iterative correction where the resulting points are obtained as follow (for a single iteration):

$$P^{i}{}_{final} = \frac{P^{i-1}{}_{initial}}{6} + \frac{2 * P^{i}{}_{initial}}{3} + \frac{P^{i+1}{}_{initial}}{6} \qquad i = 2 \dots end - 1 \quad (B1)$$

Points were smoothed iteratively using a smoothing degree, i.e., number of iteration, which was set to 3 during our simulation. The weights have been set to: $\left[\frac{1}{6} \quad \frac{2}{3} \quad \frac{1}{6}\right]$, however, for a stronger correction, one may apply a stronger correction by setting a higher weight to adjacent points, i.e., $\left[\frac{1}{4} \quad \frac{1}{2} \quad \frac{1}{4}\right]$. Results were also compared to the Matlab function “smooth.m” from the Matlab Central’s File Exchange [288].

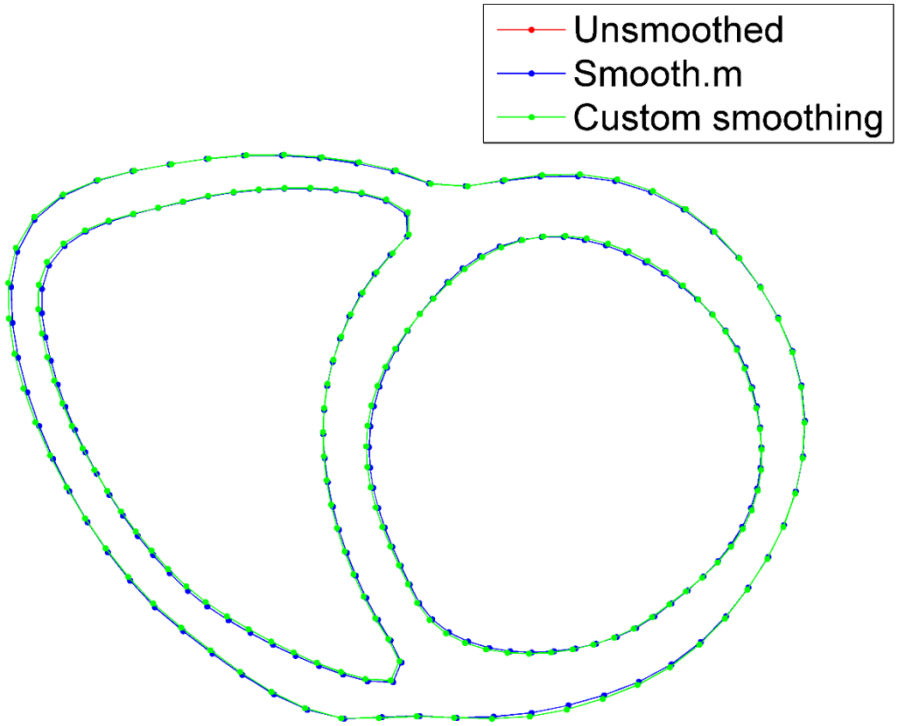

Figure B.1: End-diastolic contours with temporal smoothing in short-axis view.

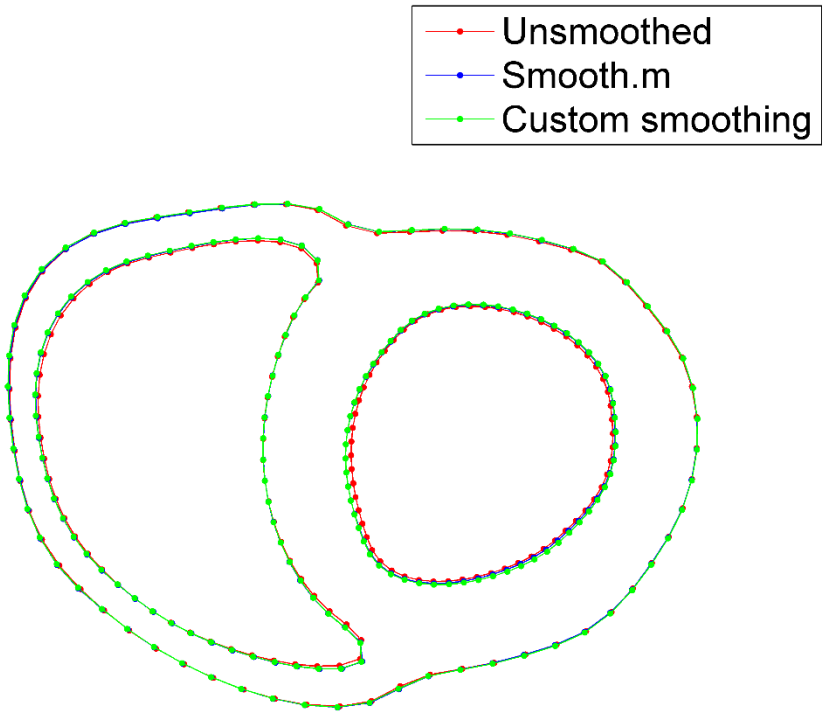

Figure B.2: End-systolic contours with temporal smoothing in short-axis view.

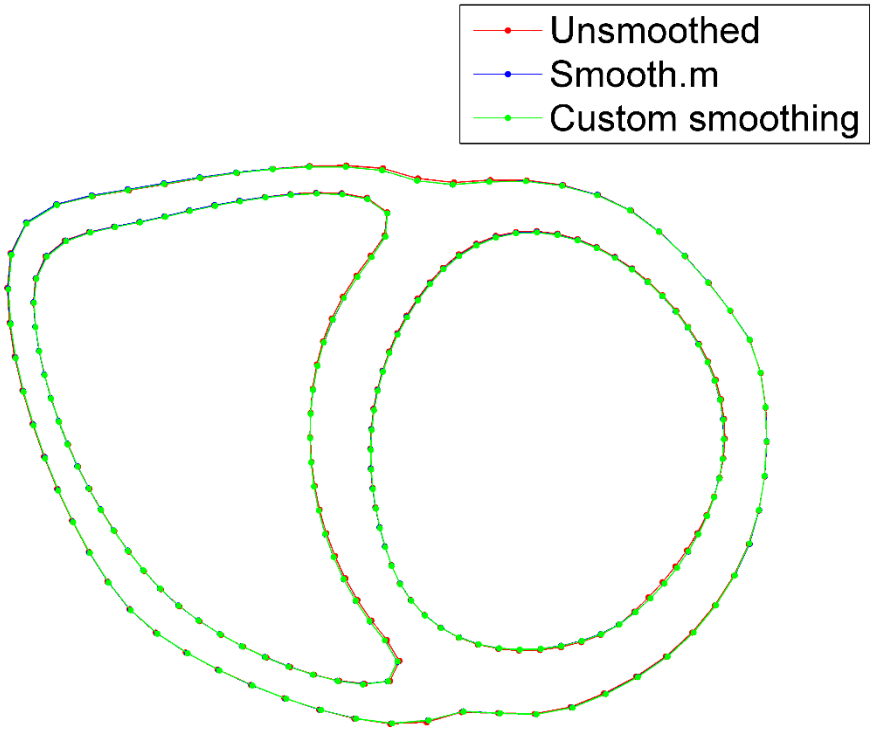

Figure B.3: Early-diastole contours with temporal smoothing in short-axis view.

Both smoothing functions fairly preserve myocardial geometry, however with Custom smoothing function, one may add one or several points as fixed points, where no smoothing is applied. In our context, the first and last points, representing the end-diastole/systole-start were fixed as reference points (See Figure B.4). This was necessary because a simple smoothing function may significantly alter these points, which may result in significant geometric variation, if no boundary limit is applied.

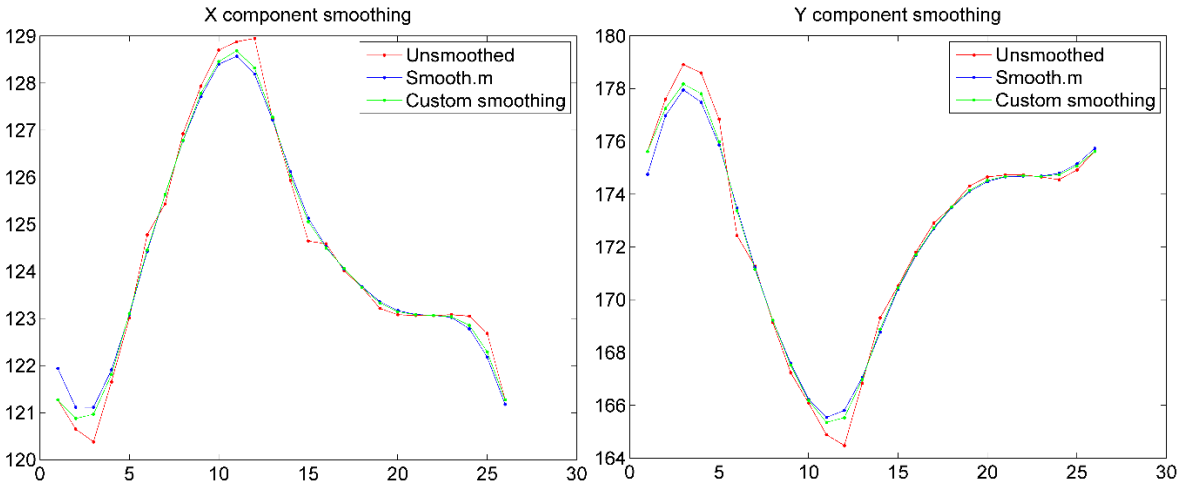

Figure B.4: Example of an X- and Y-component smoothing for a point taken along the endocardial RV curve.

The zigzag course seen from myocardial displacement paths (Figure B.5), caused mainly by segmentation errors, was considerably reduced after smoothing myocardial displacements. However, the torsional aspect of the curves, was kept fairly similar (see Figure B.5).

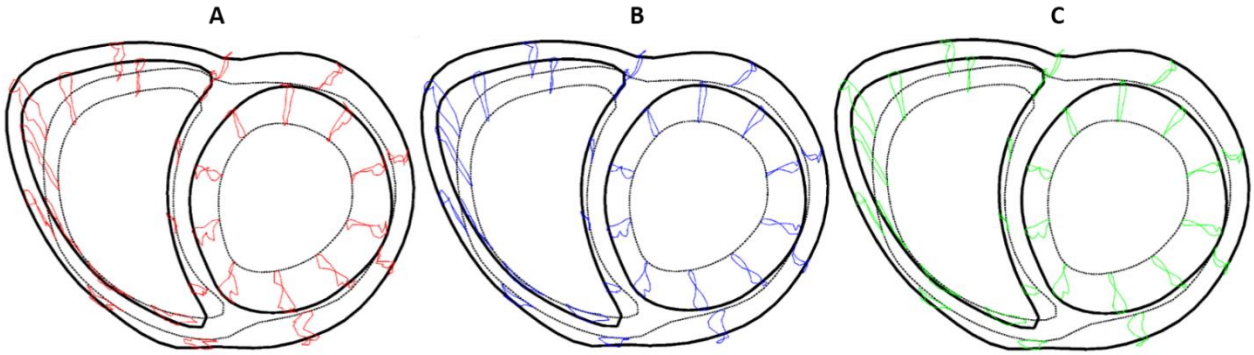

Figure B.5: Displacement paths in short-axis view: Unsmoothed (a), smoothed using "Smooth.m" (b) and smoothed using Custom smoothing (c).

APPENDIX C – MYOCARDIAL DISPLACEMENTS ESTIMATION USING ELASTIC REGISTRATION

Elastic registration [239] failed to provide a robust estimation for myocardial displacements using clinical cine MRI. Particularly when estimating displacements from two distant phases of the cardiac cycle. Using different levels of image pixels' depth (see Figure C.1) had little to no effects on the final result (Figure C.2). The only difference was that unsigned integer 16 (uint16) kept most of the signal unchanged while unsigned integer 8 (uint8) resulting in an image with reduced sharpness and details due to depth conversion, i.e., reduction.

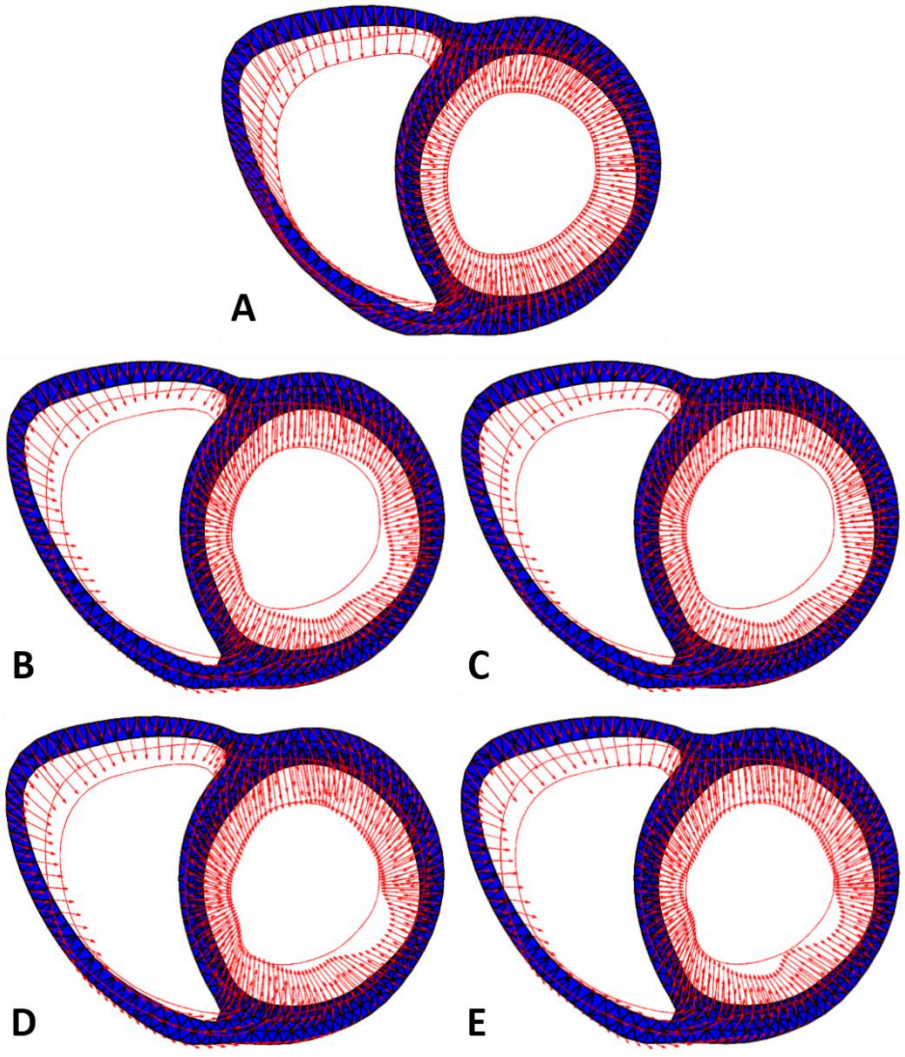

Figure C.1: Myocardial displacement field in short-axis view using: contour tracking as a reference (a), compared with elastic registration with: uint8 images/no contrast enhancement (b), uint8 images/with contrast enhancement (c), uint16 images/no contrast enhancement (d) and uint16 images/no contrast enhancement (e).

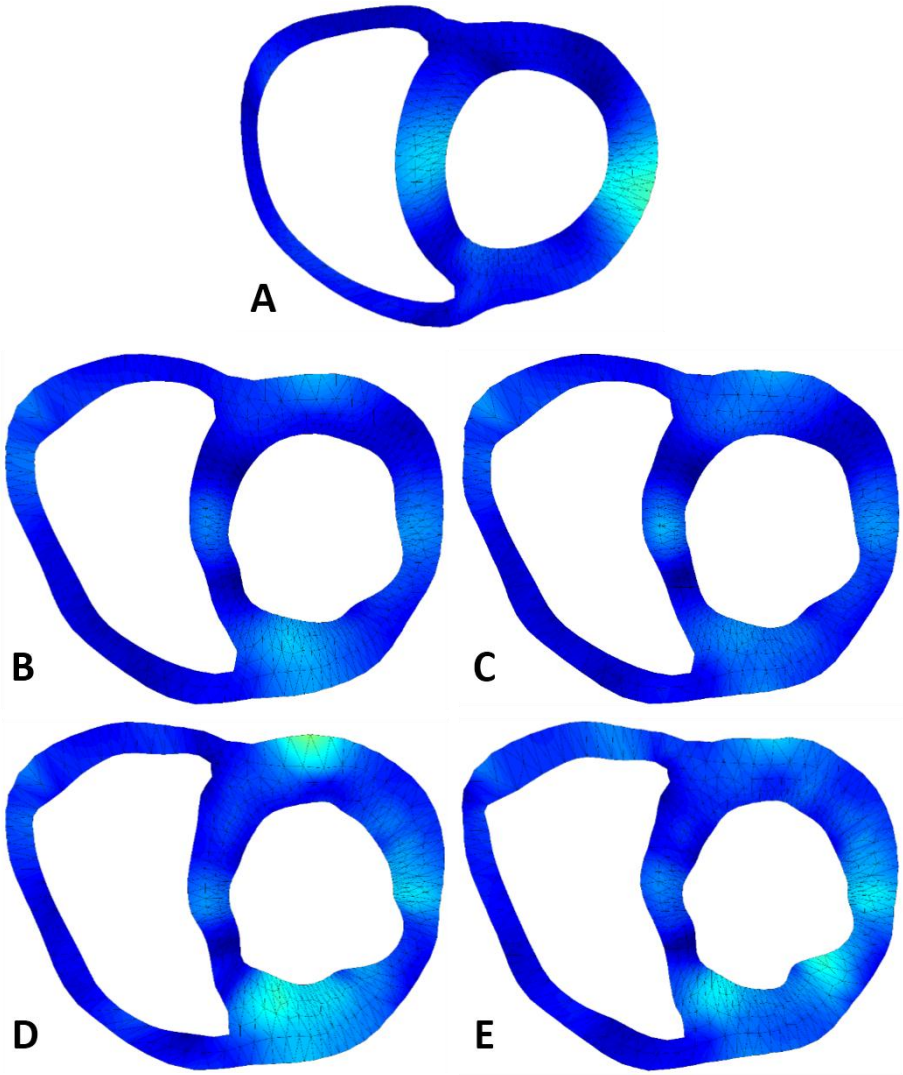

Figure C.2: Myocardial strains distribution in short-axis view from: contour tracking as a reference (a), compared with elastic registration with: uint8 images/no contrast enhancement (b), uint8 images/with contrast enhancement (c), uint16 images/no contrast enhancement (d) and uint16 images/no contrast enhancement (e).

Windowing myocardial region of interest, i.e., zooming, or enhancing images resolution (Figure C.3) had little effect on myocardial tracking accuracy using elastic registration technique (Figure C.4).

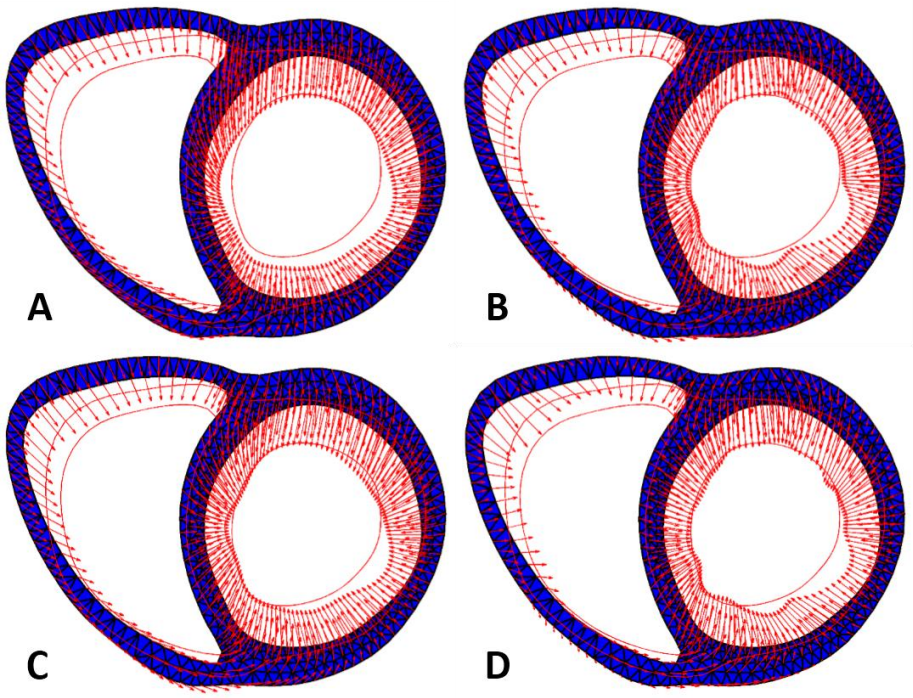

Figure C.3: Myocardial displacement field in short-axis view using: unzoomed 256x256 images (a), compared with: zoomed 256x256 images (b), unzoomed 512x512 images (c) and zoomed 512x512 images (d).

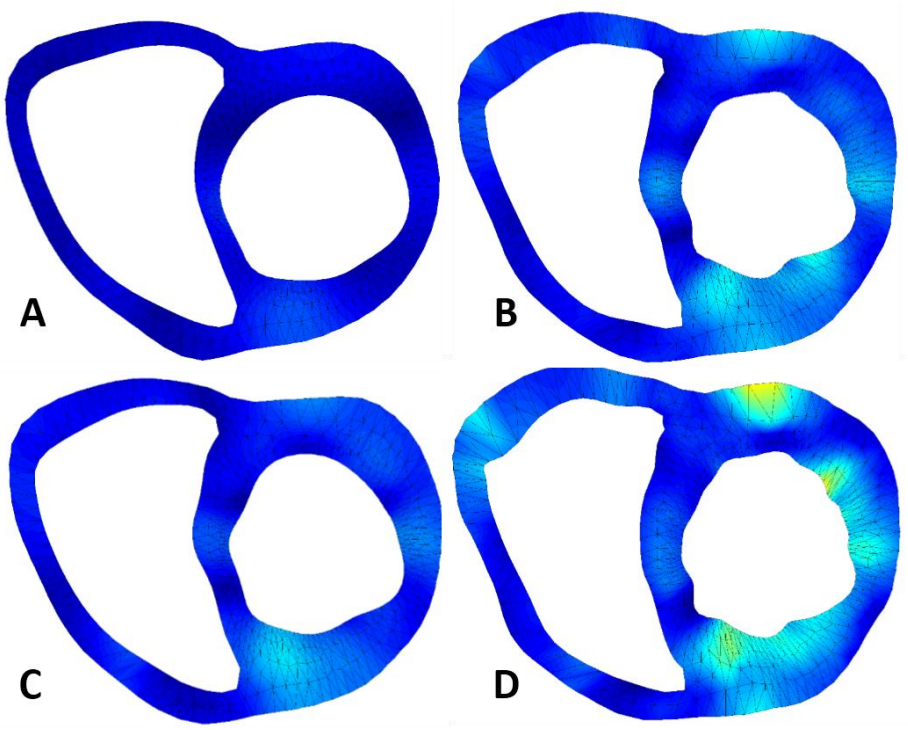

Figure C.4: Myocardial strains distribution in short-axis view from: unzoomed 256x256 images (a), compared with: zoomed 256x256 images (b), unzoomed 512x512 images (c) and zoomed 512x512 images (d).

APPENDIX D – FINITE-ELEMENT ANALYSIS DIAGRAM

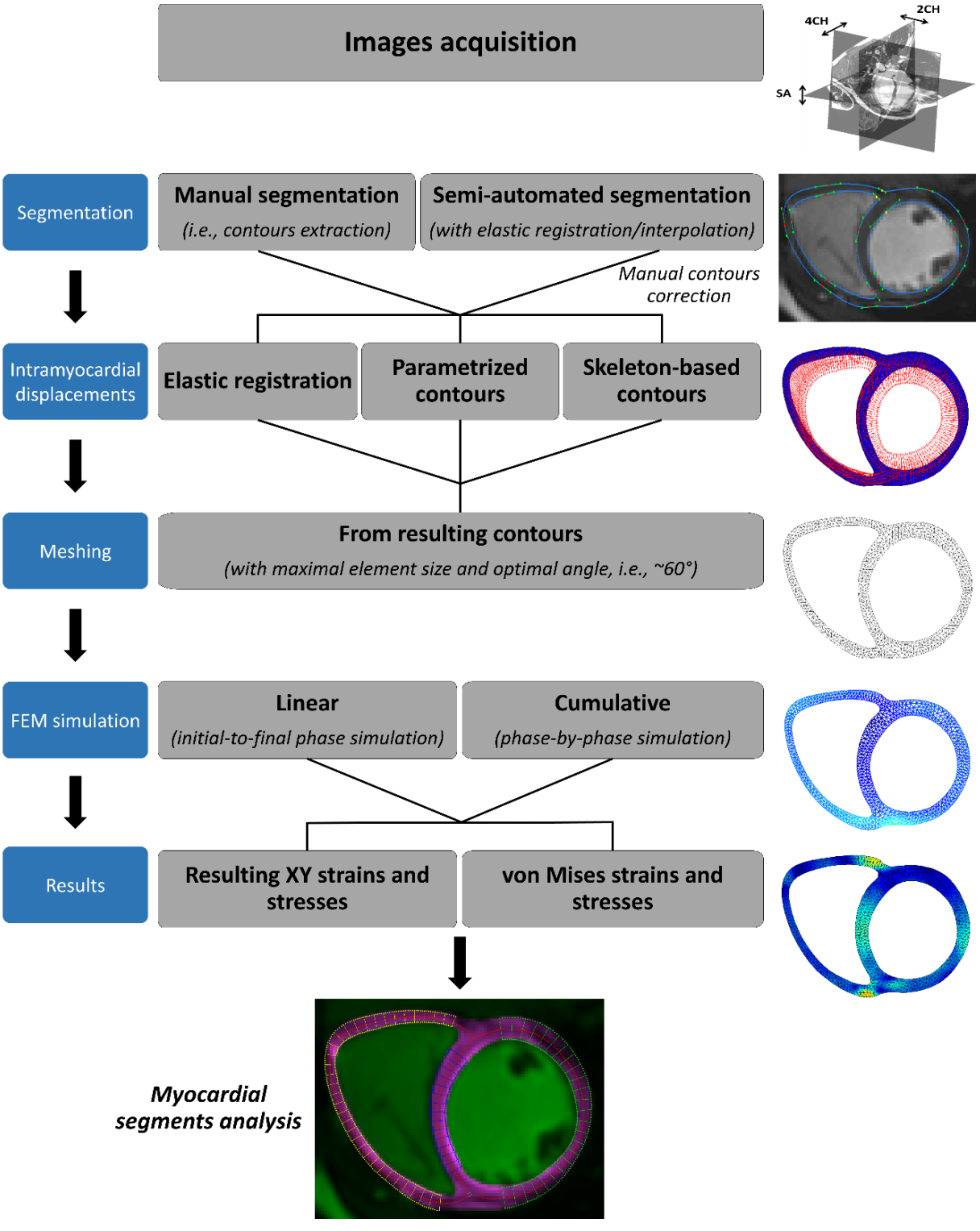

Figure D.1: Myocardial finite element analysis methodology.

APPENDIX E – FINITE-ELEMENT EQUATIONS

The 3D equations [289] of equilibrium (derived from summation of forces in x, y and z directions) over an infinitesimal element are:

$$\frac{\partial \sigma_x}{\partial x} + \frac{\partial \tau_{xy}}{\partial y} + \frac{\partial \tau_{xz}}{\partial z} + f_x = 0 \tag{E1}$$

$$\frac{\partial \tau_{xy}}{\partial x} + \frac{\partial \sigma_y}{\partial y} + \frac{\partial \tau_{yz}}{\partial z} + f_y = 0 \tag{E2}$$

$$\frac{\partial \tau_{xz}}{\partial x} + \frac{\partial \tau_{yz}}{\partial y} + \frac{\partial \sigma_z}{\partial z} + f_z = 0 \tag{E3}$$

For an isotropic material, the constitutive equation which state the relationship between stress and strains (relative displacements) is:

$$\{\sigma\} = [D]\{\varepsilon\} \tag{E4}$$

Where,

$$\{\sigma\} = \{\sigma_x \quad \sigma_y \quad \sigma_y \quad \tau_{xy} \quad \tau_{yz} \quad \tau_{xz}\}^T \tag{E5}$$

$$\{\epsilon\} = \{\epsilon_x \quad \epsilon_y \quad \epsilon_z \quad \gamma_{xy} \quad \gamma_{yz} \quad \gamma_{xz}\}^T \tag{E6}$$

And,

$$[D] = \frac{E}{(1+\upsilon)(1-2\upsilon)}\begin{bmatrix} 1-\upsilon & \upsilon & \upsilon & 0 & 0 & 0 \\ \upsilon & 1-\upsilon & \upsilon & 0 & 0 & 0 \\ \upsilon & \upsilon & 1-\upsilon & 0 & 0 & 0 \\ 0 & 0 & 0 & \frac{1-2\upsilon}{2} & 0 & 0 \\ 0 & 0 & 0 & 0 & \frac{1-2\upsilon}{2} & 0 \\ 0 & 0 & 0 & 0 & 0 & \frac{1-2\upsilon}{2} \end{bmatrix} \quad \text{(E7)}$$

However, for an anisotropic material [290] the D matrix is:

$$[D] = \begin{bmatrix} D_{11} & D_{12} & D_{13} & D_{14} & D_{15} & D_{16} \\ D_{21} & D_{22} & D_{23} & D_{24} & D_{25} & D_{26} \\ D_{31} & D_{32} & D_{33} & D_{34} & D_{35} & D_{36} \\ D_{41} & D_{42} & D_{43} & D_{44} & D_{45} & D_{46} \\ D_{51} & D_{52} & D_{53} & D_{54} & D_{55} & D_{56} \\ D_{61} & D_{62} & D_{63} & D_{64} & D_{65} & D_{66} \end{bmatrix} \quad \text{(E8)}$$

Where $D_{ij} = D_{ji}$, which lead the problem to 21 unknown material parameters. For materials that have two or three planes of material symmetry (orthotropic) such as muscle fibers (with two planes of symmetry) aligned with x axis, the number of unknowns is reduced to 9 and the relation become:

$$\begin{Bmatrix} \epsilon_x \\ \epsilon_y \\ \epsilon_z \\ \gamma_{xy} \\ \gamma_{yz} \\ \gamma_{xz} \end{Bmatrix} = \begin{bmatrix} \frac{1}{E_x} & -\frac{\upsilon_{xy}}{E_y} & -\frac{\upsilon_{xz}}{E_z} & 0 & 0 & 0 \\ -\frac{\upsilon_{yx}}{E_x} & \frac{1}{E_y} & -\frac{\upsilon_{yz}}{E_z} & 0 & 0 & 0 \\ -\frac{\upsilon_{zx}}{E_x} & -\frac{\upsilon_{zy}}{E_y} & \frac{1}{E_z} & 0 & 0 & 0 \\ 0 & 0 & 0 & \frac{1}{G_{xy}} & 0 & 0 \\ 0 & 0 & 0 & 0 & \frac{1}{G_{yz}} & 0 \\ 0 & 0 & 0 & 0 & 0 & \frac{1}{G_{zx}} \end{bmatrix} \begin{Bmatrix} \sigma_x \\ \sigma_y \\ \sigma_z \\ \tau_{xy} \\ \tau_{yz} \\ \tau_{xz} \end{Bmatrix} = [D]^{-1}\{\sigma\} \qquad \text{(E9)}$$

Where E_x and $E_y = E_z$ are elastic moduli along x, y and z directions, $\upsilon_{yz} \approx \upsilon_{xy} = \upsilon_{xz}$ are Poisson ratios and $G_{yz}, G_{xy} = G_{xz}$ are shear moduli, reducing the number of unknowns to 6: two directional moduli, two Poisson ratios and two shear moduli. In order to avoid system singularities, The Poisson's ratio is set at $\upsilon = 0.45 - 0.49$. Although the myocardium is not completely incompressible, it is reported that myocardial volume change during the cardiac cycle is no more than 4%, and less than 2% in any direction [243].

The kinematic equation which derive strains from displacement (for small displacements) is:

$$\begin{Bmatrix} \epsilon_x \\ \epsilon_y \\ \epsilon_z \\ \gamma_{xy} \\ \gamma_{yz} \\ \gamma_{xz} \end{Bmatrix} = \begin{Bmatrix} \frac{\partial u}{\partial x} \\ \frac{\partial v}{\partial y} \\ \frac{\partial w}{\partial z} \\ \frac{\partial v}{\partial x} + \frac{\partial u}{\partial y} \\ \frac{\partial w}{\partial y} + \frac{\partial v}{\partial z} \\ \frac{\partial w}{\partial x} + \frac{\partial u}{\partial z} \end{Bmatrix} \qquad \text{(E10)}$$

Where u, v and w are displacement in the x, y and z directions, respectively. After applying the weighted residual method to Equations (E1), (E2) and (E3) and writing them together, the system become:

$$\int_{\Omega}\begin{Bmatrix}\omega_1(\frac{\partial\sigma_x}{\partial x}+\frac{\partial\tau_{xy}}{\partial y}+\frac{\partial\tau_{xz}}{\partial z})\\ \omega_2(\frac{\partial\tau_{xy}}{\partial x}+\frac{\partial\sigma_y}{\partial y}+\frac{\partial\tau_{yz}}{\partial z})\\ \omega_3(\frac{\partial\tau_{xz}}{\partial x}+\frac{\partial\tau_{yz}}{\partial y}+\frac{\partial\sigma_z}{\partial z})\end{Bmatrix}d\Omega+\int_{\Omega}\begin{Bmatrix}\omega_1 f_x)\\ \omega_2 f_y\\ \omega_3 f_z\end{Bmatrix}-\int_{\Lambda}\begin{Bmatrix}\omega_1\phi_x\\ \omega_2\phi_y\\ \omega_3\phi_z\end{Bmatrix}d\Lambda=0 \qquad \text{(E11)}$$

Where Λ is the imposed boundary condition that can be either a displacement or traction defined over a sub-region $\Lambda \in \Omega$. Applying integration by parts and substituting the constitutive equation and the kinematic equation in the first part of Eq. (E11) gives:

$$\int_{\Omega^e}[B]^T[D][B]\,d\Omega\{d\}-\int_{\Omega^e}[N]^T\begin{Bmatrix}f_x\\ f_y\\ f_z\end{Bmatrix}d\Lambda+\int_{s_m}^{s_n}\begin{pmatrix}\frac{s_n-s}{s_n-s_m} & 0 & 0\\ 0 & \frac{s_n-s}{s_n-s_m} & 0\\ 0 & 0 & \frac{s_n-s}{s_n-s_m}\\ \frac{s-s_m}{s_n-s_m} & 0 & 0\\ 0 & \frac{s-s_m}{s_n-s_m} & 0\\ 0 & 0 & \frac{s-s_m}{s_n-s_m}\end{pmatrix}\begin{Bmatrix}\phi_x\\ \phi_y\\ \phi_z\end{Bmatrix}=0 \qquad \text{(E12)}$$

Where the element stiffness matrix, integrated over element domain Ω^e, is

$$[K^e]=\int_{\Omega^e}[B]^T[D][B]\,d\Omega \qquad \text{(E13)}$$

As our model uses 3-node triangles or 4-node tetrahedron, the linear shape function for each element is

$$\begin{Bmatrix} u \\ v \\ w \end{Bmatrix} = \begin{bmatrix} H_1 & 0 & 0 & H_2 & 0 & 0 & H_3 & 0 & 0 & H_4 & 0 & 0 \\ 0 & H_1 & 0 & 0 & H_2 & 0 & 0 & H_3 & 0 & 0 & H_4 & 0 \\ 0 & 0 & H_1 & 0 & 0 & H_2 & 0 & 0 & H_3 & 0 & 0 & H_4 \end{bmatrix} \begin{Bmatrix} u_1 \\ v_1 \\ w_1 \\ u_2 \\ v_2 \\ w_2 \\ u_3 \\ v_3 \\ w_3 \\ u_4 \\ v_4 \\ w_4 \end{Bmatrix} = [N]\{d\} \tag{E14}$$

Where $\{d\}$ is the nodal displacement vector. Substituting Eq. (E14) into the kinematic equation results in

$$\begin{Bmatrix} \epsilon_x \\ \epsilon_y \\ \epsilon_z \\ \gamma_{xy} \\ \gamma_{yz} \\ \gamma_{xz} \end{Bmatrix} = \begin{bmatrix} \frac{\partial H_1}{\partial x} & 0 & 0 & \frac{\partial H_2}{\partial x} & 0 & 0 & \frac{\partial H_3}{\partial x} & 0 & 0 & \frac{\partial H_4}{\partial x} & 0 & 0 \\ 0 & \frac{\partial H_1}{\partial y} & 0 & 0 & \frac{\partial H_2}{\partial y} & 0 & 0 & \frac{\partial H_3}{\partial y} & 0 & 0 & \frac{\partial H_4}{\partial y} & 0 \\ 0 & 0 & \frac{\partial H_1}{\partial z} & 0 & 0 & \frac{\partial H_2}{\partial z} & 0 & 0 & \frac{\partial H_3}{\partial z} & 0 & 0 & \frac{\partial H_4}{\partial z} \\ \frac{\partial H_1}{\partial y} & \frac{\partial H_1}{\partial x} & 0 & \frac{\partial H_2}{\partial y} & \frac{\partial H_2}{\partial x} & 0 & \frac{\partial H_3}{\partial y} & \frac{\partial H_3}{\partial x} & 0 & \frac{\partial H_4}{\partial y} & \frac{\partial H_4}{\partial x} & 0 \\ 0 & \frac{\partial H_1}{\partial z} & \frac{\partial H_1}{\partial y} & 0 & \frac{\partial H_2}{\partial z} & \frac{\partial H_2}{\partial y} & 0 & \frac{\partial H_3}{\partial z} & \frac{\partial H_3}{\partial y} & 0 & \frac{\partial H_4}{\partial z} & \frac{dH_4}{dy} \\ \frac{dH_1}{dz} & 0 & \frac{\partial H_1}{\partial x} & \frac{\partial H_2}{\partial z} & 0 & \frac{\partial H_2}{\partial x} & \frac{\partial H_3}{\partial z} & 0 & \frac{\partial H_3}{\partial x} & \frac{\partial H_4}{\partial z} & 0 & \frac{dH_4}{dx} \end{bmatrix} \begin{Bmatrix} u_1 \\ v_1 \\ w_1 \\ u_2 \\ v_2 \\ w_2 \\ u_3 \\ v_3 \\ w_3 \\ u_4 \\ v_4 \\ w_4 \end{Bmatrix} = [B]\{d\} \tag{E15}$$

Finally, replacing matrix $[D]$ from Eq. (E4), for a specific material (isotropic or orthotropic), and matrix $[B]$ from Eq. (E15), for a tetrahedron element (or 2D or 3D elements), into Eq. (E13) results in element stiffness matrix

$$[K^e] = [B]^T[D][B]V \tag{E16}$$

Where V represents the tetrahedron volume or triangular area in 2D.

APPENDIX F – STRAINS AND STRESSES DISTRIBUTIONS FOR EACH CARDIAC INTERVAL USING VON MISES AND XY INDICES: CUMULATIVE VS. LINEAR TECHNIQUE

Linear and cumulative strains and stresses are shown using either von Mises or XY index (Figures F.1 to F.5). Results are compared between SR and HR group and between cancer survivors and healthy volunteers.

Figure F.1: “Linear” von Mises strains and stresses.

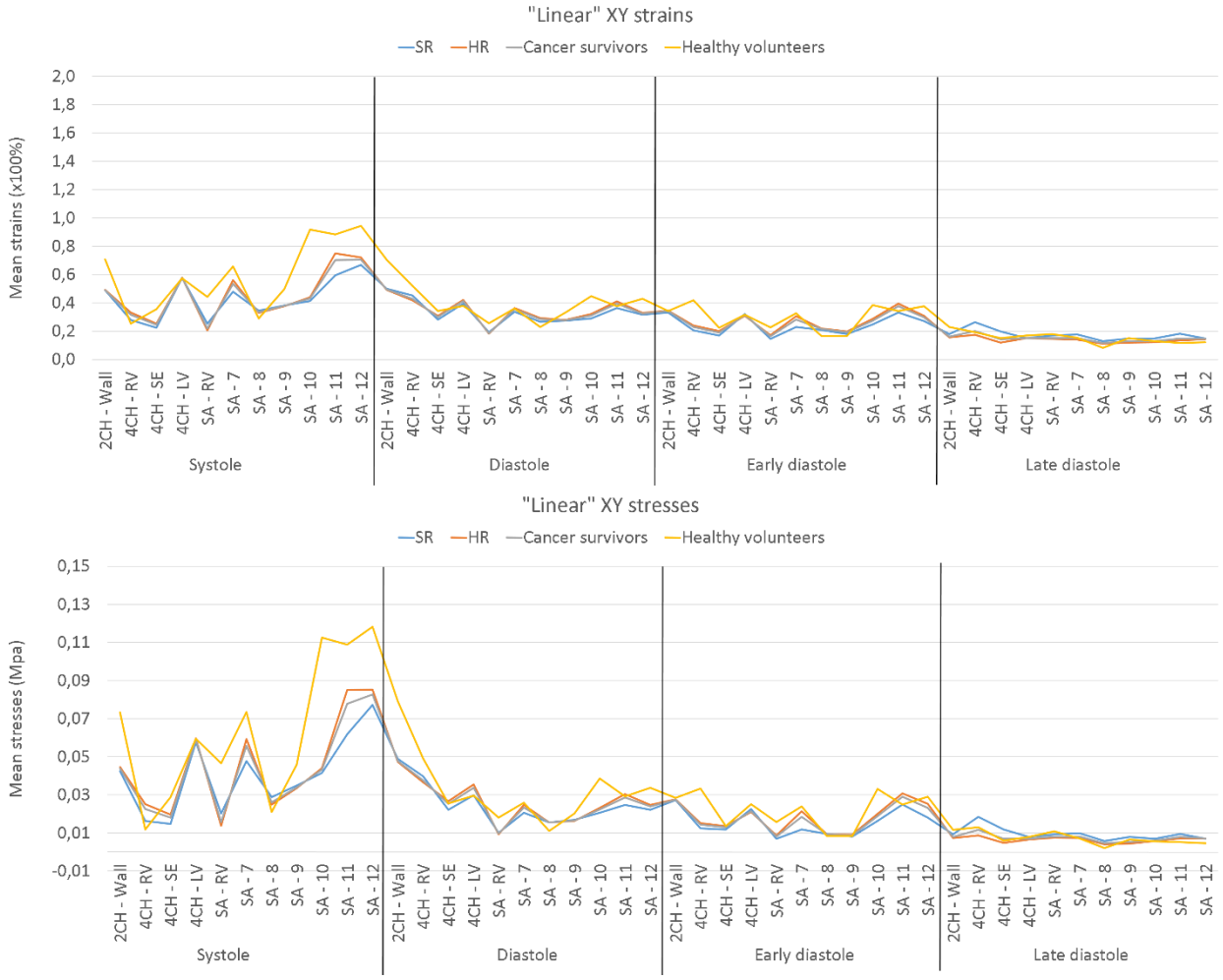

Figure F.2: “Linear” XY strains and stresses.

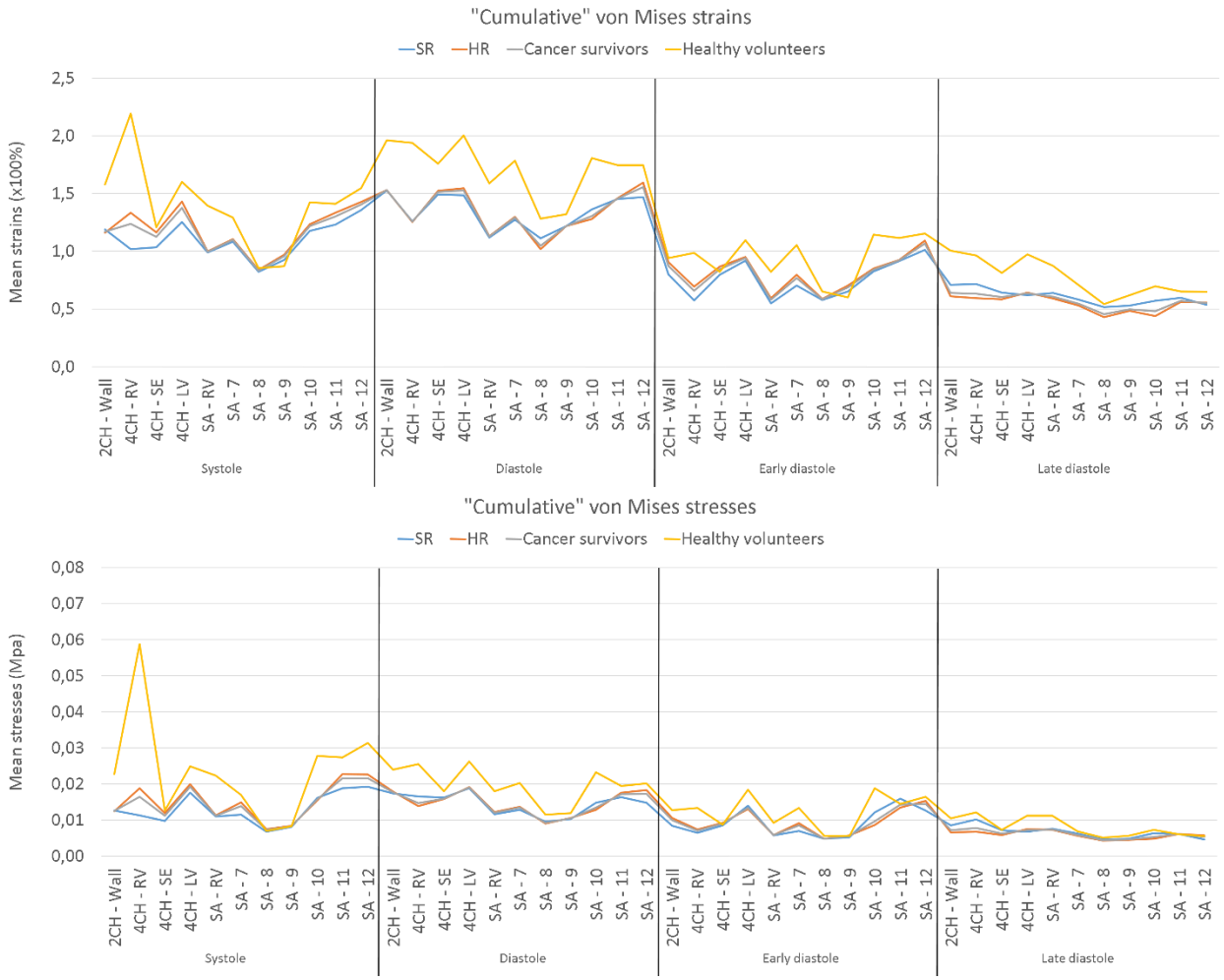

Figure F.3: “Cumulative” von Mises strains and stresses.

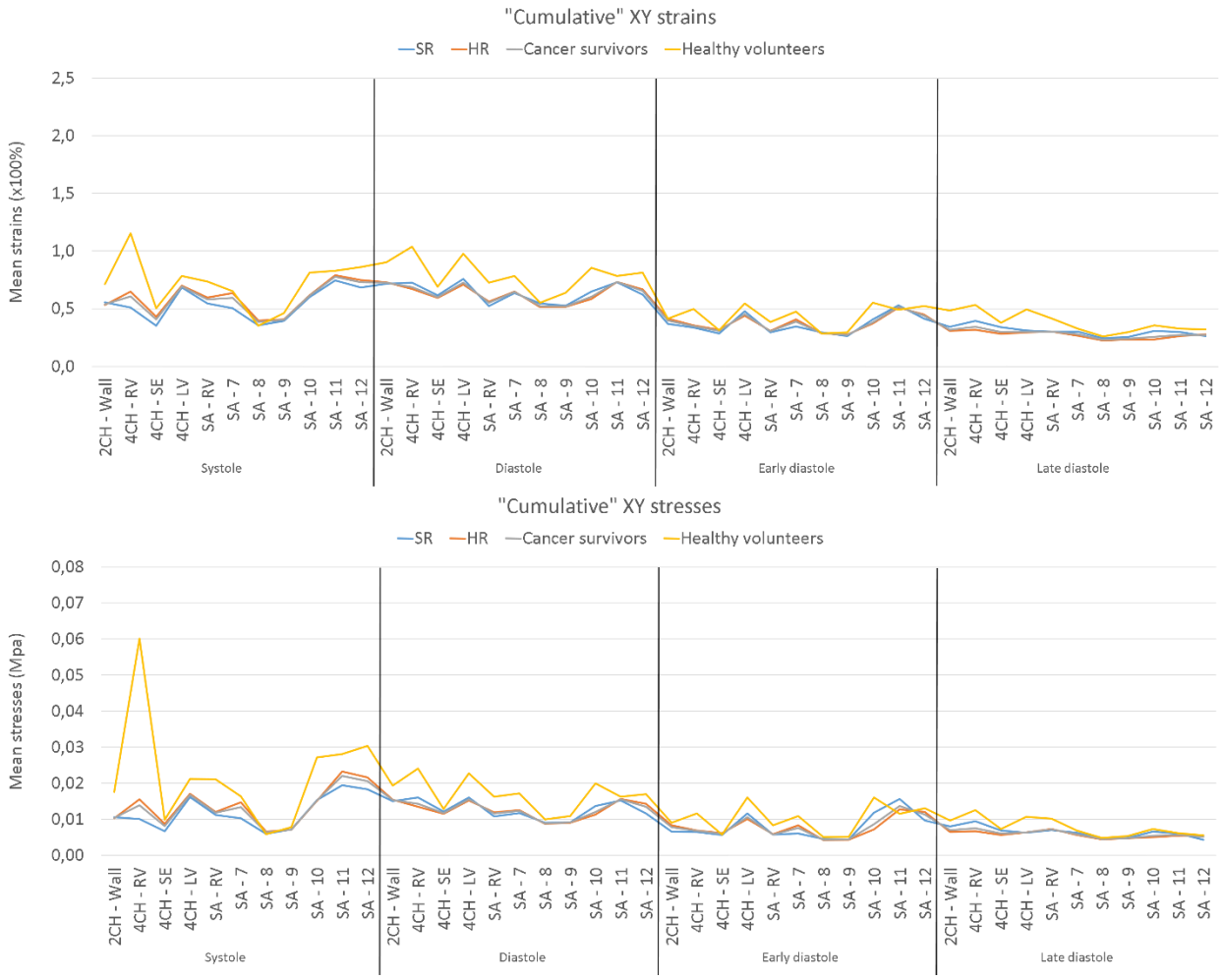

Figure F.4: “Cumulative” XY strains and stresses.

Linear and cumulative estimation techniques for strains and stresses are compared in Table F.1

Table F.1: linear vs. cumulative estimation techniques for strains and stresses

Technique	Displacements from:	Advantages	Limits
Linear	***Raw contours***	• Accurate tracking • Cancel residual strains/stresses	• Sliding phenomenon if large deformations
	Elastic registration	• Uniform displacement flow	• Poor tracking if large deformations
	Calibrated contours	• Excellent accuracy	• Pixelation effects
Cumulative	***Raw contours***	• Mesh stabilisation every phase	• Keep residual strains/stresses
	Elastic registration	• Acceptable accuracy • Mesh stabilisation every phase	• Keep residual strains/stresses
	Calibrated contours	• Excellent accuracy	• Pixelation effects

APPENDIX G – 3D MODELING OF THE HEART: PERSPECTIVES

2-dimensional modeling of the myocardium in 2-chamber, 4-chamber and short-axis views serves as a building block for a 3D model. Current imaging techniques rely mainly on 2D images such as 2D cine MRI. The combination of these 3 orientations may provide enough information to estimate 3D myocardial displacement at any point. In this work, we concentrated our efforts mainly in 2D myocardial tracking in order to develop an accurate estimation technique of myocardial displacement. At this point, from cine MRI images, one promising technique is to reconstitute contours from the myocardial skeleton by projection myocardial skeleton curves back into myocardial contours, as discussed previously. The calibration of myocardial contours is mainly done using key skeleton-based points (Fig G.1), which can be considered as anatomical references from tracking. Using these resulting contours, i.e., calibrated contours, one could estimate intra-myocardial displacement at any given point using an interpolator function such as kriging. Furthermore, such points may provide a stable parametrization for 3D contours (Fig G.2), which paves the way for 3D myocardial tracking (Figure G.3).

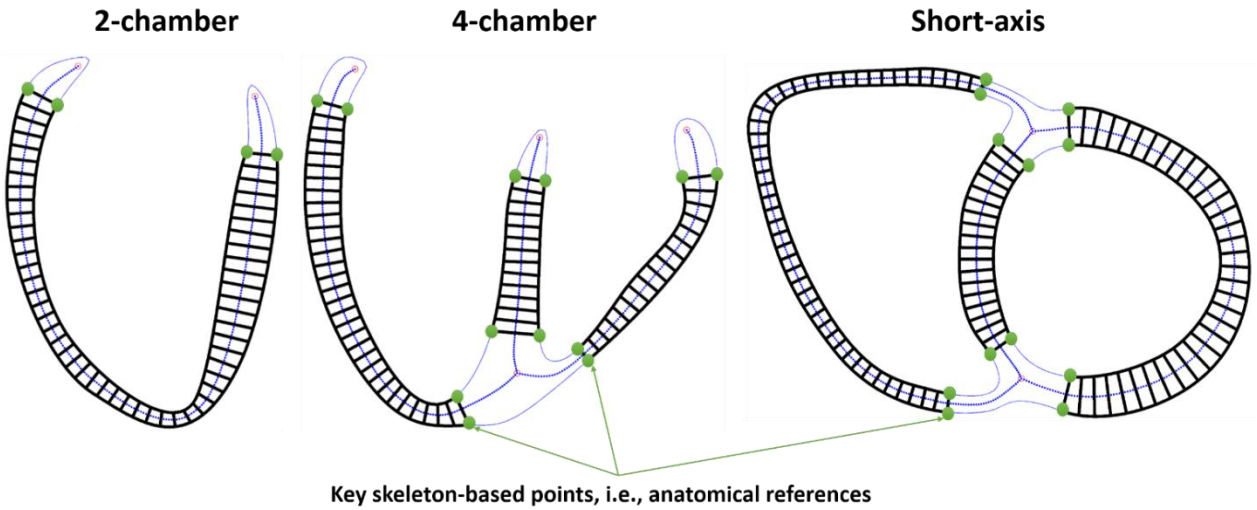

Figure G.1: Key skeleton-based anatomical points which may be used for 3D myocardial tracking.

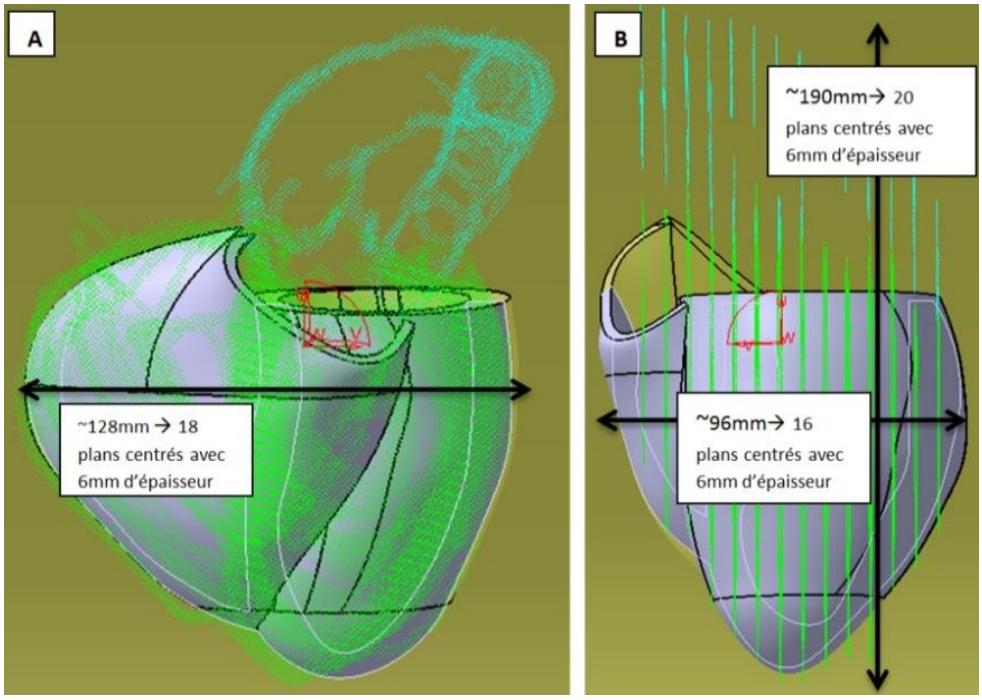

Figure G.2: Preliminary model of the ventricular myocardium obtained using 3-planes segmentation. A, 4-chambers view (long vertical axis). B, 2-chambers view (long horizontal axis).

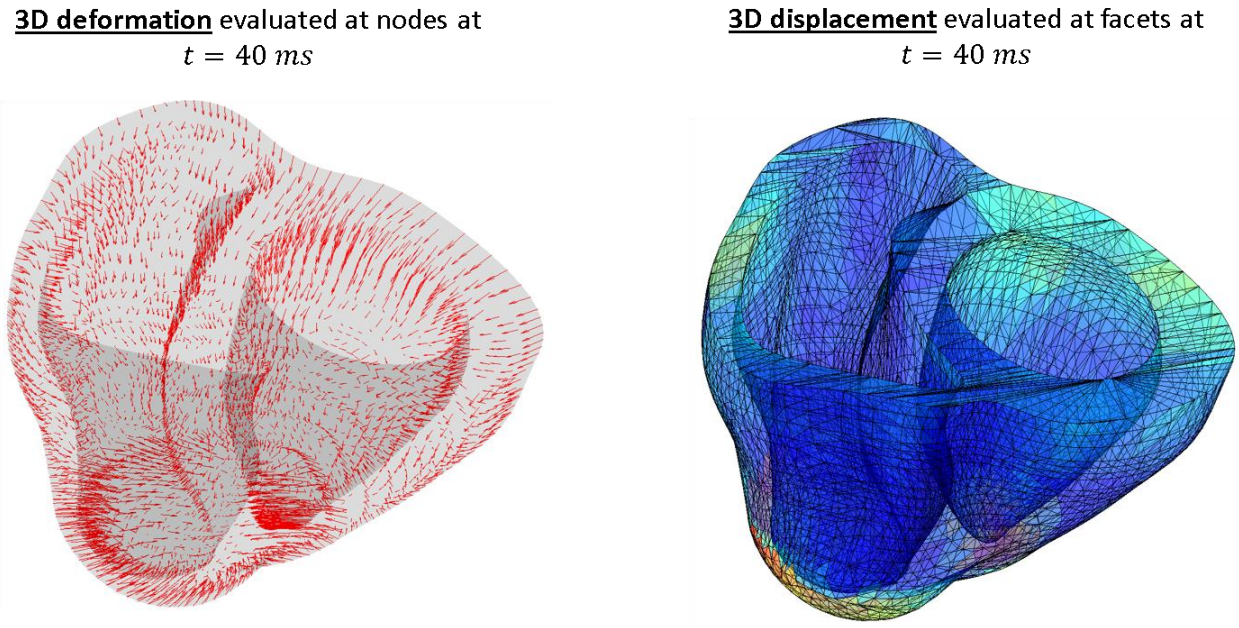

Figure G.3: Preliminary model of the ventricular myocardium obtained using 3-planes segmentation.

APPENDIX H – CARDIOLAB: A NEW SEGMENTATION SOFTWARE

The main segmentation software used to segment cine MRI images and display 3D segmentation is shown in Figure H.1:

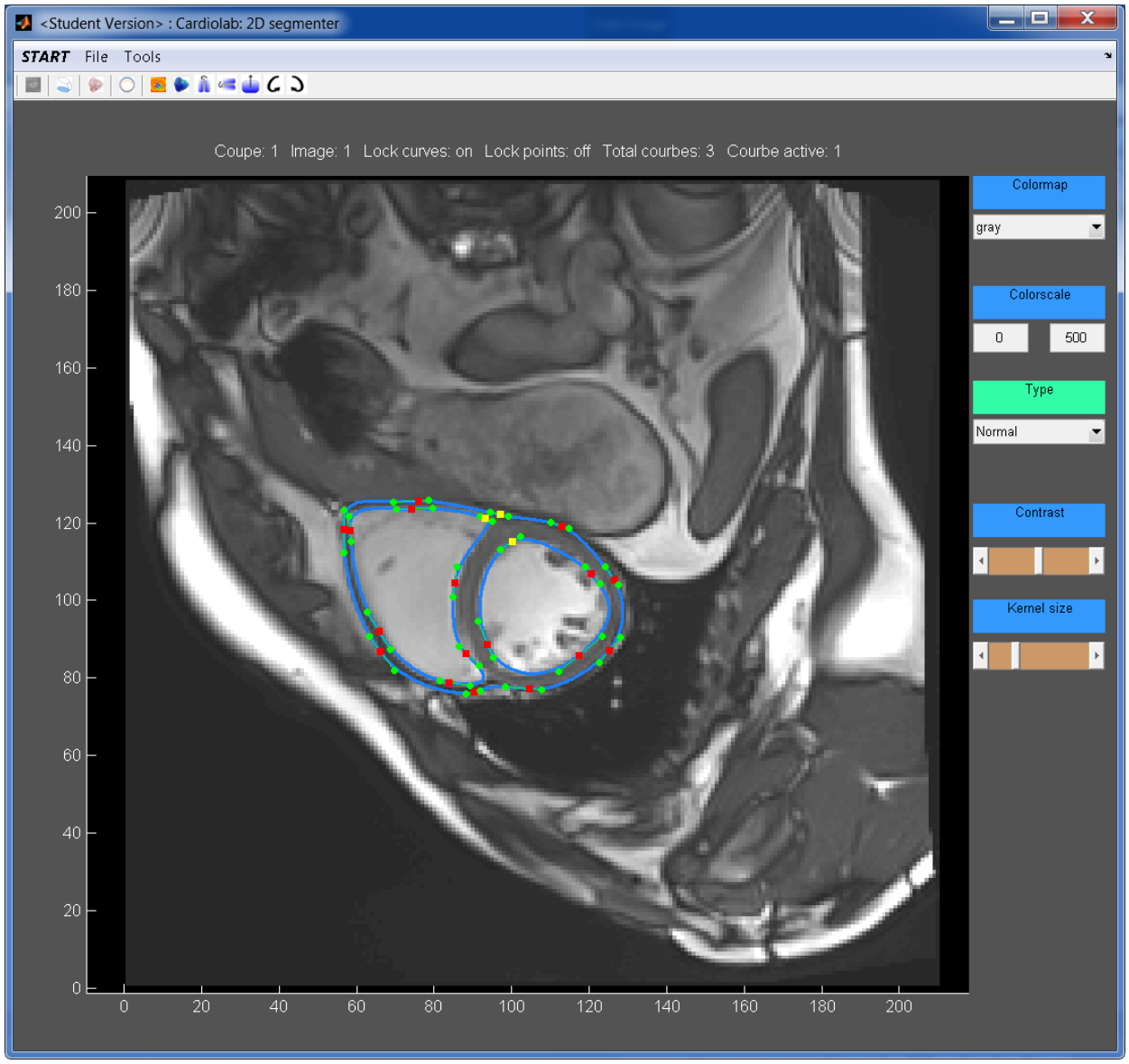

Figure H.1: The main segmentation software which uses template based on Bezier curves.